Title

Optical Breakdown in gases induced by high-power IR CO_2 laser pulses

Authors

J. J. Camacho[1], L. Díaz[2], M. Santos[2], L. J. Juan[1] and J. M. L. Poyato[1]

[1]Departamento de Química-Física Aplicada. Facultad de Ciencias. Universidad Autónoma de Madrid. Cantoblanco. 28049-Madrid. Spain

[2]Instituto de Estructura de la Materia, CFMAC, CSIC, Serrano 121. 28006-Madrid, Spain

E-mails: j.j.camacho@uam.es; luisol@cfmac.csic.es; magna@iem.cfmac.csic.es; jml.poyato@uam.es;

Abstract

This chapter reviews some fundamentals of laser-induced breakdown spectroscopy (LIBS) and describes some experimental studies developed in our laboratory on gases such as nitrogen, oxygen and air. LIBS of these gases at different pressures, in the spectral range ultraviolet-visible-near infrared (UV-Vis-NIR), was excited by using a high-power transverse excitation atmospheric (TEA) CO_2 laser (λ=9.621 and 10.591 μm; τ_{FWHM}=64 ns; and different laser power densities). The spectra of the generated plasmas are dominated by emission of strong atomic, ionic species and molecular bands. Excitation temperatures were estimated by means of atomic and ionic lines. Electron number densities were deduced from the Stark broadening of several ionic lines. The characteristics of the spectral emission intensities from different species have been investigated as functions of the gas pressure and laser irradiance. Optical breakdown threshold intensities in different gases have been measured experimentally. The physical processes leading to laser-induced breakdown of the gases have been analyzed. Plasma characteristics in LIBS of air were examined in detail on the emission lines of N^+, O^+ and C by means of time-resolved optical-emission spectroscopy (OES) technique. The results show a faster decay of continuum and ionic spectral species than of neutral atomic and molecular ones. The velocity and kinetic energy distributions for different species were obtained from time-of-flight (TOF) OES measurements. Excitation temperature and electron density in the laser-induced plasma were estimated from the analysis of spectral data at various times from the laser pulse incidence. Temporal evolution of electron density has been used for the estimation of the three-body recombination rate constant.

Table of contents

1. Introduction

A remarkable demonstration of the interaction of radiation with matter is the plasma production which occurs when a powerful laser is focused in a gas. Strong pulses of infrared (IR) laser light can cause breakdown and plasma formation in gases which are usually transparent at these wavelengths. By this means gases are transformed into opaque, highly conducting plasmas in times of the order of nanoseconds. If the radiant energy in the focus exceeds the threshold value for breakdown, as happens with high-power lasers (ruby, Nd:YAG, CO_2, excimer, etc), the gas becomes highly ionized and the plasma thus produced will practically absorb the beam. In atmospheric air, for example, laser-beam-induced breakdown is characterized by a brilliant flash of bluish-white light at the lens focus accompanied by a distinctive cracking noise. This transformation from neutral gas into hot plasma takes place in three quite distinct stages: initiation, formative growth, and plasma development accompanied by shock wave generation and propagation in the surrounding gas. A fourth and final stage, extinction, follows.

The formation of laser-induced breakdown (LIB) plasma in a gas has been investigated since its discovery by Maker *et al* [1] resulting in several studies that have been summarized by different authors [2-16]. Several hundred papers describing various aspects of the phenomenon have been published, and a healthy controversy appears to be in existence concerning the mechanisms by which gases can become almost perfect conductors under the influence of short-duration pulses of long-wavelength light alone. The LIB plasma develops a shock wave into the ambient medium and the gas is heated to high temperatures [17]. It is evident that after breakdown, the plasma becomes very opaque and an abrupt shutoff of the laser transmitted light occurs. Due to the many experimental parameters involved in the LIB, an exhaustive investigation of the plasma would involve the processing of an impressive number of records. To investigate LIB of gases several diagnostic techniques have been employed in the last years. Optical emission spectroscopy (OES) is a powerful tool to get information on the LIB species. Because of the transient features of the plume created by LIB, OES technique with time and space resolution is

especially appropriate to obtain information about the behaviour of the created species in space and time as well as the dynamics of the plasma evolution. Although OES gives only partial information about the plasma particles, this diagnostic technique helped us to draw a picture of the plasma in terms of the emitting chemical species, to evaluate their possible mechanisms of excitation and formation and to study the role of gas-phase reactions in the plasma expansion process.

The objectives of this work are: (i) to show some fundamentals of laser-induced breakdown spectroscopy (LIBS) and, (ii) to review of our recent results on LIBS analysis of chemical species in gases plasmas induced by high-power IR CO_2 laser, adding some new results. This chapter describes the experimental results obtained from UV-Visible-near IR spectra of LIB plasmas generated by carbon dioxide laser pulses in gases such as N_2, O_2 and air. The major parts of this work are already published by us in different journals [18-21]. We consider here only research on the plasma induced when a high-intensity laser radiation is focused in a gas. The emission observed in the laser-induced plasma region is due to electronic relaxation of excited atoms, ions and molecular bands of different diatomic molecules. Excitation temperatures and electron number densities were calculated by means of different atomic and ionic lines. Estimates of vibrational and rotational temperatures of some molecules electronically excited species are also reported. The characteristics of the spectral emission intensities from different species have been investigated as functions of the gas pressure and laser irradiance. Optical breakdown threshold intensities in the different studied gases have been determined.

For air we discuss the dynamics of the plume expansion and formation of different atomic, ionic and molecular species for different delay times with respect to the beginning of the laser pulse. The velocity and kinetic distributions for the different species were obtained from the time-of-flight (TOF) measurements using time-resolved OES. Possible mechanisms for the production of these distributions are discussed. Line intensities from different atomic and ionic species were used for determining electron temperature and Stark-broadened profiles of some lines were

employed to calculate electron density. The temporal behavior of electron number density has been employed for the estimation of three-body recombination rate constant and recombination time. The present paper is aimed at discussing thermo-chemical processes produced by a high-power IR CO_2 pulsed laser on several gases and at evaluating LIB changes which are of fundamental importance in establishing the mechanisms responsible for the plasma emission.

1.1 Laser-Induced Breakdown Spectroscopy (LIBS)

Excellent textbooks and reviews about the fundamentals of laser-induced breakdown spectroscopy (LIBS) and examples of various processes are readily available today [13-16]. LIBS, also sometimes called laser-induced plasma spectroscopy, is a technique of atomic-molecular emission spectroscopy which utilizes a highly-power laser pulse as the excitation source. LIBS can analyze any matter regardless of its physical state, being it solid, liquid or gas. Because all elements emit light when excited to sufficiently high energy, LIBS can detect different species (atomic, ionic and molecular) and limited only by the power of the laser as well as the sensitivity and wavelength range of the spectrograph/detector. Basically LIBS makes use of OES and is to this extent very similar to arc/spark emission spectroscopy. LIBS operates by focusing the laser onto a small volume of the sample; when the laser is triggered it breaks a very small amount of gas which instantaneously generates a plasma plume with temperatures of about 10000–30000 K. At these temperatures, the gas dissociates (breakdown) into excited ionic and atomic species. At the early time, the plasma emits a continuum of radiation which does not contain any known information about the species present in the plume and within a very small timeframe the plasma expands at supersonic velocities and cools. At this point the characteristic atomic/ionic and molecular emission lines of the species can be observed. The delay between the emission of the continuum and characteristic radiation is of the order of 1 μs, this is one of the reasons for temporally gating the detector. LIBS is technically similar and complementary to a number of other laser-based techniques (Raman spectroscopy, laser-induced fluorescence etc). In fact devices

are now being manufactured which combine these techniques in a single instrument, allowing the atomic, molecular and structural characterization of a sample as well as giving a deeper insight into physical properties. A typical LIBS system consists of a pulsed laser and a spectrometer with a wide spectral range and a high sensitivity, fast response rate and time gated detector. The principal advantages of LIBS over the conventional analytical spectroscopic techniques are its simplicity and the sampling speed.

1.2 Laser parameters

The variables that can influence the LIBS measurements are mainly the laser properties i.e. wavelength, energy, pulse duration, focusing spot size, shot-to-shot energy fluctuations, ambient conditions, physical properties of the sample and the detection window (delay time and gate width). How these parameters affect the precision and accuracy of LIBS are addressed below. In LIBS a high-power laser is used to breakdown a gaseous sample in the form of plasma. The primary energy related parameters influencing the laser-gas interaction are the laser peak power P_W (or radiant pulse energy per time, in W) and the laser peak intensity I_W (power density or irradiance; energy per unit area and time, W cm^{-2}) given by

$$P_W = E_W / \tau_{FWHM}^{Las}, \quad (1.1)$$

$$I_W = P_W / \pi r^2, \quad (1.2)$$

where E_W (in J) is the pulse energy, τ_{FWHM}^{Las} (in s) is the laser pulse duration of the full width at half maximum (FWHM) and πr^2 is the focal spot area (cm^2). The fluence Φ_W (in J cm^{-2}) on the focused spot area, the photon flux density F_{ph} (photon cm^{-2} s^{-1}), electric field F_E (V cm^{-1}) and pressure radiation p_R (in Pa) are given by

$$\Phi_W = E_W / \pi r^2, \quad (1.3)$$

$$F_{ph} = I_W \lambda / hc, \quad (1.4)$$

$$F_{\mathrm{E}} = \sqrt{I_{\mathrm{W}} / c\varepsilon_0}\ , \tag{1.5}$$

$$p_{\mathrm{R}} = 2I_{\mathrm{W}} / c\ , \tag{1.6}$$

where λ is the laser wavelength, h is the Planck constant, c is the speed of light, and ε_0 is the electric constant. In Eq. (1.6) we suppose that the laser radiation is totally reflected and therefore the pressure radiation can be doubled. The laser peak intensity I_{W}, fluence, photon flux, electric field and pressure radiation are inversely proportional to the focused spot area. For LIBS, the peak intensity I_{W} (and the other properties Φ_{W}, F_{ph}, F_{E} and p_{R}) that can be delivered to the sample is more important than the absolute value of the laser power. For the formation of plasma, the laser irradiance needs to exceed the threshold value, typically of the order of several GW×cm^{-2} for a nanosecond laser pulse. If the laser energy is very close to the breakdown threshold, the pulse-to-pulse fluctuations can cause the plasma condition to be irreproducible, which results in poor measurement precision. The intensities of the emission lines are proportional to the laser energy while the laser plasma is in the optical thin region. When the laser energy increases further, it produces very dense and hot plasma that can absorb laser energy. This will lead to an increase in the continuum emission and a decrease in the signal intensity. Besides, the laser pulse duration and the shot-to-shot fluctuations can also affect the signal reproducibility and hence LIBS precision.

1.3 Focal properties

The laser power density at the focal volume is inversely proportional to the focused spot size. For a laser beam with a Gaussian profile, the focused bean waist w_0 is given by

$$w_0 = \frac{\lambda\ f}{\pi\ w_{\mathrm{s}}}, \tag{1.7}$$

where f is the focal length of the lens and w_{s} is the radius of the unfocused beam. The higher laser power density at the focal point can be achieved by reducing the focused beam waist using a

shorter focal length lens. On the other hand, the angular spread in laser light generated by the diffraction of plane waves passing through a circular aperture consists of a central, bright circular spot (the Airy disk) surrounded by a series of bright rings. The beam divergence angle θ, measured to edges of Airy disk, is given by $\theta=2.44\times\lambda/d$, where λ is the laser wavelength and d is the diameter of the circular aperture. It can be shown that a laser beam, with beam divergence θ_i, incident on a lens of focal length f, whose diameter is several times larger than the width of the incident beam, is focused to a diffraction-limited spot of diameter approximately equal to $f\times\theta_i$. If the focal region of the laser beam is assumed to be cylindrical is shape, the spot size in terms of length l, can be approximated as

$$l = (\sqrt{2}-1)\theta_i f^2 / d \ . \qquad (1.8)$$

2. Optical breakdown in gases

Optical breakdown in gases leads to the generation of free electrons and ions, electrons in gases are either bound to a particular molecule or are quasifree when they have sufficient kinetic energy to move without being captured by local molecular energy potentials. Thus, transitions bound and quasi-free states are the equivalent of ionization of molecules in gases. The optical breakdown process describes in greater detail by Raizer [2-3, 23], starts when a laser beam with sufficient power density is focused down, and a sufficient radiation flux density is achieved, leading to a discharge/spark. This discharge is somewhat similar to the discharge induced by a sufficient electric field between the electrodes of a spark plug in an internal combustion engine. The temperature and pressure of the gas in the region of this discharge will be increased significantly as the energy of the laser is absorbed to cause this so called laser induced optical breakdown. The energy deposition into a gas by a focused laser beam can be described by four progressive steps: (i) initial release of electrons by multi-photon effect; (ii) ionization of the gas in the focal region by the cascade release of electrons; (iii) absorption and reflection of laser energy by the gaseous plasma, rapid expansion of the plasma and detonation wave formation; and (iv) the

propagation of the detonation wave into the surrounding gas and relaxation of the focal plasma region.

2.1 LIB plasma

Plasma is a local assembly of atoms, molecules, ions and free electrons, overall electrically neutral, in which the charged species often act collectively. The LIB plasma is initiated by a single laser pulse. If we consider the temporal evolution of LIB plasma, at early times the ionization grade is high. As electron-ion recombination proceeds, neutral atoms and molecules form. A recombination occurs when a free electron is captured into an ionic or atomic energy level and gives up its excess kinetic energy in the form of a photon. LIB plasmas are characterized by a variety of parameters, the most basic being the degree of ionization. A weakly ionized plasma is one in which the ratio of electrons to other species is less than 10%. At the other extreme, high ionized plasmas may have atoms stripped of many of their electrons, resulting in very high electron to atom/ion ratios. LIB plasmas typically, for low power laser intensities, fall in the category of weak ionized plasmas. At high laser power densities, LIB plasmas correspond to strong ionized plasmas.

2.2. Initiation mechanism: Multiphoton ionization (MPI) and electron impact ionization (EII)

Plasma is initiated by electron generation and electron density growth. The conventional LIB plasma can be initiated in two methods: **multiphoton ionization** (MPI) and **electron impact ionization** (EII) both followed by electron cascade. EII is sometimes denominated as cascade ionization process or avalanche ionization due to **inverse bremsstrahlung** (IB) heating of electrons. MPI involves the simultaneous absorption of a number of photons n, required to equal the ionization potential $I_P(A)$ of an atom or molecule A

$$nh\nu + A \rightarrow A^+ + e + I_P(A);\ nh\nu \geq I_P(A), \qquad (2.1)$$

where n is the number of photons needed to strip off an electron, which corresponds to the integer part of the quantity:

$$n = \frac{I_{\mathrm{P}} + \varepsilon_{\mathrm{osc}}}{h\nu} + 1. \qquad (2.2)$$

Here $\varepsilon_{\mathrm{osc}}$ is the oscillation energy of a free electron in the alternating electric field. Within the classical microwave breakdown theory [22], a free electron oscillates in the alternating electric field E of the laser electromagnetic wave with frequency ω and wavelength λ (μm), and its oscillation energy,

$$\varepsilon_{\mathrm{osc}}[eV] = \frac{e^2E^2}{4m\omega^2} = \frac{e^2}{4m\pi c^3} I_{\mathrm{W}}\lambda^2 = 4.67\times10^{-14} I_{\mathrm{W}}\lambda^2, \qquad (2.3)$$

remains constant. In Eq. (2.3) e is the electron charge and I_{w} is the laser intensity [irradiance, power density or flux density in W×cm^{-2}; Eq. 1.2]. The probability of MPI W_{MPI}, by absorbing simultaneously n laser photons to strip off an electron, is expressed by the classical formula [23]

$$W_{\mathrm{MPI}}[\mathrm{s}^{-1}] \cong \omega\, n^{3/2} \left(1.36\frac{\varepsilon_{\mathrm{osc}}}{I_{\mathrm{P}}}\right)^n = 1.88\times10^{15}\lambda^{2n-1} n^{3/2} \left\{\frac{6.35\times10^{-14} I_{\mathrm{W}}}{I_{\mathrm{P}}}\right\}^n, \qquad (2.4)$$

where I_{P} is in eV. Besides, the probability of simultaneous absorption of photons decreases with the number of photons n necessary to cause ionization. Therefore, the MPI rate is proportional to $I_{\mathrm{W}}^{\mathrm{n}}$ and inversely proportional to $I_{\mathrm{P}}^{\mathrm{n}}$.

EII process consists on the absorption of light photon by free or quasifree electrons, producing electrons with enough kinetic energy e^* to ionize one atom or molecule

$$e + n\mathrm{h}\nu + A \rightarrow e^* + A \rightarrow 2e + A^+. \qquad (2.5)$$

Two conditions must co-exist for EII to initiate: (i) an initial electron must reside in the focal volume; and (ii) the initial electron must acquire energy which exceeds the ionization energy of the material in the focus. These free or quasifree electrons can be produced by the effect of cosmic ray ionization (natural ionization), by means of MPI, or by a breakdown induced in some impurity. The equilibrium number of free electrons and ions per cm^3 in the atmosphere at the earth's surface is about 500 [24]. The electron cascade ionization process requires the presence of

either free electrons or excited atoms or molecules in the focal region for their initiation, but the possibility of a free electron or an excited atom produced by natural causes being present there during the laser flash can be discounted, as Tozer pointed out [25]. They occur naturally in the earth's atmosphere, produced at a rate of about 10 $cm^{-3}\times s^{-1}$ at the earth's surface by the presence of local radioactivity and the passage of ultraviolet radiation and cosmic rays. Most electrons become rapidly attached to electronegative atoms and molecules to form negative ions. The mean lifetime of a free electron in the atmosphere is about 10^{-7} s, so that the aggregate life of free electrons is about 10^{-6} s when liberated at the rate of $\approx$ 10 $cm^{-3}\times s^{-1}$. The probability of finding a free electron in the focal region $\approx 10^{-4}$ cm^3 during a laser flash $\approx 10^{-8}$ s is thus entirely negligible, as is the chance for finding an excited atom. One concludes that the laser light itself produces the initiatory electrons. These electrons in the focal volume gain sufficient energy, from the laser field through IB collision with neutrals, to ionize atoms, molecules or ions by inelastic electron-particle collision resulting in two electrons of lower energy being available to start the process again

$$e^*[\epsilon \geq I_P(A)] + A \rightarrow A^+ + 2e;\ e^*[\epsilon \geq I_P(A^+)] + A^+ \rightarrow A^{2+} + 2e. \qquad (2.6)$$

Thus a third species (atom-molecule/ion) is necessary for conserving momentum and energy during optical absorption. The recurring sequences of IB absorption events and subsequent EII lead to a rapid growth in the number of free electrons, if the laser intensity is sufficient to overcome the losses of free electrons through diffusion out of the focal volume and through recombination. The MPI mechanism dominates electron generation only for low exciting wavelengths. Therefore initial EII becomes a problem at a higher wavelength because neither cascade nor MPI can furnish sufficient number of electrons. At higher laser intensities, electric field of the laser is able to pull an outer shell electron out of its orbit. After the initial electron ejection the LIB plasma is commonly maintained by the absorption of optical energy and the EII. Electrons in the laser field will gain energy through electron-neutral IB collisions and will lose energy by elastic and inelastic collisions with the neutral species through excitation of rotational and vibrational degree of freedom of molecules and excitation of electronic states. While some

electrons will be lost by attachment, new electrons will be produced by ionizing collisions. At high laser intensity, few electrons will be generated with energy larger than the ionization energy. The wavelength-resolved emission spectra from the laser plasma are not expected to vary due to the plasma origin. However plasma origin may be relevant, if the enhancement is observed between UV, visible and IR excitation wavelengths.

Once that LIB plasma is formed, its growth is governed by the continuity rate equation for the electron density [26] due to the combined effect of EII and MPI

$$\frac{dn_e}{dt} = \nu_i n_e + W_n I_W^n N - \nu_a n_e - \nu_R n_e^2 + D_e \nabla^2 n_e , \qquad (2.7)$$

where ν_i is the impact ionization rate, W_n is the multiphoton ionization rate coefficient, I_w is the intensity of the laser beam, n is the number of photons required for MPI, N is the number of atoms/molecules per unit volume, ν_a is the attachment rate, ν_R is the recombination rate and D_e is the electron diffusion coefficient. The term dn_e/dt is the net rate of change in electron concentration at a point in the focal volume at a time t after the release of initiatory electrons. On the right side of the equation (2.7), the first term is the electron generation due to impact ionization. The second term on the right is MPI rate. The third, fourth and fifth terms are sink terms which represent electron attachment, recombination and diffusion, respectively. Impact ionization is defined by multiplying the number of electrons per unit volume to the impact ionization rate ν_i. The impact ionization rate refers to the rate at which electrons are generated as a result of ionizing collisions. At high laser intensity, a few new electrons can be generated and gain energy larger than their ionization energy which leads to the generation of new electrons by impact ionization, thereby leading to the cascade growth. Recombination losses are usually not important in the breakdown forming stage.

2.3. Electron attachment, recombination and diffusion

Electron attachment is the rate of electron attachment ν_a multiplied by the number of electrons per unit volume. The LIB plasma typically loose electrons to the neutral species via the

attachment mechanism in the form of three-body attachment or two-body dissociative attachment. Three-body attachment is: $e + AB + X \rightarrow AB^- + X$, where X appears to be a facilitator that allows the electrons to be gained by AB even through X remains unchanged throughout the process. Two-body dissociative attachment is: $e + AB \rightarrow A^- + B$. In this mechanism the electrons must exhibit a threshold electron energy that is equal to the difference between the dissociative energy of AB and the attachment energy of A, which results in the separation of A and B.

Electron recombination is the rate of electron recombination ν_R multiplied to the number of electrons per unit volume. When the electron density is high, such as during the last stage of cascade breakdown, the LIB plasma can lose electrons to ions through electron-ion recombination. Similar to the electron attachment, three-body recombination and two-body recombination occurs as: $e + AB^+ + X \rightarrow AB + X$, $e + AB^+ \rightarrow A + B$. The electron-ion recombination rate has been studied theoretically for a three-body recombination by Gurevich and Pitaevskii [27]

$$\nu_R = 8.8 \times 10^{-27} \frac{n_e^2}{T_e^{3.5}} \ [s^{-1}], \tag{2.8}$$

where n_e is the electron density in cm^{-3} and T_e is the electron temperature in eV. The electron diffusion term is expressed as $D_e \nabla^2 n_e$ [Eq. (2.7)]. This loss mechanism, more important for a small diameter laser beam, is the diffusion of electrons out of the focal volume. Morgan [6] referred to the combined effect of diffusion and cascade ionization as the responsible for top-hat intensity profile. By imposing an electron skin at the edge of the intensity profile, they found that the electron density grows exponentially as

$$\langle \nu_e \rangle = \frac{2.408 D_e}{r^2} \ , \tag{2.9}$$

where $\langle \nu_e \rangle$ is the average electron velocity, D_e is electron diffusion coefficient and r is the radius of the beam. The equation (2.9) is intended to be an upper boundary for diffusion losses only because laser beams typically have a radial distribution closer to the Gaussian rather than top-hat distribution.

In LIB plasmas, the decrease of electron density n_e is mainly due to recombination between electrons and ions in the plasma. These processes correspond to the so-called radiative recombination and three-body recombination processes in which a third body may be either a heavy particle or an electron. The electron number density n_e (cm^{-3}) in the laser induced plasma is governed by the kinetic balance equation [28, 29]

$$\frac{dn_e}{dt} = k_{ion} n_e N_i - k_{rec} n_e^3, \tag{2.10}$$

where N_i indicates the concentration of heavy particles (neutrals and ions) and k_{ion} ($cm^3\ s^{-1}$) and k_{rec} ($cm^6\ s^{-1}$) denote the rate constants of ionization ($e + A \rightarrow A^+ + 2e$) and tree-body electron-ion recombination ($2e + A^+ \rightarrow A^* + e$), respectively. The excess of energy in three-body electron-ion recombination is deposited as kinetic energy to a free electron, which participates in the recombination process as a third body partner. The three-body electron-ion recombination energy can be converted into radiation in the process of radiative electron-ion recombination ($e + A^+ \rightarrow A^* \rightarrow A + h\nu$). The cross section of this process is relatively low and it can be competitive with three-body electron-ion recombination only when the plasma density is low. If $dn_e/dt=0$ an equilibrium condition can be established; if $dn_e/dt\neq0$, then the ionization ($dn_e/dt>0$) or the three-body recombination ($dn_e/dt<0$) prevails and departure from equilibrium occurs [28]. The second derivative of $Y=dn_e/dt$ with respect to the electron number density is given by

$$\frac{d^2Y}{dn_e^2} = -6k_{rec} n_e . \tag{2.11}$$

The recombination time can be determined by the value of the rate constant of the recombination process as $t_{rec}=1/(n_e^2.k_{rec})$ [29].

In summary, the process of plasma initiation essentially consists of the formation of free or quasi-free electrons by interplay of MPI and EII. Therefore, two mechanisms MPI and EII can initiate a conventional LIB plasma formation. After the LIB plasma formation the temporal growth is governed by the equation (2.7). The recombination of these two source terms (MPI and EII) and three sink terms (electron attachment, electron recombination and electron diffusion)

controls the development of the conventional LIB plasma. The decrease of n_e is mainly due to the so-called radiative recombination and three-body recombination processes in which a third body may be either a heavy particle or an electron. These mechanisms that directly affect the temporal development of the LIB plasma, determine the necessary spectroscopic techniques required to spectrally resolve elemental species inside the LIB plasma.

2.4. Optical breakdown threshold intensities

The minimum power density required to form a plasma is called the breakdown threshold; different types of laser, sample, and environmental conditions will have different breakdown thresholds. Breakdown thresholds of solids and liquids are usually much lower than those for gases. The principal method of investigation has been to measure the beam intensity required for electron liberation and the minimum intensity needed to produce breakdown as a function of the radiation wavelength and pressure of a variety of gases. Precise measurements of the intensities of laser radiation required to release initiatory electrons or to lead to breakdown are made only with the greatest difficulty. The difficulties arise on account of the imprecise definition of the extent of the focal region and inaccurate knowledge of the spatial-temporal characteristics of the beam intensity within the focal region, which, in turn, lead to uncertainties in the absolute value of the instantaneous radiation intensity. The parameters which characterize a focused laser beam are its polarization, wavelength, line width, duration, divergence and the temporal and spatial distribution of intensity. For a given pulse these are functions of the laser and focusing system governed by the mode structure within the laser cavity, by the aberration functions of the lens or focusing mirror, and by the beam diameter at the lens or mirror. In specifying the electron liberation or breakdown threshold intensities all these factors should ideally be specified, but, regrettably, in the literature there is often inadequate detail and essential features of experimental procedures are frequently omitted. In consequence many published data are of little value, serving merely to indicate orders of magnitude and broad trends only rather than absolute values in well-defined conditions. For

these reasons data published by various workers are often contradictory, and reliable interpretation is sometimes difficult to make.

For gases to breakdown, a certain concentration of electrons has to be reached before the end of the laser pulse. Laser-induced breakdown is frequently defined [5, 30] as an electron density multiplication during the laser pulse by a factor of 10^{13} corresponding to 43 electron generations. In fact, multiplying the natural electron density by 10^{13} leads to $n_e \approx 10^{16}\,\mathrm{cm}^{-3}$ which is the electron density of plasmas at atmospheric pressure for which electron-ion IB dominates electron-neutral IB. With respect to electron-neutral IB, the electron-ion IB has a much higher efficiency as a result of the long range Coulomb interaction, and a plasma with an electron density $n_e = 10^{16}\ \mathrm{cm}^{-3}$ is quasi instantaneously completely ionized.

The condition for optical breakdown is taken to occur when the number density of the induced electrons equals the critical density for the laser wavelength. The critical plasma density $n_e^{\mathrm{crit}}\left[\mathrm{cm}^{-3}\right] = m\ \omega^2 / 4\pi e^2 \cong 1.1\times 10^{21} / \lambda^2[\mu\mathrm{m}]$ ($n_e^{\mathrm{crit}} \cong 10^{19}\ cm^{-3}$ for CO_2 laser) is the density where the electron plasma frequency equals to the laser frequency. When the electron density exceeds the critical density the sample is not transparent any more. Energetic electrons produce excited species through impact excitation, dissociation and ionization of gas molecules. According to the microwave theory [22], electrons gain energy from the laser radiation field by elastic collisions with neutral atoms at the rate: $(\mathrm{d}\varepsilon/\mathrm{d}t)_{\mathrm{gain}} = (e^2 F_E^2 / m)\cdot[\nu_c^2/(\omega^2+\nu_c^2)]$, where F_E and ω are the root-mean-square electric field and angular frequency of the radiation and ν_c is the electron-neutral collision frequency.

Several models have been developed to describe the optical breakdown and to compute the breakdown threshold. Chan *et al.* [30] proposed a model based on the energy balance of electrons neglecting their energy distribution. According to this work, breakdown occurred if the laser heating of electrons by IB induces a gain of electron energy that overcomes the energy losses. Thus, one requires a laser power density (power threshold density)

$$I_{las} \geq \frac{m\ c\ I_P}{4\pi e^2 \ln 2} \frac{\omega^2 + \nu_c^2}{\nu_c} \left[\frac{43}{\tau_{las}} \ln 2 + \frac{D_e}{\Lambda^2} + \frac{2m\ \langle \varepsilon \rangle\ \ln 2\ \nu_c}{M\ I_P} + (\alpha + \frac{\beta}{\Lambda^2})\nu_c \right], \quad (2.12)$$

where m and e are the mass and charge of electrons, c is the light velocity, and I_P and M are the ionization potential and the atomic mass of the gas. The terms ω, ν_c, τ_{las}, D_e, Λ and $<\epsilon>$ are the laser frequency, effective electron-neutral collision frequency, laser pulse duration, diffusion coefficient, diffusion length and average electron energy, respectively. The terms α (dimensionless) and β (length^2) are two parameters which depend on the atomic structure of the gas. The terms inside the brackets represent various loss terms. The first term in the brackets stands for the generation of 43 electrons necessary for breakdown. The second, third, and fourth terms take into account the electron energy loss due to diffusion out of the focal volume, elastic and inelastic collisions, respectively. The loss due to electron attachment is very low and therefore not considered in Eq. (2.12). The losses due to elastic and inelastic collisions are proportional to ν_c that increases linearly with the gas pressure p. At low pressure, collisional loss can be neglected and electron heating by IB varies linearly with p according to $\nu_c^2 << \omega$. Thus, the threshold decreases with p in the low-pressure range. When increasing p to sufficiently high values, the collisional losses overcome the terms of electron generation and diffusion loss. If $\nu_c^2 << \omega$ still holds, both gain and loss terms are proportional to p and the threshold is pressure independent. In the high pressure range ($\nu_c^2 >> \omega$) the gain by IB diminishes as p^{-1} and the threshold increases. Thus, it exists an optimum pressure for which the optical breakdown threshold is minimum. According to Eq. (2.12), the breakdown power threshold density in general is directly proportional to the ionization potential of the gas. Moreover, the breakdown threshold passes through a minimum at the pressure when laser angular frequency ω is equal to the effective electron-neutral collision frequency ν_c as indicated by the term outside the brackets. Depending on their relative magnitudes, breakdown may be termed to be limited, diffusion limited or attachment limited [30].

Time-limited breakdown occurs if the first term in the brackets dominates, that is when the laser pulse duration τ_{las} is so short that the growth rate of electron density required to induce a visible

breakdown exceeds any losses. Thus, the threshold power density varies inversely with pulse duration and the breakdown is determined by the product of the intensity times the pulse duration. Diffusion-limited processes occur when the second term in the brackets dominates, that is for gas breakdown to take place in a small focal volume at low gas pressure. The breakdown power density threshold in this case decreases as Λ^{-2} with the focal size and it also decreases as p^{-2} with the gas pressure in the range of pressure so that $\omega >> \nu_c$. The third and fourth terms are the attachment and elastic collision loses. They are relatively unimportant and are dependent on the type and masses of the gas. For inert gases, the attachment loss can be completely neglected. The last term is the energy loss due to inelastic collision and it should be important for molecular gases because the large number of excited states they possess. Because the attachment rate and collision frequency are assumed to be proportional to the gas pressure *p*, these three terms are independent of the gas pressure.

At low pressure and in particular for small waist, the electron diffusion out of the focal volume is the dominating loss term. The electron diffusion length Λ can be estimated assuming a focal volume of cylindrical shape with radius

$$r = \frac{f\Theta}{2}, \tag{2.13}$$

and length $l = \left(\sqrt{2}-1\right)\frac{f^2\Theta}{d}$ (Eq. 1.8), where *f* is the focal length of the focussing lens, Θ the angle of laser beam divergence, and *d* the laser beam diameter incident on the lens. For a Gaussian laser beam, one has

$$\frac{1}{\Lambda^2} = \left(\frac{2.405}{r}\right)^2 + \left(\frac{\pi}{l}\right)^2, \tag{2.14}$$

For a large numerical opening ($\geq f/5$), Eq. (2.14) is simplified to $\Lambda = r/2.405$. Using this expression with *r* from Eq. (2.13) and computing the electron diffusion coefficient as

$$D_e = \frac{2\langle\varepsilon\rangle}{3m\nu_{eff}}, \tag{2.15}$$

the energy loss due to electron diffusion is evaluated. With respect to the loss due to elastic collisions, the energy loss by diffusion can be neglected if

$$\nu_{\text{eff}} >> \frac{4.81\sqrt{I_P M}}{\sqrt{3} m f \Theta}. \qquad (2.16)$$

A large dispersion of breakdown threshold values exists in literature. It is attributed to the large number of parameters on which the optical breakdown depends. Several mechanisms have been found to reduce the threshold of optical breakdown. Smith and Haught [31] observed threshold lowering by Penning effect during ruby laser breakdown in a high-pressure Ar atmosphere when adding 1% Ne. The phenomenon was due to Ar ionization by collisions with excited Ne atoms which were produced by a resonant excitation process. However, the threshold lowering was at maximum of about 50% [31]. For CO_2 laser radiation, a resonant excitation process can be excluded because of the small photon energy and the Penning effect does not contribute to optical breakdown threshold lowering in the far IR spectral range. For laser radiation of sufficiently high photon energy, the presence of impurities with low ionization energy led to the threshold lowering [32] that was attributed to multiphoton ionization. However, this effect was not observed for CO_2 laser radiation. Gas impurities with the lowest ionization potential like hydrocarbon radicals require at least the simultaneous absorption of more than 50 photons that is a process of vanishing probability. Contrarily, molecular species such as hydrocarbon or other radicals brake the ionization avalanche. They have many vibrational and rotational excitation levels which cause electron energy loss by inelastic collisions [see Eq. (2.12)].

Several authors [33, 34] reported threshold lowering when initiating the breakdown by ablation of a solid target. A threshold reduction by a factor of 10^2 was observed for CO_2 laser radiation [33]. The threshold lowering was explained by shock wave generation as an effect of strong material ablation. The shock wave heats up the surrounding gas which is instantaneously transformed in a strongly ionized plasma. The optical breakdown from solid material ablation has been shown to be a multistage plasma initiation process that is characterized by three thresholds

[34]: (i) the material ablation threshold I_{vap}; (ii) the breakdown threshold of the evaporated material I_{vap}^{*}; and (iii) the breakdown threshold of the surrounding gas I_{gas}^{*}. It is noted that I_{vap}* and I_{gas}^{*} are the thresholds of preionized vapour and the gas, respectively. For the case of CO_2 laser ablation, the initial ionization stage of the ablated material vapour is $n_e/n_{vap}<10^{-5}$-10^{-4}[34], n_{vap} being the ablated material vapor density. As a consequence of preionization, the number of electrons generations necessary for complete ionization is strongly reduced (<<43). Thus, the electron generation term can be neglected in Eq. (2.12). The diffusion loss can be also neglected according to the relative large volume preionized by the shock wave. In the case of rare gases, the loss by inelastic collisions is much smaller than that due to elastic collisions and the avalanche ionization is determined by the balance between IB heating of electrons and losses by elastic collisions. The breakdown threshold (in W×cm^{-2}) given by Eq. (2.12) is simplified to [34]

$$I_{las} \geq I_{EC}^{*} = 1.8 \times 10^{7} \frac{I_P}{M}, \qquad (2.17)$$

where the ionization potential is in eV and the atomic mass of the gas is in atomic mass units. The index *EC* stands for elastic collisions to recall that only this loss term has been taken into account. Barchukov *et al.* [33] proposed a threshold criterion similar to Eq. (2.17) with a three times larger numerical constant. The difference is due to the average electron energy which was supposed to be equal to the ionization potential by Barchukov *et al.* [33] while $<\epsilon>=(1/3)I_P$ was taken for Eq. (2.17).

2.5. Laser-plasma interaction

The interaction between the laser radiation and free electrons of the plasma is described by the Drude model considering the electron motion in the laser field as a harmonic oscillator. For collision frequencies $\omega_P^2>>\nu_c^2$, where ω_P is the plasma frequency. The dielectric constant is given by $\epsilon\approx1 - \omega_P^2/\omega^2$, where ω is the laser frequency. Optical breakdown in gases at atmospheric pressure leads to an electron density equal to the critical density (for CO_2 laser radiation $n_e^{crit} \cong 10^{19}$ cm^{-3}). In the region where the critical density is reached, the plasma frequency is

equal to the laser frequency and $n = \sqrt{\varepsilon} = 0$. The plasma is thus completely reflecting in the corresponding zone. Only a few authors have investigated the laser beam reflection by the plasma. In fact, the studies show that breakdown plasmas reaching the critical density absorb most of the incident laser energy [35-37]. The fraction of reflected radiation is small because of strong absorption in the zone adjacent to the plasma sheet of critical density. Donaldson *et al.* [36] showed that 80% of incident laser energy was absorbed in a zone of weak thickness where the electronic density varied from $0.83n_e^{crit}$ to n_e^{crit} when generating breakdown with a (Nd:YAG) laser of τ_{las}=35 ps and $I_W=10^{14}$ Wcm^{-2}. Offenberger and Burnett [35] measured the reflected and transmitted power of TEA-CO_2 laser pulses during breakdown in hydrogen. The reflected power was always below 2% of the incident laser power. The major absorption mechanism of CO_2 laser radiation during breakdown ignition is electron-neutral IB. Once strongly ionized plasma is formed, the electron impact ionization or electron-ion IB dominates as a result of the long range Coulomb interaction between charged particles.

Several experimental and theoretical studies have been performed to investigate the IB effect. Among numerous expressions for the determination of the IB absorption coefficient [2, 5, 36] the formula

$$\alpha_{IB} = 3.69\times10^{8}\,\frac{n_e^2\sum_i f_i Z_i^2}{\sqrt{T_e}\,\nu^3}\left(1-e^{-h\omega/2\pi k_B T}\right)\ [\mathrm{cm}^{-1}], \qquad (2.18)$$

proposed by Spitzer [38] was used by many authors to estimate the laser energy absorption by the plasma. Here, T_e and n_e are in K and cm^{-3}, respectively. The factors f_i are the fractional abundances of ions, Z_i the corresponding ion charge. In the case of CO_2 laser radiation, one has $\left(1-e^{-h\omega/2\pi k_B T}\right)\approx h\omega/2\pi k_B T$ and Eq. (2.18) simplifies for a singly ionized plasma to

$$\alpha_{IB} = 1.8\times10^{-35}\,\frac{n_e^2}{T_e^{3/2}}\ [\mathrm{cm}^{-1}], \qquad (2.19)$$

where T_e is in eV. Equation (2.19) shows that the efficiency of IB absorption decreases with increasing electron temperature. At high plasma temperatures, other absorption mechanisms

dominate. They have been made in evidence during studies of laser-plasma interaction related to thermonuclear fusion using power densities several orders of magnitude higher than breakdown thresholds.

2.6. Absorption wave propagation

After breakdown ignition, the strongly absorbing plasma will propagate in the direction opposite to the laser beam. The absorption wave formation has been observed in many experiments using CO_2 laser sources [33, 35, 39]. The theoretical analyses of optical breakdown and absorption wave propagation performed by Raizer [2] using a hydrodynamic model have been widely accepted and became a standard theory in the field. According to this model, the laser-induced absorption waves propagate by the following stepwise mechanisms: (i) A small plasma zone is heated up by the laser beam. It reaches the critical density and strongly absorbs the laser radiation. (ii) The electron density in the adjacent zones increases. (iii) The adjacent preionized zone that is irradiated by the laser beam is heated up and becomes absorbent. Thus, the strongly absorbing plasma zone propagates in the direction opposite to the laser beam.

Three different propagation modes are distinguished. The breakdown wave is characterized by the following propagation mechanism: (i) breakdown occurs initially in the region of the highest laser power density and later in the zones of lower power density. The expansion of high pressure plasma compresses the surrounding gas and drives a shock wave. Thus, the breakdown propagates in the direction opposite to the laser beam. The plasma also tends to expand back along the beam path toward the laser, a phenomenon known as moving breakdown. The velocity of the breakdown wave is given by

$$v_{bw} = \frac{w_0}{t_b \, \mathrm{tg}\varphi} \,, \tag{2.20}$$

where w_0 and φ are the minimum radius and opening angle of the focused laser beam, respectively. For example, for our typical experimental conditions with the CO_2 laser, taking w_0=0.05 cm, t_b=100 ns and tgφ=0.2, the breakdown wave propagates with $v_{bw}=2.5\times10^6$ cm/s;

(ii) Propagation through the detonation wave mechanisms occurs when rapid heating of the gas in the region of strong absorption induces a spherical shock wave. The latter propagates into the surrounding gas that is heated and preionized. The part of the preionized gas that is further illuminated by the laser beam absorbs the laser radiation and becomes opaque. Thus, the absorption zone follows the shock wave. The propagation velocity of the detonation wave is given by

$$\mathrm{v}_{\mathrm{bw}} = \left[2\left(\gamma^2 - 1\right)\frac{I_{\mathrm{W}}}{\rho_0} \right]^{1/3} , \tag{2.21}$$

where γ and ρ_0 are the adiabatic constant of the gas and the specific mass, respectively. The specific energy that is injected into the gas is

$$\varepsilon_{\mathrm{bw}} = \frac{\gamma}{\left(\gamma^2 - 1\right)\left(\gamma + 1\right)} \mathrm{v}_{\mathrm{bw}}^2 . \tag{2.22}$$

It is noted that detonation wave propagation velocity and injected specific energy are independent of the atomic structure of the gas. The gas influences the detonation wave propagation only through its specific mass and adiabatic constant. Thus, a change of gas nature is equivalent to a pressure variation if γ is unchanged. Consequently, the detonation wave propagation velocity in Ar is equal to that in Xe at three times lower pressure. For Xe at atmospheric pressure and $I_{\mathrm{W}}=10^8$ W cm^{-2}, the detonation wave propagates with a velocity of 6×10^5 cm s^{-1} and heats up the gas to a temperature of 28 eV. The temperature is obtained by assuming an ideal gas, for which the specific energy is related to the temperature by $\epsilon_{\mathrm{bw}}=(3/2)\ k_{\mathrm{B}}\ T\ N_{\mathrm{A}}/M$. Here, k_{B}, T, N_{A} and M are Boltzmann's constant, plasma temperature, Avogadro's constant and mass, respectively.

(iii) For $I_{\mathrm{W}}>10^{10}$ Wcm^{-2}, the plasma is heated up to $T<10^2$ eV. According to the high temperature, the plasma strongly radiates in the UV and soft X-ray spectral range ionizing thus the surrounding gas. Once preionized, the gas in the zone illuminated by the laser beam absorbs the laser radiation and a laser sustained radiation wave propagates in the direction opposite to the laser beam. The dominating propagation mechanism of the absorption wave depends on the

experimental conditions. Breakdown waves are formed in the case of very small opening angle of the focused laser beam whereas radiation waves occur at very high laser power density. For moderate power density and sufficiently wide opening angle, the optical breakdown propagates as a detonation wave.

A portion of the laser pulse energy is absorbed by the expanding plasma generating three different types of waves: (i) laser-supported combustion (LSC) waves; (ii) laser-supported detonation (LSD) waves; and (iii) laser-supported radiation (LSR) waves [40]. They differ in their predictions of the opacity and energy transfer properties of the plasma to the surrounding gas. At low-power laser regime (I_W<1 MW/cm^2), LSC waves are produced, which comprise of a precursor shock, that is separated from the absorption zone and the plasma. The shock wave results in an increase in the ambient gas density, temperature and pressure, whereas the shock edges remain transparent to the laser light. At medium-power laser regime (1 MW/cm^2<I_W<4 GW/cm^2), the precursor shock is sufficiently strong and the shocked gas is hot enough to begin absorbing the laser radiation without requiring additional heating by energy from the plasma. The laser absorption zone follows directly behind the shock wave and moves at the same velocity. In this case a LSD wave is produced and has been modelled by several Raizer [2-3, 23]. The propagation of the LSD wave is controlled by the absorption of the laser energy. At high-power laser regime (I_W >4 GW/cm^2), the plasma is so hot that, prior to the arrival of the shock wave, the gas it heated to temperatures at which laser absorption begins. Laser radiation is initiated without any density change and the pressure profile results mainly from the strong local heating of the gas rather than a propagating shock wave. The LSR wave velocity increases much more rapidly with irradiance than those of the LSC and LSD waves.

3. LIB plasma analysis

In contrast to conventional spectroscopy, where one is mainly concerned with the structure of an isolated atom and molecule, the radiation from the plasma also depends on the properties of the

plasma in the intermediate environment of the atomic or molecular radiator. This dependence is a consequence of the long-range Coulomb potential effects which dominate the interactions of ions and electrons with each other and with existing neutral particles. These interactions are reflected in the characteristic radiations in several ways. They can control population densities of the discrete atomic states, spectral shift and broadening by Stark effect, decrease of ionization potentials of the atomic species, cause continuum radiation emissions and emission of normally forbidden lines. Generally, the radiation emitted from self-luminous plasma can be divided into bound-bound (b-b), bound-free (b-f), and free-free (f-f) transitions.

3.1 Local Thermodynamic Equilibrium (LTE).

Plasma description starts by trying to characterize properties of the assembly of atoms, molecules, ions and electrons rather than individual species. If thermodynamic equilibrium exits, then plasma properties can be described through the concept of temperature. Thermodynamic equilibrium is rarely complete, so physicists have settled for a useful approximation, local thermodynamic equilibrium (LTE). In LTE model it is assumed that the distribution of population densities of the electrons is determined exclusively through collisional processes and that they have sufficient rate constants so that the distribution responds instantaneously to any change in the plasma conditions. In such circumstances each process is accompanied by its inverse and these pairs of processes occur at equal rates by the principle of detailed balance. Thus, the distribution of population densities of the electrons energy levels is the same as it would be in a system in complete thermodynamic equilibrium. The population distribution is determined by the statistical mechanical law of equipartition among energy levels and does not require knowledge of atomic cross sections for its calculation. Thus, although the plasma density and temperature may vary in space and time, the distribution of population densities at any instant and point in space depends entirely on local values of density, temperature, and chemical composition of plasma. If the free electrons are distributed among the energy levels available for them, their velocities have a Maxwellian distribution

$$dn_{\mathrm{v}} = n_e 4\pi \left(\frac{m}{2\pi k_B T_e} \right)^{3/2} \exp\left(-\frac{m\ \mathrm{v}^2}{2k_B T_e} \right) \mathrm{v}^2 d\mathrm{v}\,, \tag{3.1}$$

where n_e is the electron density, m is the electron mass, k_B is the Boltzmann constant, T_e is the electron temperature and v is the electron velocity. For the bound levels the distributions of population densities of neutrals and ions are given by the Boltzmann (3.2) and Saha (3.3) equations

$$\frac{N_j}{N_i} = \frac{g_j}{g_i} \exp\left(-\frac{(E_j - E_i)}{k_B T_e} \right) \quad , \tag{3.2}$$

$$\frac{N_{z+1,k} n_e}{N_{z,k}} = \frac{g_{z+1,k}}{g_{z,k}} 2 \left(\frac{2\pi\ m\ k_B\ T_e}{h^2} \right)^{3/2} \exp\left(-\frac{I\mathrm{p}_{z,k}}{k_B T_e} \right), \tag{3.3}$$

where N_i, N_j, $N_{z+1,k}$ and $N_{z,k}$ are the population densities of various levels designated by their quantum numbers j (upper), i (lower) and k (the last for the ground level) and ionic charge z and z+1. The term $g_{z,i}$ is the statistical weight of the designated level, E_j and E_i are the energy of the levels j and i and $Ip_{z,k}$ is the ionization potential of the ion of charge z in its ground level k. Equations (3.1)-(3.3) describe the state of the electrons in an LTE plasma. For complete LTE of the populations of all levels, including the ground state, a necessary condition is that electron collisional rates for a given transition exceed the corresponding radiative rates by about an order of magnitude [41]. This condition gives a criterion [42] for the critical electron density of the level with energy $\Delta E = E_j - E_i$

$$n_e^{\mathrm{crit}} \geq \frac{5}{8\sqrt{\pi}} \left(\frac{\alpha}{a_0} \right)^3 z^7 \left(\frac{\Delta E}{z^2 E_{\mathrm{H}}} \right)^3 \sqrt{\left(\frac{k_{\mathrm{B}} T_{\mathrm{e}}}{z^2 E_{\mathrm{H}}} \right)} \cong 1.6 \times 10^{12} T_{\mathrm{e}}^{1/2} (\Delta E)^3, \tag{3.4}$$

where α is fine-structure parameter, a_0 is Bohr radius, and E_{H} is the hydrogen ionization potential. In the numerical relationship of Eq. (3.4), n_e^{crit} is given in cm^{-3}, T_e in K and ΔE (energy difference between the two neighboring states) in eV. Many plasmas of particular interest do not come close

to complete LTE, but can be considered to be only in partial thermodynamic equilibrium in the sense that the population of sufficiently highly excited levels are related to the next ion's ground state population by Saha-Boltzmann relations, respective to the total population in all fine-structure levels of the ground state configuration [41]. For any atom or ion with simple Rydberg level structure, various criteria were advanced for the minimum principal quantum number n_{crit} for the lowest level, often called thermal or collision limit, for which partial thermodynamic equilibrium remains valid to within 10%. One criterion with quite general validity is given by Griem [42]:

$$n_{crit} \approx \left[\frac{10 z^7}{2\sqrt{\pi} n_e} \left(\frac{\alpha}{a_0} \right)^3 \right]^{2/17} \left(\frac{k_B T_e}{z^2 E_H} \right)^{1/17} . \tag{3.5}$$

3.2 Line Radiation

Line radiation from plasma occurs for electron transitions between the discrete or bound energy levels in atoms, molecules or ions. In an optically thin plasma of length l along the line of sight [43], the integrated emission intensity I_{ji} of a spectral line arising from a transition between bound levels j and i is given by

$$I_{ji} = \frac{A_{ji} h \nu_{ji}}{4\pi} \int N_j ds = h \nu_{ji} A_{ji} N_j l , \tag{3.6}$$

where N_{j} is the population density of the upper level j, $h\nu_{\mathrm{ji}}$ is the photon energy (energy difference between levels j and i), and A_{ji} is the spontaneous transition probability or Einstein A coefficient. The integration is taken over a depth of plasma viewed by the detector, and the intensity of radiation is measured in units of power per unit area per unit solid angle. Transition probabilities can be sometimes expressed via the oscillator strength f_{ji}. This is defined as the ratio of the number of classical oscillators to the number of lower state atoms required to give the same line-integrated absorption [44]. Its relationship to the Einstein coefficient is

$$f_{ji} = \frac{4\pi\varepsilon_0}{e^2}\frac{mc^3}{8\pi^2\nu_{ji}}\frac{g_j}{g_i}A_{ji}. \qquad (3.7)$$

The usefulness of f_{ji} is that it is dimensionless, describing just the relative strength of the transition. The detailed values of A_{ji} , g_i, and g_j can be obtained from reference compilations or from electronic databases, i.e by NIST [45].

3.3 Continuum Radiation

The origins of continuum radiation are both bound-free and free-free transitions. Free-free emission or IB radiation is due to the interaction of free electrons with positively charged ions. In free-bound emission (recombination radiation), a free electron is captured by an ion in a bound level. The energy of the photon given off is the difference between original energy of the electron and its new energy in whatever level of whatever atom it ends up in. Since this difference can have any value, the result of many free-bound transitions is a continuous spectrum. Transitions between two free energy levels can occur in plasmas increasing the energy exchanges of charged particles. Classically, this takes place because a moving charge radiates when it is accelerated or retarded. For most cases of practical importance, these free-free transitions are classified as bremsstrahlung or cyclotron spectra. In bremsstrahlung, the acceleration of charged particle takes place via the Coulomb field of charged particles. In cyclotron radiation, the acceleration is due to the gyration of charged particles in a magnetic field. The total continuum radiation at any particular frequency $I(\nu)$ is the sum of the contributions from all such processes having components at the specified frequency. Thus

$$I(\nu)d\nu = \frac{1}{4\pi}\int n_e \sum_i N_i \left[\gamma(i, T_e, \nu) + \sum_p \alpha(i, j, T_e, \nu)\right] h\nu \; ds \; d\nu , \qquad (3.8)$$

where $\gamma(i, T_e, \nu)$ is the atomic probability of a photon of frequency ν being produced in the field of an atom or ion (specified by i) by an electron of mean kinetic temperature T_e making free-free

transition; $\alpha(i, j, T_e, \nu)$ is the corresponding probability where the electron makes a free-bound transition into a level *j*. As before, the integration is taken over the plasma depth *s*.

3.4 Line Broadening; Determination of electron number density from Stark broadening of spectral lines

The shape of the spectral lines in the LIB has been studied since the first observation of the laser-induced breakdown in early 1960s. It plays an important role for the spectrochemical analysis and quantification of the plasma parameters. The observed spectral lines are always broadened, partly due to the finite resolution of the spectrometers and partly to intrinsic physical causes. In addition, the center of the spectral lines may be shifted from its nominal central wavelength. The principal physical causes of spectral line broadening are the Doppler, resonance pressure, and Stark broadening. There are several reasons for this broadening and shift. These reasons may be divided into two broad categories: broadening due to local conditions and broadening due to extended conditions. Broadening due to local conditions is due to effects which hold in a small region around the emitting element, usually small enough to assure LTE. Broadening due to extended conditions may result from changes to the spectral distribution of the radiation as it traverses its path to the observer. It also may result from the combining of radiation from a number of regions which are far from each other.

3.4.1 Natural broadening

The uncertainty principle relates the lifetime of an excited state (due to the spontaneous radiative decay) with the uncertainty of its energy. This broadening effect results in an unshifted Lorentzian profile. The FWHM of natural broadening for a transition with a natural lifetime of τ_{ji} is: $\Delta\lambda^{N}_{FWHM}=\lambda^2/\pi c\tau_{ji}$. The natural lifetime τ_{ji} is dependent on the probability of spontaneous decay: $\tau_{ji}=1/A_{ji}$. Natural broadening is usually very small compared with other causes of broadening.

3.4.2 Doppler broadening

The Doppler broadening is due to the thermal motion of the emitting atoms, molecules or ions. The atoms in a gas which are emitting radiation will have a distribution of velocities. Each photon emitted will be "red" or "blue" shifted by the Doppler effect depending on the velocity of the atom relative to the observer. The higher the temperature of the gas, the wider the distribution of velocities in the gas. Since the spectral line is a combination of all of the emitted radiation, the higher the temperature of the gas, the broader will be the spectral line emitted from that gas. This broadening effect is described by a Gaussian profile and there is no associated shift. For a Maxwellian velocity distribution the line shape is Gaussian, and the FWHM may be estimated as (in Å):

$$\Delta\lambda_{\mathrm{FWHM}}^{\mathrm{D}} = 7.16\times10^{-7}\cdot\lambda\cdot\sqrt{T/M}\ , \qquad (3.9)$$

being λ the wavelength in Å, T the temperature of the emitters in K, and M the atomic mass in amu.

3.4.3 Pressure broadening

The presence of nearby particles will affect the radiation emitted by an individual particle. There are two limiting cases by which this occurs: (i) Impact pressure broadening: The collision of other particles with the emitting particle interrupts the emission process. The duration of the collision is much shorter than the lifetime of the emission process. This effect depends on both the density and the temperature of the gas. The broadening effect is described by a Lorentzian profile and there may be an associated shift. (ii) Quasistatic pressure broadening: The presence of other particles shifts the energy levels in the emitting particle, thereby altering the frequency of the emitted radiation. The duration of the influence is much longer than the lifetime of the emission process. This effect depends on the density of the gas, but is rather insensitive to temperature. The form of the line profile is determined by the functional form of the perturbing force with respect to distance from the perturbing particle. There may also be a shift in the line center. Pressure

broadening may also be classified by the nature of the perturbing force as follows: (i) *Linear Stark broadening* occurs via the linear Stark effect which results from the interaction of an emitter with an electric field, which causes a shift in energy which is linear in the field strength ($\sim E$ and $\sim 1/r^2$); (ii) *Resonance broadening* occurs when the perturbing particle is of the same type as the emitting particle, which introduces the possibility of an energy exchange process ($\sim E$ and $\sim 1/r^3$); (iii) *Quadratic Stark broadening* occurs via the quadratic Stark effect which results from the interaction of an emitter with an electric field, which causes a shift in energy which is quadratic in the field strength ($\sim E$ and $\sim 1/r^4$); (iv) *Van der Waals broadening* occurs when the emitting particle is being perturbed by Van der Waals forces. For the quasistatic case, a Van der Waals profile is often useful in describing the profile. The energy shift as a function of distance is given in the wings by e.g. the Lennard-Jones potential ($\sim$E and $\sim 1/r^6$).

3.4.4 Stark broadening

Stark broadening of spectral lines in the plasma occurs when an emitting species at a distance r from an ion or electron is perturbed by the electric field. This interaction is described by the Stark effect. The linear Stark effect exists for hydrogen and for all other atoms. Stark broadening from collisions of charged species is the primary mechanism influencing the emission spectra in LIBS. Stark broadening of well-isolated lines in the plasma can be used to determine the electron number density $n_e(\mathrm{cm}^{-3})$. In the case of a non-H-like line, an estimation of the Stark width (FWHM) and line shift of the Stark broadened lines is given as [41-44]:

$$\Delta\lambda_{\mathrm{FWHM}}^{\mathrm{Stark}} = 2W\left(\frac{n_e}{10^{16}}\right) + 3.5A\left(\frac{n_e}{10^{16}}\right)^{1/4}\left(1 - BN_D^{-1/3}\right) W\left(\frac{n_e}{10^{16}}\right), \tag{3.10}$$

$$\Delta\lambda^{\mathrm{Shift}} = D\left(\frac{n_e}{10^{16}}\right) \pm 2A\left(\frac{n_e}{10^{16}}\right)^{1/4}\left(1 - BN_D^{-1/3}\right) W\left(\frac{n_e}{10^{16}}\right), \tag{3.11}$$

where W is the electron impact parameter or half-width, A is the ion impact parameter both in Å, B is a coefficient equal to 1.2 or 0.75 for ionic or neutral lines, respectively, D (in Å) is the electron

shift parameter and N_D is the number of particles in the Debye sphere $N_D=1.72\times10^9 T^{3/2} n_e^{-1/2}$. The electron and the ion impact parameters are functions of temperature. The first term on the right side of Eq. (3.10) refers to the broadening due to the electron contribution, whereas the second one is the ion broadening. The minus sign in Eq. (3.11) applies to the high-temperature range of those few lines that have a negative value of D/W at low temperatures. Since for LIB conditions Stark broadening is predominantly by electron impact, the ion correction factor can safely be neglected, and Eq. (3.10) becomes

$$\Delta\lambda_{\mathrm{FWHM}}^{\mathrm{Stark}} \approx 2W\left(\frac{n_e}{10^{16}}\right). \qquad (3.12)$$

The coefficients W are independent of n_e and slowly varying functions of electron temperature. A comprehensive list of width and shift parameters W, A and D is given by Griem [42].

In the quasi-static approximation, the interaction between slowly moving ions and radiating species can be approximated by a perturbation which remains nearly constant over the whole time that the species is radiating. Hydrogen and hydrogen-like ions exhibits linear Stark effect. The FWHM (in Å) of a hydrogen or H-like ion spectral line, in the quasi-static approximation, is given by [41, 42]

$$\Delta\lambda_{\mathrm{FWHM}}^{\mathrm{Stark}} = 8.16\times10^{-19}\left(1-0.7N_D^{-1/3}\right)\lambda_0^2(n_2^2-n_1^2)(Z_p^{1/3}-Z_e)n_e^{2/3}, \qquad (3.13)$$

where λ_0 is the wavelength line centre, n_2 and n_1 are the principal quantum numbers of the upper and lower states, respectively, Z_p and Z_e are the nuclear charge on the perturbing ion and the emitting species (atom or ion) and n_e is the electron number density in cm^{-3}. Although the line shapes do depend on the electron contribution, the FWHM are generally insensitive. Eq. (3.13) represents a very good estimate of the Stark broadening in those hydrogenic lines that do not have a strong undisplaced Stark component as for example L_β, L_δ, H_β (Balmer) and H_δ transitions. On

the other hand, the FWHM of hydrogenic lines with strong central Stark components are dominated by interaction of the electrons with the emitting hydrogenic species such as L_α and H_α transitions. Such lines have a Lorentzian line shape and FWHM for L_α transition in the impact approximation is given by

$$\Delta\lambda_{\mathrm{FWHM}}^{\mathrm{Stark}} \approx 1.62\times10^{-17}\,\frac{n_{\mathrm{e}}}{\sqrt{T}}\left(13.76-\log\frac{n_e^{1/2}}{T}\right), \tag{3.14}$$

where $\Delta\lambda_{\mathrm{FWHM}}^{\mathrm{Stark}}$ is in Å, T is in K and n_{e} is in cm^{-3}. It is seen from Eqs. (3.13) and (3.14) that the ion broadening, in the quasi-static approximation, varies as $n_{\mathrm{e}}^{2/3}$ and is independent of the temperature whereas the collisional broadening varies approximately as n_{e} and it is very much temperature dependent. It is to be noted the electron densities determined from Eqs. (3.13) and (3.14) are only crude estimations and one must compute the entire line profile to extract the total line width for an accurate estimation of n_{e}.

3.5 Determination of excitation, vibrational and rotational temperatures

The excitation temperature T_{exc} can be calculated according to the Boltzmann equation under the assumption of LTE (Section 3.1). The significance of this temperature depends on the degree of equilibrium within the plasma. For plasma in LTE, any point can be described by its local values of temperature, density, and chemical composition. By considering two lines λ_{ji} and λ_{nm} of the same species, characterized by different values of the upper energy level ($E_{\mathrm{j}}\neq E_{\mathrm{n}}$), the relative intensity ratio can be used to calculate the plasma excitation temperature

$$T_{\mathrm{exc}} = \frac{E_j - E_n}{k_{\mathrm{B}}\ln\left[\dfrac{I_{nm}\cdot\lambda_{nm}\cdot g_j\cdot A_{ji}}{I_{ji}\cdot\lambda_{ji}\cdot g_n\cdot A_{nm}}\right]}. \tag{3.15}$$

When selecting a line pair, it is advisable to choose two lines as close as possible in wavelength and as far apart as possible in excitation energy. This is to limit the effect of varying the spectral response of the detection system. The use of several lines instead of just one pair leads to greater

precision of the plasma excitation temperature estimation. In fact, though the precision of the intensity values can be improved by increasing the signal intensity, the transition probabilities A_{ji} reported in the literature exhibit significance degree of uncertainty (5-50%). The excitation temperature can be calculated from the relative intensities of a series of lines from different excitation states of the same atomic or ionic species from the slope of the Bolztmann plot $\ln[I_{ji}\cdot\lambda_{ji}/g_j\cdot A_{ji}]$ versus E_j/k_B

$$\ln\left[\frac{I_{ji}\cdot\lambda_{ji}}{g_j\cdot A_{ji}}\right]=C-\frac{E_j}{k_B\cdot T_{exc}}\ , \tag{3.16}$$

where I_{ji} is the emissivity (W m^{-3} sr^{-1}) of the emitted $j\rightarrow i$ spectral line, λ_{ji} is the wavelength, $g_j=2J_j+1$ is the statistical weight, A_{ji} is the Einstein transition probability of spontaneous emission, E_j/k_B is the normalized energy of the upper electronic level and $C=\ln(hcN_j/4\pi Q(T))$ ($Q(T)$ is the partition function). The values of the λ_{ji}, g_j, A_{ji} and E_i for selected atomic or ionic lines can be obtained from the NIST Atomic Spectral Database [45]. A set of selected spectral lines can be chosen based on their relative strengths, accuracies and transition probabilities.

The emission spectra of the diatomic species reveal a relatively complex structure which is due to the combination of the electronic transitions from the different rotational and vibrational states [46-48]. The emission intensities of the molecular bands can be analyzed in order to calculate the molecular vibrational temperature T_{vib}. For a plasma in LTE, the intensity of an individual vibrational v'-v" band $I_{v'-v"}$ is given by

$$\ln\left(\frac{I_{v'-v"}\cdot\lambda_{v'-v"}^4}{q_{v'-v"}}\right)=A-\frac{G(v')h\ c}{k_B\cdot T_{vib}}\ , \tag{3.17}$$

where A is a constant, $\lambda_{v'-v"}$ is the wavelength corresponding to the band head, $q_{v'-v"}=\left|\int_0^\infty \Psi_{v'}(R)\Psi_{v"}(R)dR\right|^2$ is the Franck-Condon factor and $G(v')h\ c/k_B$ is the normalized

energy of the upper vibrational level. A line fit to $\ln\left(I_{v'-v''}\cdot\lambda^4_{v'-v''}/q_{v'-v''}\right)$ as a function of the upper normalized electronic-vibrational energies has a slope equal to -1/T_{vib}.

On the other hand, the emission intensities of the rotational lines of a vibrational band can be analyzed in order to estimate the effective rotational temperature T_{rot}. In this case it is necessary to consider the Hund´s coupling case for the both electronic states implied in the transition. From the assignment of the rotational spectrum it is possible to estimate the effective rotational temperature by considering the J value for the maximum of the band $T_{rot}=(2\,B_v\,h\,c/k_B)(J_{max}+1/2)^2$, being B_v the rotational constant for v' vibrational level and J_{max} the total angular momentum at the maximum.

Another method for estimating the vibrational and rotational temperatures is based on a simulation program of the spectra. Software developed in our laboratory [49] calculated the spectra of a diatomic molecule by summing the intensity of all rovibrational levels and convoluting the results with the instrumental line shape of the optical system. The emission intensity $I_{v',J'-v'',J''}$ of a molecular line can be approximated by

$$I_{v',J'-v'',J''}\approx\frac{64\pi^4\tilde{\nu}^4_{v',J'-v'',J''}}{3(2J'+1)}N_{v',J'}\overline{R}_e^{\,2}q_{v',v''}S_{J',J''}\quad , \tag{3.18}$$

where $\tilde{\nu}_{v',J'-v'',J''}$ is the wavenumber of the transition, 2J'+1 is the rotational degeneracy of the upper state, $N_{v',J'}$ is the population in the initial (upper) state, $\overline{R}_e$ is the average electronic transition moment, $q_{v',v''}$ is the Franck-Condon factor and $S_{J',J''}$ is the Hönl-London factor [50]. Spectrum simulations are based on comparison of experimental and calculated spectra for different rotational and vibrational population distributions which depend on temperature.

3.6 Ionization degree of the plasmas: Saha equation

In plasma there is a continuous transition from gases with neutral atoms to a state with ionized atoms, which is determined by an ionization equation. The transition between gas and

plasma is essentially a chemical equilibrium, which shifts from the gas to the plasma side with increasing temperature. Let us consider the first three different ionization equilibria of an atom *A*:

$A \leftrightarrow A^{+}+e+IP(A\text{-}I)$,

$A^{+} \leftrightarrow A^{2+} + e + IP(A\text{-}II)$,

$A^{2+} \leftrightarrow A^{3+} + e + IP(A\text{-}III)$.

For each ionization equilibrium, considering the atoms and ions in their ground electronic state, the LTE between ionization and recombination reactions at temperature *T* is described by the Saha equation (see Eq. 3.3)

$$\frac{n_e \cdot N_i}{N_0} = \frac{g_e \cdot g_i}{g_0} \frac{\left(2\pi\ m\ k_B T\right)^{3/2}}{h^3} e^{-I_P/k_B T}, \qquad (3.19)$$

where $n_e = N_i$ are the electron and ion densities in the different ionization equilibria in the second member of ionization equilibria. From this equation, ionization degree $n_e \cdot N_i / N_0$ can be estimated.

4. Experimental details

LIBS is a plasma based method that uses instrumentation similar to that used by other spectroscopic methods (atomic emission spectroscopy, laser-induced fluorescence etc). A typical LIBS apparatus utilizes a pulsed laser that generates the powerful optical pulses used to form the plasma. Principles of laser operation in general and the operation of specific lasers are described in detail in numerous books. The discussion here will be limited to the fundamentals of the operation of the transversely excited atmospheric (TEA) carbon dioxide laser used in this work. The CO_2 laser is a near-infrared gas laser capable of very high power and with the highest efficiency of all gas lasers (≈10-20%) and for cw operation the highest output power. Although CO_2 lasers have found many applications including surgical procedure, their popular image is as powerful devices for cutting, drilling, welding or as weapons for military applications. The linear CO_2 molecule has three normal modes of vibration, labelled v_1 (symmetry stretch), v_2 (bending vibration) and v_3

(asymmetric stretch). The fundamental vibration wavenumbers are 1354, 673 and 2396 cm^{-1}, respectively. The vibrational state of the molecule is described by the number of vibrational quanta in these modes. The bending vibrational mode is twofold degenerate and can have a vibrational angular momentum along the CO_2 axis. The number of quanta of this vibrational angular momentum is stated as an upper index to the vibrational v_2 quanta. The upper laser level (00^01) denotes the ground vibrational state for the mode v_1, the ground vibrational state for the mode v_2 which is doubly degenerate, and the first excited vibrational state for the mode v_3. The active medium is a gas discharge in a mixture of He, N_2 and CO_2. By electron impact in the discharge excited vibrational levels in the electronic ground states of N_2 and CO_2 are populated. The vibrational levels v = 1 in the N_2 molecule and (ν_1, ν_2, ν_3) = (00^01) in the CO_2 molecule are near-resonant and energy transfer from the N_2 molecule to the CO_2 molecule becomes very efficient. This populates the (00^01) level in CO_2 preferentially, creates inversion between the (00^01) and the (02^00) levels, and allows laser oscillations on many rotational transitions between these two vibrational states in the wavelength range 9.6-10.6 μm. The main laser transitions in CO_2 occur between the excited states of the mode $\nu_3(00^01)$ and the symmetric stretching mode $\nu_1(10^00)$ (10.6 μm) or the bending mode $\nu_2(01^10)$ (9.6 μm). A single line can be selected by a Littrow-grating, forming one of the resonator end mirrors. Helium atoms do not take part directly in the excitation of CO_2 molecules but do play an important role in heat-transfer from the gas mixture to the tube walls, as well as facilitating the depopulation of the lower vibrational levels in CO_2, contributing in this way to the maintenance of the population inversion. The power of CO_2 lasers depends on their configuration. The laser used in these experiments was a transversely excited atmospheric (TEA) CO_2 laser in which the gas-flow is transverse to the laser cavity's axis. The pressure in the tube is close to atmospheric pressure. The CO_2:N_2:He mixture is exchange in a continuous way, enhancing the output power of the laser. The laser can achieve a power of 50 MW. The optical materials used in lasers emitting radiation in the infrared range are obviously different than those used in the visible range. For example, materials such as germanium (Ge) or

gallium arsenide (GaAs) are completely opaque in the visible range, while being transparent in the infrared range. Some materials, such as zinc selenide (ZnSe), are transparent in both spectral ranges. Typical materials transparent in the IR range are: NaCl or CsI. Metal mirrors (copper, molybdenum) are used in the IR range, owing to their small absorption (and large reflectivity) as well as their large heat capacity which enables removal of heat from the active medium.

A schematic diagram of the experimental configuration used for time-resolved TEA-CO_2 pulsed laser gas breakdown diagnostics is shown in Fig. 1. The experiments were carried out with a transverse excitation atmospheric (TEA) CO_2 laser (Lumonics model K-103) operating on an 8:8:84 mixture of CO_2:N_2:He, respectively. The laser is equipped with frontal Ge multimode optics (35 % reflectivity) and a rear diffraction grating with 135 lines mm^{-1} blazed at 10.6 μm. The laser pulse repetition rate was usually 1 Hz. The divergence of the emitted laser beam is 3 mrad. The laser delivered up to 3.16 J at a wavelength of 10.591 μm, leading to an estimated power of 49.5 MW (Eq. 1.1), intensity (power density or irradiance) of 6.31 GW cm^{-2} (Eq. 1.2), fluence of 403 J×cm^{-2} (Eq. 1.3), photon flux of 3.1×10^{29} photon×cm^{-2}×s^{-1} (Eq. 1.4), electric field of 1.54 MV×cm^{-1} (Eq. 1.5) and radiation pressure of 421 kPa (Eq. 1.6) on the focal position. The focused-spot area (7.85×10^{-3} cm^2) of the laser beam was measured with a pyroelectric array detector (Delta Development Mark IV). The temporal shape of the TEA-CO_2 laser pulse, monitored with a photon drag detector (Rofin Sinar 7415), consisted in a prominent spike of a FWHM of around 64 ns carrying ~90% of the laser energy, followed by a long lasting tail of lower energy and about 3 μs duration. The primary laser beam was angularly defined and attenuated by a diaphragm of 17.5 mm diameter before entering to the gas cell. A beam splitter was used to redirect 10% of the laser pulse energy on a pyroelectric detector (Lumonics 20D) or on a photon-drag detector (Rofin Sinar 7415) for energy and temporal shape monitoring and triggering, respectively, through a digital oscilloscope (Tektronix TDS 540). The laser-pulse energy was varied with the aid of several calibrated CaF_2 attenuating plates. The shot-to-shot fluctuation of the laser energy was approximately 5%. In time-resolved gas breakdown, the pulsed laser light was focused by a NaCl

lens of 24 cm focal lens onto the surface of a 0.7 mm×0.7 mm stainless steel mesh in gas at atmospheric pressure. This allows us to fix the focal position for LIB at any fluence inducing strong gas breakdown plasma. No lines from metals were found in the spectra, meaning that the metal mesh was practically never ablated. The high purity gases (~99.99 %) were placed in a medium-vacuum cell equipped with a NaCl window for the laser beam and two quartz windows for optical access. The gas is initially at ambient temperature (298 K). The cell was evacuated with the aid of a rotary pump, to a base pressure of 4 Pa that was measured by a mechanical gauge. Optical emission from the plume was imaged by a collecting optical system onto the entrance slit of different spectrometers. The light emitted from the laser-induced plasma was optically imaged 1:1, at right angles to the normal to the focal volume, by a quartz lens (focal length 4 cm, *f*-number = *f*/2.3) onto the entrance slit of the spectrometer. The distance between gas plasma axis and entrance slit was typically *y*=16 cm. Optical emission accompanying the laser-induced gas plasma was viewed in a *XZ* parallel plane to the front face of the metal mesh for different distances *z* along the plasma *Y* axis. Two spectrometers were used: 1/8 m Oriel spectrometer (10 and 25 μm slits) with two different gratings (1200 and 2400 grooves×mm^{-1}) in the spectral region 2000-11000 Å at a resolution of ~1.3 Å in first-order (1200 grooves mm^{-1} grating), and an ISA Jobin Yvon Spex (Model HR320) 0.32 m equipped with a plane holographic grating (2400 grooves mm^{-1}) in the spectral region 2000-7500 Å at a resolution of ~0.12 Å in first-order. Two detectors were attached to the exit focal plane of the spectrographs and used to detect the optical emissions from the laser-induced plasma: an Andor DU420-OE (open electrode) CCD camera (1024x256 matrix of 26x26 $μm^2$ individual pixels) with thermoelectric cooling working at –30 ºC; A 1024×1024 matrix of 13×13 $μm^2$ individual pixels ICCD (Andor iStar DH-734), with thermoelectric cooling working at –20 ºC. The low noise level of the CCD allows long integration times and therefore the detection of very low emission intensities. The spectral window in high-resolution experiments was about 12 nm. The intensity response of the detection systems was calibrated with a standard (Osram No.6438, 6.6-A, 200-W) halogen lamp and Hg/Ar pencil lamp. Several (Cu/Ne, Fe/Ne

and Cr/Ar) hollow cathode lamps (HCL) were used for the spectral wavelength calibration of the spectrometers.

In time-resolved measurements, for synchronization, the CO_2 laser was operated at the internal trigger mode and ICCD detector was operated in external and gate modes. The external trigger signal generated by the laser was fed through the scope and delay generator into the back of the ICCD detector head. The total insertion delay (45 ± 2 ns) is the total length of time taken for the external trigger pulse to travel through the digital delay generator and gater so that the ICCD will switch on. The time jitter between the laser and the fast ICCD detector gate was about ± 2 ns. The delay time t_d is the time interval between the arrival of the laser pulse on the metal mesh and the activation of the ICCD detector. The gate width time t_w is the time interval during which the plasma emission is monitored by the ICCD. Both parameters were adjusted by the digital delay generator of the ICCD detector. The CO_2 laser pulse picked up with the photon drag detector triggered a pulse generator (Stanford DG 535) through the scope and this pulse was used as external trigger in the ICCD camera. The laser pulse and the gate monitor output were displayed in a digital oscilloscope. In this way, by using the output of the photon drag detector, the oscilloscope, the delay pulse generator and the gate monitor output of the ICCD camera, the gate width time t_w and the delay time t_d could be adjusted without insertion time.

5. Results and discussion

When a gas is irradiated by CO_2 laser lines of sufficient power, a visible breakdown occurs. The onset of LIB in air is a sudden dramatic event involving the production of more than $\sim 10^{16}$ electron-ion pairs and the emission of radiation characteristic of the gas-plasma. Figure 2 shows a series of images of the LIB nitrogen (up to the left), oxygen (up to the right), air (below to the left) and helium (below to the right) plasma at different times of the experiment. Although the laser-induced plasma appears spatially uniform to the naked eye, it is indeed elongated along the direction of the incoming carbon dioxide laser beam. For a laser power density around 4.5

$GW \times cm^{-2}$, the laser-induced plasma may be ≈ 6 cm long and a few centimeters in diameter. A number of plasma lobes can be distinguished as well as diffuse, luminous cloud surrounding the central plasma core. The observations of the LIB geometry during the experiments indicate that the actual plasma region is not spherical, but elongated in the direction of the laser beam propagation. There is an expansion back toward the laser that essentially fills the converging cone of the CO_2 laser radiation. The growth of the plasma in the direction opposite to the laser beam had lead to the model of a radiation-supported detonation wave (Section 2.6). A shock wave propagates from the focal region (a point at the centre of the cell) into the gas and absorption of energy from the laser beam drives the shock wave, causing it to spread. The structure of the LIB plasma is complex, and indeed there may be several distinct plasma regions produced along the laser beam axis. This multiple collinear plasmas in gases at pressures around the atmospheric level are observable by the naked eye. The CO_2 laser pulse remains in the focal volume after the plasma formation for some significant fraction of its duration and the plasma formed can be heated to very high temperatures and pressures by IB absorption. Since plasmas absorb radiation much more strongly than ordinary mater, plasmas can block transmission of incoming laser light to a significant degree; a phenomenon known as plasma shielding [51]. The high temperatures and pressures produced by plasma absorption can lead to thermal expansion of the plasma at high velocities, producing an audible acoustic signature, shock waves, and cavitation effects. The plasma also tends to expand back along the beam path toward the laser, a phenomenon known as moving breakdown. The shock wave heats up the surrounding gas which is instantaneously transformed in strongly ionized plasma.

5.1 LIBS of Nitrogen

In this section we present our results on the large-scale plasma produced in nitrogen gas at room temperature and pressures ranging from 4×10^3 to 1.2×10^5 Pa by high-power TEA- CO_2 LIB plasma [18]. The time-integrated spectrum of the generated plasma is dominated by emission of

strong N^+ and N and very weak N^{2+} atomic lines and molecular features of $N_2^+(B^2\Sigma_u^+\text{-}X^2\Sigma_g^+)$, $N_2^+(D^2\Pi_g\text{-}A^2\Pi_u)$, $N_2(C^3\Pi_u\text{-}B^3\Pi_g)$ and very weak $N_2(B^3\Pi_g\text{-}A^3\Sigma_u^+)$. Figure 3 displays an overview of the optical emission spectrum of LIDB in nitrogen (2000–9565 Å) compared with atomic lines of N, N^+ and N^{2+} [45]. Strong atomic N^+ lines dominate the spectrum but, atomic N lines (about 3 times weaker) and very weak N^{2+} lines (about 10^2-10^3 times weaker) also are present. The assignments of the atomic N (mainly in the 5700–9565 Å spectral region), N^+ (2000–6000 Å) and N^{2+}(2000–5500 Å) individual lines are indicated by stick labels. In the upper part of figure 3 we indicate in a column graph, the relative intensities of atomic observed N, N^+ and N^{2+} lines tabled in NIST Atomic Spectral Database [45]. There is a good agreement between line intensities tabulated in NIST and the measured intensities observed here for N, N^+ and N^{2+}. The spectrum of fig. 3 has been obtained with six successive exposures on the CCD detector using a 1/8 m Oriel spectrometer (1200 grooves/mm grating). In addition to identified atomic lines, molecular bands associated to N_2^+ and N_2 diatomic molecules are observed. The analysis of the molecular emission has already been used for a long time to get information on the structure and symmetry of excited states [46-48]. Studies of the electronic spectra of N_2 and N_2^+ in a number of discharge tubes, such as electrodeless microwave discharges and conventional *ac* and *dc* discharges, are well known. In many electrical discharges, the most prominent electronic transitions of N_2 are the first positive $B^3\Pi_g\text{-}A^3\Sigma^+_u$ system (between 480 and 2530 nm) and the second positive $C^3\Pi_u\text{-}B^3\Pi_g$ system (between 270 and 550 nm) [52]. For the electronic states implied in the electronic transitions of N_2(C-B and B-A) and N_2^+(B-X and D-A) the vibrational quanta $\Delta G(v+½)$ in the upper and lower electronic states have similar magnitudes and therefore the vibrational transitions with $\Delta v=v'\text{-}v''$ constant (sequences) appear quite close. The known part of the C-B second positive system of molecular nitrogen consist of the Δv = 4, 3, 2, 1, 0, -1, -2, -3, -4, -5, -6 and -7 triple-headed band sequence, all degraded to the violet. A sharp cutting-off of the rotational in v'=4 vibrational level of the C state is observed, which Herzberg [53] attributed to a predissociation. Pannetier *et al* [54] observed the 5-5 band of the C-B system with band-head at 3259.2 Å. Also Tanaka and Jursa [55]

studied this band system with high intensity in the aurora afterglow observed for weak red-degraded triplet bands originate from *v'*=5 ($C^3\Pi_u$). Perturbations of various types in the $C^3\Pi_u$ state of molecular nitrogen were also observed. Moreover, the most prominent electronic transitions of N_2^+ are the first negative $B^2\Sigma_u^+$-$X^2\Sigma_g^+$ system (between 280 and 590 nm) and the $A^2\Pi_u$-$X^2\Sigma_g^+$ Meinel system (550 and 1770 nm) [52]. The A-X Meinel bands for nitrogen cation were first identified in the aurora borealis [56]. The analysis of these band systems of N_2 and N_2^+ was accomplished in the early work of many authors and played an important part in the development of our understanding of the spectra of diatomic molecules.

In order to assign the molecular features of the LIDB in nitrogen, its spectrum is compared to that of the *dc* electric glow discharge at low pressure (~5 Torr). Typical spectra recorded with the oriel spectrometer (25 μm slit and grating of 1200 grooves/mm) after CO_2 laser excitation and in the cathode glow discharge of N_2 are given in figure 4. A global analysis of the latter allows one to distinguish the second positive C-B system (between 270 and 530 nm) and the first positive B-A system (between 570 and 970 nm) of N_2 and very weak emissions corresponding to the first negative B-X system of N_2^+ ions. Moreover, spectroscopic measurements performed on the dc electric glow in N_2 spectrum showed that although numerous molecular bands appear, nitrogen atomic lines are not present. Besides, the second positive system of N_2 and the first negative system of N_2^+ spectra are frequently observed simultaneously in plasma containing nitrogen. In the glow discharge in N_2 at 5977.4 Å, the 0-0 band of the $c_4{}^1\Pi_u$-a"$^1\Sigma_g^+$ Ledbetter Rydberg series [57] of nitrogen is observed overlapped with the 8-4 band sequence of the first positive B-A system. The LIB emission spectrum of N_2 (figure 4) shows six red-degraded heads in the region 225-275 nm which were readily assigned to the Δv=0 (v=0, 1, …6) band sequence of the $D^2\Pi_g$-$A^2\Pi_u$ Janin-d'Incan system [52] of N_2^+. In the spectral range between 2700-5300 Å, the second positive system of N_2(C-B) and the first negative system of N_2^+(B-X) spectra are observed simultaneously. Table 1 lists the different molecular species that have been observed in the LIB spectrum of nitrogen.

In order to investigate the different electronic bands of N_2 and N_2^+ both LIDB and high-voltage dc electric glow discharge spectra were recorded with a resolution of ~0.12 Å by a ISA Jobin Yvon Spex 0.32 m spectrometer. The high-resolution of LIB spectrum allowed us to resolve partially the vibrational bands of the second positive C-B system of N_2 and the first negative B-X system of N_2^+. Both spectra have been obtained with forty successive exposures on the CCD camera in the spectral region 2000-7500 Å. In the high-resolution spectra, no new processes were detected but allow us to identify unequivocally the band structure of the different transitions. As examples, figure 5(a)-(f) shows a comparison between two spectra, the lower one obtained for the high-voltage dc electric discharge, and the upper one recorded in the LIB experiment. We indicate with italic the position of the band-head (v'-v") of first negative system of N_2^+(B-X) while in regular typeface the bands of the second positive system of N_2(C-B). The upper panel of fig. 5(a) shows the LIB emission spectrum of nitrogen in the spectral region 2925-3175 Å of nitrogen. Assignment of the emission band heads is shown in table 1 and indicated also on the spectra. The two sets of three blue degraded band heads (2925-2980 Å) and (3105-3165 Å) are readily assigned to the $\Delta v=2$ and $\Delta v=1$ sequences of the second positive system of N_2(C-B), respectively. The series of bands between 3020-3095 Å belong to any of the bands 11-7, 4-1 and 3-0 of the first negative system of N_2^+(B-X). The lower panel, corresponding to the dc electric glow discharge of nitrogen at low pressure, shows practically the same bands with different intensity distributions and spectral widths. In the spectrum of the lower panel of fig. 5(b) (nitrogen electric glow discharge) we easily identified five bands of the $\Delta v=0$ sequence and the 1-0 band of the second positive system of N_2(C-B). The main intensity is observed for the dominant transition N_2(C, $v'=0$)→(B, v"=0) which corresponds to the most intense nitrogen laser line at 3371 Å. However, this simple picture changes drastically in the LIB emission spectrum of nitrogen excited by the CO_2 laser, being now the 0-0 band very weak. A large number of additional strong bands mainly in the region 3260-3410 Å are detected in the LIDB spectrum and can be attributed to emissions from the first negative system of N_2^+ (especially for $\Delta v=2$). The B-X system of N_2^+ has been

observed over a wide range of vibrational levels. The highest values so far observed are *v'*=29 for the excited B state and *v"*=23 for the X state. The main bands of this system lie in the $-2 \leq \Delta v \leq 2$ with $v' < 5$ sequences and all of these bands are blue degraded. However under certain circumstances many more bands, some red degraded, are observed, most being tail bands of these sequences. The observed bands with $v' \leq 7$ and also those with $8 \leq v' \leq 11$ and $\Delta v < -1$ are shaded to the violet. All the observed bands with $v' \geq 12$ and those with *v'*=10 and 11, $\Delta v \geq 0$ are shaded to the red although some bands appear headless. These bands are so-called tail bands taking place a reversal in the successions of the bands in the sequence. Moreover, in the bands of the first negative system of N_2^+ have been observed numerous rotational line displacements and intensities anomalies arising from perturbations in the B state. The perturbing state is $A^2\Pi_u$. In the Deslandres table listing the observed band heads, there is a pronounced gap in on arm of the Condon locus, and a less marked one in the other [52]. Franck-Condon factors indicate that the missing bands should be as intense as many of the observed. The few bands observed in the region of the gap are 8-6 and 9-8, which are headless and the 10-9 and 10-8 which have no definite heads. The missing bands coincide with the strong bands of either first negative system of N_2^+(B-X) or the second positive system of N_2(C-B), and are difficult to detect. In the spectrum of the lower panel of fig. 5(c) corresponding to the nitrogen electric glow discharge we easily identified several bands of the $\Delta v=-1$ sequence and two weak 4-6 and 3-5 bands of the second positive system of N_2(C-B). In this spectral region (3425-3675 Å) the most intense bands are due to the transitions N_2(C, v'=0)→(B, v"=1) and N_2(C, v'=1)→(B, v"=2), also present in the LIB emission spectrum of nitrogen in the upper panel of fig. 5(c). As in the previous cases, the LIB emission spectrum excited by the CO_2 laser changes drastically regarding the emission spectrum of nitrogen electric glow discharge. In it a large number of additional strong bands corresponding mainly to the $\Delta v=+1$ sequence B-X band system of N_2^+ are detected which are partially overlapped by the weak bands of the C-B system of N_2. For low *v'* the 1-0, 2-1, 3-2 … bands of the B-X system of N_2^+ are degraded to shorter wavelengths and for high v' values the bands are degraded to longer

wavelengths (tail bands). In the nitrogen electric glow discharge spectrum [lower panel of fig. 6(d)] we identified 3-6, 4-7, 0-2, 1-3 and 2-4 bands of the second positive system of N_2(C-B) and 0-0, 1-1 and 2-2 bands of the first negative system of N_2^+. In this spectral region (3675-3935 Å) the most intense band is the 0-2 band of N_2(C-B). The LIB emission spectrum in this region hardly shows bands of the second positive system of N_2(C-B). However, this emission spectrum exhibits a large number of bands corresponding mainly to the $\Delta v=0$ sequence B-X band system of N_2^+. In the spectra of the lower panel of figs. 5(d)-(f) (nitrogen electric glow discharge) we identified several bands of the second positive system of N_2(C-B), indicated on the spectra, and some very weak bands of the first negative system of N_2^+. As in the previous cases, the spectra change drastically in the LIDB emission of nitrogen excited by the CO_2 laser. A large number of N^+ and N^{2+} atomic lines and additional strong bands of the first negative system of N_2^+ are now present.

To understand the different processes involved in the analyzed emission, Rydberg-Klein-Rees (RKR) potential energy curves for some bound electronic states of N_2 and N_2^+ have been calculated. The potential energy curves for the $X^1\Sigma_g^+$, $A^3\Sigma_u^+$, $B^3\Pi_g$, $C^3\Pi_u$ states of N_2 and $X^2\Sigma_g^+$, $A^2\Pi_u$, $B^2\Sigma_u^+$, $C^2\Sigma_u^+$ and $D^2\Pi_g$ states of N_2^+ were obtained from the experimental information reported by Huber and Herzberg [58] and Laher and Gilmore [59]. Figure 6 shows the calculated RKR potentials and associated transitions for electronic states of N_2 and N_2^+ which can be relevant to interpret the results of the present work. Many perturbations are known in molecular states of nitrogen although a depth explanation of these features in terms of mixing of electronic states is not yet available. A useful graphical summary of many potential energy curves has been reported by Gilmore [60]. Perturbations are often accompanied by complex intensity irregularities as happens in the first negative system of N_2^+. Whereas the vibrational and rotational constants run quite normal for the $X^2\Sigma_g^+$ state of N_2^+, this is not at all the case for the $B^2\Sigma_u^+$ electronic state. Both the B_v and $G(v)$ curves versus the vibrational quantum number v have unusual shapes. This can be interpreted as caused by a strong mutual vibrational perturbation between the $B^2\Sigma_u^+$ and $C^2\Sigma_u^+$ states of the same species of N_2^+ (see fig. 6). As this perturbation is homogeneous (i.e.,

$\Delta\Lambda=0$) the shifts in both levels will be nearly independent of J producing that the $B^2\Sigma_u^+$ potential curve to flatten out in the middle of its energy range. The minimum of the $C^2\Sigma_u^+$ potential energy curve should be moved to smaller internuclear distances. There are also observed numerous rotational perturbations in the B-X system of N_2^+, caused by an interaction between the $A^2\Pi_u$ and the $B^2\Sigma_u^+$ states.

The excitation temperature T_{exc} was calculated from the relative intensities of some N^+ ionic lines (3400–4800 Å spectral region) according to the Boltzmann equation (3.16). The estimated excitation temperature was T_{exc}= 21000±1300 K. However, if the excitation temperature is determined using only the relative intensities of N atomic lines (7300–8800 Å spectral region) a value of T_{exc}=7900±1300 K is obtained. This behaviour is observed by other authors [61] and may be interpreted to result from the different emissivity distributions of neutral atoms and ion lines. The emissivity of the ion lines is produced, on the average, near the inner region with higher temperature. On the contrary, the emissivity of the neutral atom lines comes, on the average, from the low temperature region close to the plasma front, where the neutral atom density is higher. The intensity measurements correspond to the integration of the local emissivity values along the line-of-sight, integrated in turn in the perpendicular directions. As a consequence, the neutral atom Boltzmann plot provides a temperature value which is a certain average of the low-temperature values in the plasma (7900 K), whereas the temperature obtained from the ion Boltzmann plot (21000 K) averages the values existing in the high-temperature region. On the other hand, we have carried out simulations of the $\Delta v=+1$ sequence of B-X band of N_2^+ for different vibrational temperatures finding that a value around 20000 K reasonably reproduces the experimental spectrum. Also, if we consider a temperature of 7900 K the ionization degree obtained by means of the Saha equation is of 0.00064. Such a low ionization degree does not justify the observed emission spectra of N^+ and N_2^+. Keeping in mind these results, the temperature obtained from relative intensity of N^+ atomic lines (21000±1300 K) was chosen as the first approximation for the excitation temperature.

5.2 LIBS of Oxygen

In this section we present our recent results on LIBS in oxygen gas and pressures ranging from 4.6 to 75 kPa was studied using a high-power transverse excitation atmospheric CO_2 laser (λ=9.621 and 10.591 μm; τ_{FWHM}=64 ns; power densities ranging from 0.87 to 6.31 GW×cm^{-2}) [20]. For the present experiments the measured focused-spot area was 7.85×10^{-3} cm^2. This value is higher than the calculated area (2.2×10^{-4} cm^2) obtained from the beam waist (Eq. 1.7). This fact is due to the non-Gaussian profile of the CO_2 laser beam. Moreover the CO_2 laser beam passes through a circular aperture of diameter 17.5 mm. For this diaphragm the calculated divergence angle for the laser beams at 9.621 and 10.591 μm are 1.3 and 1.5 mrad, respectively. Thus, considering the total beam divergence (~4.4 mrad), the calculated diameter of the focused TEA-CO_2 laser (beam waist) is 1.06 mm, which is very similar to the measured value (~1 mm). If the focal region of the laser beam is assumed to be cylindrical in shape, the spot size in terms of length *l* (Eq. 1.8) of the focused TEA-CO_2 laser is 6.0 mm, which is similar to the measured value (~7 mm). For the different pulse laser energies measured in LIB of oxygen, the calculated laser peak power (Eq. 1.1), intensity (Eq. 1.2), fluence (Eq. 1.3), photon flux (Eq. 1.4), electric field (Eq. 1.5) and pressure radiation (Eq. 1.6) are given in Table 2.

Figures 7(a-f) display an overview of the low-resolution LIB emission spectrum (2320-9690 Å) in oxygen at a pressure of 53.2 kPa, excited by the 10P(20) line of the CO_2 laser, and assignment of the atomic lines of O, O^+, O^{2+}, N and N^+ [45]. Strong atomic O lines dominate the spectrum but, ionic O^+ lines (about 8 times weaker) and weak O^{2+} lines (about 150 times weaker) also are present. Some atomic and ionic nitrogen lines were also present, as well as, the first negative band system 330-400 nm corresponding to the transition $B^2\Sigma_u^+ - X^2\Sigma_g^+$ in N_2^+. In the acquisition of the spectrum of the Fig. 7(d-f) a cut-off filter was used to suppress the second order intense UV oxygen atomic lines. This cut-off filter produces a decrease of the intensity with regard to the spectra of the Fig. 7(a-c). In order to get more insight into LIB of oxygen and to

obtain an unambiguous assignment of the emission lines, we have scanned the corresponding wavelength regions with higher resolution (~0.10 Å in first-order), which was sufficient to distinguish clearly between nearly all observed lines. The spectra have been obtained with fifty successive exposures on the ICCD camera in the spectral region 1900-7500 Å. As example, Fig. 8(a-f) shows several spectra recorded in the LIB experiment. These LIB emission spectra were recorded under the following experimental conditions: oxygen pressure of 48.8 kPa, excitation line 10P(20) at 10.591 μm and CO_2 laser power density 4.28 GW×cm^{-2}. Figs. 8(a-f) display some details of the large features found in Figs. 7(a-f). No new features were observed in these high-resolution spectra. In these figures, multiplet transitions between different J levels for O^+ and O^{2+} are observed. In some cases these multiplet structures are not completely resolved due to Stark broadening of ionic lines. The spectral features clearly show the complexity of the relaxation process and bring out the possibility of cascading processes.

The excitation temperature was calculated from the relative intensities of several O^+ (3270–3310 Å spectral region) and O^{2+} (2900–3350 Å spectral region) atomic lines and the slope of the Boltzmann plot (Eq. 3.16). The values of the λ_{ki}, g_k, A_{ki} and E_k for O^+ and O^{2+} selected atomic lines were obtained from the NIST Atomic Spectral Database [45]. The excitation temperatures were determined under the following experimental conditions: oxygen pressure of 48.8 kPa, excitation line 10P(20) at 10.591 μm and CO_2 laser power density 4.28 GW×cm^{-2}. The obtained excitation temperatures, in the case of O^+ and O^{2+}, were 23000 ± 3000 K and 31500 ± 1600 K, respectively (Fig. 9). This behavior can be due to the different quenching rate coefficients between each species. Also this fact may be interpreted to result from the different emissivity distributions of single ionized and double ionized oxygen lines.

When LIB is produced in oxygen under high intensity laser radiation, some molecules can obtain an energy that exceeds the binding energy. Also some of their electrons become so energetic that the atoms and molecules ionize. Taking into account our experimental spectral observations, at these high temperatures oxygen becomes a mixture mainly of primary O_2, O, O^+,

O^{2+} and electrons. The transition between a gas and plasma is essentially a chemical equilibrium which shifts from the gas to plasma side with increasing temperature. Let us consider the first two different ionization equilibria of oxygen:

$O\ (2s^2 2p^4\ {}^3P_2\ ) \leftrightarrow O^+(2s^2 4p^3\ {}^4S^0_{3/2}) + e + I_P(O - I)$,

$O^+(2s^2 2p^3\ {}^4S^0_{3/2}) \leftrightarrow O^{2+}(2s^2 2p^2\ {}^3P_0\ ) + e + I_P(O - II)$,

where the first two ionization potentials for oxygen are $I_P(O-I) = 13.618\,eV$, and $I_P(O-II) = 35.121\,eV$ [62]. Taking into account the consideration of section 3.6, we can obtain the ionization degree. Fig. 10 shows the ionization degree $N_i/(N_0+N_i)$ of O and O^+, plotted as a function of the gas temperature T at a constant total pressure $P=(N_0+n_e+N_i)k_BT$ of 53.2 kPa. The graph shows that oxygen is already fully ionized at thermal energies well below the first ionization-energy of 13.618 eV (equivalent to 158000 K). If we consider a temperature of 23000 K, the ionization degrees of O and O^+ obtained by means of the Saha equation are 0.994 and 0.022, respectively. For T=31500 K, the ionization degrees of O and O^+ obtained by means of the Saha equation are 0.999 and 0.34, respectively. These so high values of the ionization degrees justify the observed emission spectra.

The electron number density was obtained by considering the discussion reported in section 3.4. The Doppler line widths for some lines of O^+ for different temperatures are shown in Fig. 11. In our experiments, for O^+ lines, the Doppler line widths are 0.07-0.12 Å at 23000 K. The choice of plasma emission for n_e measurements is made to ensure that the O^+ spectral lines are sensitive enough to Stark effect and do not suffer from interference by other species. The estimation of electron density n_e has been carried out by measuring the broadening of the spectral profiles of isolated lines of O^+ (2738, 3386, 3809, 4075, and 4418 Å) from the high-resolution spectra. The electron impact parameters for the different O^+ lines were approximated to a first-order exponential decay. The electron number densities of the laser-induced plasma were determined from the high-resolution emission spectra in oxygen at a pressure of 48.8 kPa, excited by the CO_2 laser at 10.591 μm with a power density of 4.28 GW×cm^{-2}. A Lorentz function was

used to fit the spectra. In order to extract the Stark broadening from the total experimentally measured line broadening, we have to previously deconvolute the different effects that contribute to the broadening of the spectral line: The instrumental, Doppler and Stark broadenings. Electron densities in the range $(3.5\text{-}16.5)\times10^{16}$ cm^{-3}, with an estimated uncertainty of 10%, were determined from the Stark broadening [Eq. (3.12)] data of several singly ionized oxygen lines.
At the evaluated temperature of 23000 ± 3000 K, Eq. (3.4) yields $n_e\approx(0.54\text{-}2.3)\times10^{16}$ cm^{-3}. These electron densities are lower to deduced values from the Stark broadening $(3.5\text{-}16.5)\times10^{16}$ cm^{-3}, approximately one order of magnitude. Based on these calculations, the validity of the LTE assumption is supported.

The interactions between the incoming laser radiation and the gas sample depend upon numerous variables related to the laser and the gas. These variables include laser wavelength, energy, spatial and temporal profile of the laser beam, and the thermal properties of the sample. The incident beam is partially reflected and partially absorbed by the bulk to a degree that depends on the nature of the gas and the temperature it reaches under laser irradiation. LIBS spectra of oxygen obtained by laser irradiation at the different wavelengths are compared in Fig. 12. These high-resolution LIB emission spectra in oxygen were obtained to a pressure of 48.8 kPa, excited by two TEA-CO_2 laser wavelengths at 10.591 μm (I_W=6.31 GW×cm^{-2}) and 9.621 μm (I_W=5.36 GW×cm^{-2}). The spectral range was chosen in order to detect both single and double ionized oxygen species. Also this spectral region has been selected to show differences in signal intensity and background emission in detail. The first remark that we should make is that the background continuum emission after the same optimization was performed on the data acquisition window is much stronger for spectrum produced by the 10.591 μm laser line. This is due to the higher laser power density (I_W=6.31 GW×cm^{-2}) and the higher absorption in the plasma caused by the IB, whose cross-section is proportional to $\lambda^3[1\text{-}\exp(-hc/\lambda k_B T)]^{-1}$ or approximately λ^2 (T is the electron temperature during the electron avalanche or cascade growth of ionization and λ is the laser excitation wavelength). The spectral lines of O^+ and O^{2+}(2983.78, 3017.63, 3023.45, 3043.02,

3047.13, 3059.30 Å) were clearly observed. It is clear that the ionic spectral lines for both O^+ and O^{2+} were enhanced by a factor of 4 when the LIBS is induced by the TEA-CO_2 laser at 10.591 μm. Besides, the irradiation at this wavelength favors the formation of the doubly ionized species (~ 30%), as it is obtained from the ratio of the intensities of the O^{2+} and O^+ lines. Moreover, plasma electron densities were determined from Stark broadening of the O^{2+} double ionized line at 2983.78 Å. The measured electron densities for the LIB emission spectra in oxygen were $(3.5\pm0.2)\times10^{16}$ cm^{-3} and $(3.2\pm0.2)\times10^{16}$ cm^{-3} for excitation at 10.591 μm and 9.621 μm, respectively. Values of the electron impact half-width W for O^{2+} were taken from the reported values given by Sreckovic *et al* [63]. It is noted that the emission intensity for O^+ and O^{2+} shows different picture than the electron density possibly due to the effect of the laser wavelength.

To see the effect laser irradiance the measurements were also carried out at different laser fluences. Optical emission spectra of the oxygen plasma plume at a pressure of 48.8 kPa as a function of the laser intensity are shown in Figs. 13(a) and 13(b). These spectra were recorded after the incidence of only one pulse of the TEA-CO_2 laser. The data were measured at a delay of 20 ms. An increase of atomic/ionic emission intensity and of the doubly ionized O^{2+} formation respect to O^+ with increasing the laser irradiance was observed. Also the background increases with the laser power. At higher laser power densities (6.31-4.28 GW cm^{-2}), the spectral lines are more broadened than at lower power densities as a result of the high pressure associated with the plasma. It is assumed that at higher laser fluence the LIB plasma is more energetic and more ionized.

The emission characteristics of the laser-induced plasma are influenced by the composition of the gas atmosphere. The pressure of the gas is one of the controlling parameters of the plasma characteristics, as well as the factors related to the laser energy absorption. Also the presence of air gas (vacuum conditions) during the LIB process has consequences on the expansion dynamics. An interesting observation was the effect of the oxygen pressure. Nanosecond TEA CO_2-laser produced plasma emission has been characterized as a function of oxygen pressure. Experiments

were performed in the pressure interval from 8 to 50 kPa and at pulse energy of 3161 mJ. Fig. 14 shows LIB emission spectra at various oxygen pressures, excited by the 10.591 μm line at a power density of 6.31 GW cm^{-2}. As can be seen in Fig. 14, the intensities of different spectral lines of O^+ and O^{2+} increase with decreasing pressure, reach a maximum at about 12.5 kPa, and then decrease for lower pressures. Characteristic emission lines from O^+ and O^{2+} elements exhibited significant enhancement in signal intensity at a few kPa oxygen pressure as compared to high pressures below atmospheric pressure. However, the ratio of the intensities among the O^{2+} and O^+ lines remains the same at all pressures. The measurements indicate enhancement due to a longer lifetime of the plasma expanding to a larger size at lower oxygen pressures. Further reduction in oxygen pressure down to ~ 12.5 kPa resulted in a decrease in signal intensity, as a result of a reduction of collisional excitation of the emission lines which occurs when the plasma plume expands into the oxygen atmosphere.

5.3 LIBS of Air

A spectroscopic study of ambient air plasma, initially at room temperature and pressures ranging from 32 to 101 kPa, produced by TEA-CO_2 laser (λ=9.621 and 10.591 μm; $\tau_{FWHM}\approx$64 ns; power densities ranging from 0.29 to 6.31 GW×cm^{-2}) has been carried out in an attempt to clarify the processes involved in laser-induced breakdown (LIB) air plasma. To understand the detailed aspects of laser-beam interaction with air and recombination processes following the breakdown, OES studies of the emission spectra from the plasma offer the most convenient method. The strong emission observed in the plasma region is mainly due to electronic relaxation of excited N, O and ionic fragments N^+. The medium-weak emission is due to excited species O^+, N^{2+}, O^{2+}, C, C^+, C^{2+}, H, Ar and molecular band systems of $N_2^+(B^2\Sigma_u^+\text{-}X^2\Sigma_g^+)$, $N_2(C^3\Pi_u\text{-}B^3\Pi_g)$, $N_2^+(D^2\Pi_g\text{-}A^2\Pi_u)$ and $OH(A^2\Sigma^+\text{-}X^2\Pi)$. Figure 15(a-f) displays an overview of the low-resolution LIB emission spectrum in air at atmospheric pressure, excited by the 10P(20) line of the CO_2 laser with an intensity of 2.2 GW×cm^{-2}, and assignment of the atomic lines of N, O, C, C^+, H, Ar, N^+, O^+, N^{2+},

O^{2+}, C^{2+} tabulated in NIST Atomic Spectral Database [45] and molecular bands of $N_2^+(B^2\Sigma_u^+$-$X^2\Sigma_g^+)$, $N_2^+(D^2\Pi_g$- $A^2\Pi_u)$, $N_2(C^3\Pi_u$-$B^3\Pi_g)$ and $OH(A^2\Sigma^+$-$X^2\Pi)$. Strong atomic N^+, N and O lines dominate the spectrum but, atomic lines of C, C^+, H, Ar, O^+, N^{2+}, O^{2+}, C^{2+} also are present. LIB spectrum of air was compared with the LIB spectra obtained in our laboratory for nitrogen [18] and oxygen [20]. The spectra have been obtained at higher resolution with fifty successive exposures on the ICCD camera in the spectral region 2000-7500 Å. As examples, Fig. 16(a-l) shows several spectra recorded in the air LIB experiment. These LIB emission spectra were recorded under the following experimental conditions: air pressure of ~101 kPa, excitation line 9P(28) at 9.621 μm and laser irradiance of 5.36 GW×cm^{-2}. Note that spectra of Figs. 15(a-f) and 16(a-l) were excited by two different laser wavelengths. No new features were observed in these high-resolution spectra. In these figures, multiplet transitions between different *J* levels for N^+ and O^+ are observed. In some cases these multiplet structures are not completely resolved due to Stark broadening of atomic/ionic lines. The spectral features clearly show the complexity of the relaxation process. In figures 16(a-l), a rather complex structure is observed, in consequence of the overlapping between rovibrational lines of different molecular band systems and atomic/ionic lines. Figure 16(a) displays the overlapping between some bands of the $N_2^+(D^2\Pi_g$-$A^2\Pi_u)$ system and some lines of N^+, O^+, C^{2+} and O^{2+}. In this spectrum the predominant emitting species is the triplet structure of N^+ $2s^22p(^2P^0)4d\ ^3F^0_{3,2,4} \rightarrow 2s^22p(^2P^0)4d\ ^3D_{2,1,3}$ around 2317 Å overlapped with the 0-0 band of the N_2^+(D-A) system. In the spectrum of figure 16(b), the most intense emitting species is the line of C $2s^22p(^2P^0)3s\ ^1P^0_1 \rightarrow 2s^22p^2\ ^1S_0$ at 2478.56 Å, and several ionic lines of O^+ $2s^22p^2(^3P)4p\ ^2D^0_{5/2} \rightarrow 2s^22p^2(^1D)3s\ ^2D_{5/2}$ at 2425.56 Å, O^+ $2s^22p^2(^1D)3p\ ^2D^0_{3/2} \rightarrow 2s^22p^2(^3P)3s\ ^2P_{1/2}$ at 2433.53 Å, and the doublet O^+ $2s^22p^2(^1D)3p\ ^2D^0_{3/2,5/2} \rightarrow 2s^22p^2(^3P)3s\ ^2P_{3/2}$ at 2444.25 Å and 2445.54 Å, respectively. Several medium intensity ionic lines of N^+ also overlapped with different bands of N_2^+(D-A) and many weak lines of O^{2+} and O^+ are also present. In the spectrum of figure 16(c), the most intense emitting species is the line of N^+ $2s^22p(^2P^0)4s\ ^1P^0_1 \rightarrow 2s^22p(^2P^0)3p\ ^1P_1$ at 3006.83 Å. This figure displays the overlapping between the N_2(C-B) v'=2-v"=0 band, OH(A-X)

Δv=0 sequence and many weak lines of O^+ and O^{2+}. In the spectrum of figure 16(d), $N_2^+(B^2\Sigma_u^+$-$X^2\Sigma_g^+)$ Δv=2 sequence and many weak lines of O^+ and O^{2+} are recorded. This spectrum shows the reversal of the bands from v'=11, which is due to the overlap between high vibrational quantum number bands with low quantum number bands. So, the first vibrational bands of N_2^+(B-X) (2-0, 3-1, 4-2 … and 10-8) are shaded to the violet and after reversal (11-9, 12-10, 13-12 …) are shaded to the red. In the spectrum of figure 16(e), the most intense emitting species is the line of N^+ $2s^22p(^2P^0)3p\ ^1S_0 \rightarrow 2s^22p(^2P^0)3s\ ^1P^0_1$ at 3437.15 Å. Many medium intensity ionic lines of O^+ and O^{2+}, weak molecular bands of N_2(C-B) and N_2^+(B-X) are also present. Surprisingly, the relative intensity of the 0-0 band head in the N_2(C-B) system is very weak. In the spectrum of figure 16(f), many medium intensity rovibrational molecular bands of N_2(C-B; Δv=-1 sequence) and N_2^+(B-X; mainly Δv=1 sequence) are observed. In the spectrum of figure 16(g), the most intense emitting species are the lines of O^+ $2s^22p^2(^3P)3p\ ^4S^0_{3/2} \rightarrow 2s^22p^2(^3P)3s\ ^4P_{3/2}$ at 3727.32 Å, O^+ $2s^22p^2(^3P)3p\ ^4S^0_{3/2} \rightarrow 2s^22p^2(^3P)3s\ ^4P_{5/2}$ at 3749.49 Å, N^+ $2s^22p(^2P^0)4s\ ^3P^0_2 \rightarrow 2s^22p(^2P^0)3p\ ^3P_2$ at 3838.37 Å and N_2^+(B-X) Δv=0 sequence. Several weak intensity ionic lines of O^+ and O^{2+} also overlapped with different bands of N_2^+(B-X) are also present. As in the spectrum of Fig. 16(d) a reversal of the bands for high vibrational levels is produced. So, the first vibrational bands of N_2^+(B-X) (0-0, 1-1, 2-2, …) are shaded to the violet and after reversal are shaded to the red. In the spectrum of figure 16(h), several strong intensity ionic lines of N^+, O^+ and N^{2+} also overlapped with different bands of N_2^+(B-X) Δv=0 sequence. The relative intensity of the 0-0 band head at 3914.9 Å in the N_2^+(B-X) system is quite weak and partially overlapped with one O^+ line. Nevertheless, the 0-0 band is the most intense of their band sequence. In this spectrum, many weak intensity rovibrational molecular bands of N_2^+(B-X) can be appreciated. The strong emission observed in figures 16(i-l) is mainly due to the relaxation of excited ionic fragments N^+ and O^+. In figure 16(j) various ionic lines overlap with molecular bands of N_2^+(B-X) transitions and produce rather complex structure, but this high-resolution spectra allow for a precise attribution of almost all observed transitions. The six lines of single ionized nitrogen between 4600-4650 Å correspond to the multiplet structure

of N^+ $2s^2 2p(^2P^0)3p\ ^3P^0_{J'} \rightarrow 2s^2 2p(^2P^0)3s\ ^3P^0_{J''}$. As it can see, the LIB of air includes mainly contributions of both nitrogen and oxygen. It should be noted that the nitrogen and oxygen line intensities maintain the proportions of the air composition.

On the other hand, excitation temperatures of 23400 ± 700 K and 26600 ± 1400 K were estimated by means of N^+ and O^+ ionic lines, respectively. Electron number densities of the order of $(0.5\text{-}2.4)\times10^{17}$ cm^{-3} and $(0.6\text{-}7.5)\times10^{17}$ cm^{-3} were deduced from the Stark broadening of several ionic N^+ and O^+ lines, respectively.

LIBS spectra obtained by laser irradiation at the different wavelengths are compared in Fig. 17. These high-resolution LIB emission spectra in air were obtained at atmospheric pressure, excited by two TEA-CO_2 laser wavelengths at 10.591 μm (I_W=6.31 GW×cm^{-2}) and 9.621 μm (I_W=5.36 GW×cm^{-2}). The spectral range was chosen in order to detect the emission lines of different atomic, single and double ionized species (C, C^+, N^+, O^+, O^{2+}). Both spectra have been obtained after the incidence of only one laser pulse. The relative intensities for different species practically do not change with the laser wavelength. The atomic C line at 2478.56 Å was enhanced when the LIBS is induced by the CO_2 laser at 10.591 μm. This fact is probably due to a self-absorption process in such resonance line. Figure 18 shows high-resolution LIB emission spectra in air at atmospheric pressure, excited by the CO_2 laser line at 9.621 μm (I_W=5.36 GW/cm^2), recorded with cell and without cell. We see similar intensities for O^+ and different bands of N_2^+(B-X) Δv=0 sequence in both spectra. However, the intensity of N^+ and N^{2+} lines was increased when the LIB is with cell. Also, there is a line in the spectra at ~3860 Å, possible due to H_2, which intensity increases without cell. This fact is probably caused by differences in relative humidity of air in both situations.

To see the effect that the laser irradiance has on the air breakdown measurements were also carried out at different laser intensities. Low-resolution LIB emission spectra of the air plasma at atmospheric pressure, excited by the TEA-CO_2 laser wavelength at 9.621 μm, as a function of the laser intensity is shown in Fig. 19. These spectra were recorded after the incidence of only one

pulse of the TEA-CO_2 laser. An increase of atomic/ionic emission intensity with increasing the laser irradiance was observed. Also the background increases with the laser power. At higher laser power densities (6.31-4.00 GW cm^{-2}), the spectral lines are more broadened than at lower power densities as a result of the high pressure associated with the plasma. It is assumed that at higher laser fluence the LIB plasma is more energetic and more ionized. In order to see the effect of the laser intensity on molecular band emission, high-resolution LIB emission spectra of the air plasma at atmospheric pressure, (excited by the TEA-CO_2 laser wavelength at 9.621 μm) as a function of the laser intensity is shown in Fig. 20. The assignment of this spectrum can be found in Fig. 4(f). An increase of molecular band intensity of $N_2^+(B^2\Sigma_u^+\text{-}X^2\Sigma_g^+)$ and $N_2(C^3\Pi_u\text{-}B^3\Pi_g)$ with increasing the laser intensity was observed.

Nanosecond TEA CO_2-laser produced plasma emission has been characterized as a function of air pressure. Fig. 21 shows LIB emission spectra in the pressure interval from 32 to 101 kPa, excited by the TEA-CO_2 laser (10.591 μm) at a power density of 6.31 GW cm^{-2}. As can be seen in Fig. 21, the intensities of different spectral lines of C, N^+, O^+, O^{2+} and N_2^+(D-A) molecular bands increase with increasing pressure, reach a maximum at about 79.6 kPa, and then decrease with higher pressures. The measurements indicate enhancement due to a longer lifetime of the plasma expanding to a larger size at lower air pressures (p<79.6 kPa). Further increase in air pressure above to ~ 79.6 kPa resulted in a decrease in signal intensity, as a result of a reduction of collisional excitation of the emission lines which occurs when the plasma plume expands into the air atmosphere.

The detection of the N_2^+(B-X) bands is of particular interest since it provides an estimation of the effective vibrational and rotational temperatures. The emission intensities of the N_2^+ Δv=-1 and Δv=0 band sequences were analyzed in order to estimate the molecular vibrational temperature T_{vib} (see section 3.5). Two Boltzmann plots (Equation 3.17) of the band intensities against the vibrational energy at the laser irradiance 5.36 GW×cm^{-2} are given in Fig. 22(a-b) along with the corresponding Franck-Condon factors. The estimated effective vibrational temperatures

were T_{vib}=12100 ± 700 K and 12000 ± 900 K, respectively. On the other hand, the emission intensities of the 0-0 ($B^2\Sigma_u^+$-$X^2\Sigma_g^+$) band of N_2^+ were analyzed in order to estimate the effective rotational temperature T_{rot}. In $^2\Sigma$-$^2\Sigma$ transitions both electronic states belong to Hund´s (b) coupling case (ΔN=±1) [46-48]. Each line of the *R* and *P* branches are doublet since they separate in two sublevels with $J=N\pm½$ each one subscripted with i=1, 2 (1 for $J=N+½$ and 2 for $J=N-½$)

$$R_i(N) = \tilde{\nu}_0 + F_i^{'}(N+1) - F_i^{''}(N), \tag{5.1}$$

$$P_i(N) = \tilde{\nu}_0 + F_i^{'}(N-1) - F_i^{''}(N). \tag{5.2}$$

In Eqs. (5.1) and (5.2) the *Q*-branch forms satellite branches, whose intensities are much lower than the main ones, very close to the corresponding *R* and *P* branches lines (called *R*-form or *P*-form *Q* branches) with wavenumbers:

$$^{R}Q_{21}(N) = \tilde{\nu}_0 + F_{i2}^{'}(N+1) - F_1^{''}(N), \tag{5.3}$$

$$^{P}Q_{12}(N) = \tilde{\nu}_0 + F_{i2}^{'}(N-1) - F_2^{''}(N). \tag{5.4}$$

The subscripts 21 and 12 indicate the transition which takes place from a term of the F_2 series to one of the F_1 series or vice versa:

$$F_1(N = J - \frac{1}{2}) = B_v N(N+1) + ... + \gamma \frac{N}{2}, \tag{5.5}$$

$$F_2(N = J + \frac{1}{2}) = B_v N(N+1) + ... - \gamma \frac{N+1}{2}. \tag{5.6}$$

In Eqs. (5.1)-(5.6) *N* is the total angular momentum excluding spin of nuclear rotation, $\tilde{\nu}_0$ is the wavenumber of the pure vibrational transition, B_v is rotational spectroscopic constant and γ is the spin-rotation coupling constant. Moreover, in the case of a molecule with two identical nuclei such as N_2^+, relative line intensities are affected by the nuclear spin (I=1). The nuclear spin governs the intensities through the Pauli exclusion principle; all wavefunctions are antisymmetric with respect to the interchange of fermions (half-integer spin particle) and symmetric with respect to the interchange of bosons (integer spin particle). Then the ratio of the statistical weights of the symmetric and antisymmetric rotational levels is I+1/I for bosons or I/I+1 for fermions. In the case

of N_2^+ the $B^2\Sigma_u^+$ electronic state has only odd J values and then the ratio of the statistical weights of the symmetric and antisymmetric rotational levels is 2/1.

The assignment of rotational spectrum of 0-0 $B^2\Sigma_u^+$-$X^2\Sigma_g^+$ band of N_2^+, recorded in experimental conditions indicated above, is shown in figure 23(a). In Fig. 23(b) we display the calculated fortrat diagram for P_1, P_2, R_1, R_2, ${}^RQ_{12}$ and ${}^PQ_{21}$ branches corresponding to this band. The alternation of the intensities of the rotational lines is observed.

To estimate the effective rotational temperature, we consider the J value for the maximum of the 0-0 band (B-X) of N_2^+ (J_{max}) (Section 3.5)

$$T_{rot} = \frac{2B_0hc}{k_B}(J_{\max} + \frac{1}{2})^2, \qquad (5.7)$$

being B_0 the rotational constant for v'=0 and J_{max} the total angular momentum at the maximum. This effective rotational temperature is found to be T_{rot}=1900 ± 100 K. As in any gas, temperature in LIB plasma is determined by the average energies of the plasma species (e^-, N_2, O_2, Ar, H, N, O, C, OH, N_2^+, N^+, O^+, N^{2+}, O^{2+}, C^+, C^{2+} etc) and their relevant degrees of freedom (translational, rotational, vibrational, and those related to electronic excitation). Thus, LIB plasmas, as multi-component systems, are able to exhibit multiple temperatures. In LIB for plasma generation in the laboratory, energy from the laser electric field is first accumulated by the electrons and, subsequently, is transferred from the electrons to the heavy particles. Electrons receive energy from the electric field and, by collision with a heavy particle, lose only a small portion of that energy. That is why the electron temperature in plasma is initially higher than that of heavy particles. Subsequently, collisions of electrons with heavy particles (Joule heating) can equilibrate their temperatures, unless time or energy are not sufficient for the equilibration (such as in LIB and pulsed discharges). The temperature difference between electrons and heavy neutral particles due to Joule heating in the collisional weakly ionized plasma is conventionally proportional to the square of the ratio of the electric field E to the pressure p. Only in the case of small values of E/p do the temperatures of electrons and heavy particles approach each other. Numerous plasmas are

characterized by multiple different temperatures related to different plasma particles and different degrees of freedom. Plasmas of this kind are usually called non-thermal plasmas. Although the relationship between different plasma temperatures in non-thermal plasmas can be quite sophisticated, it can be conventionally presented in LIB strongly ionized plasmas as T_e (electron temperature) > T_i (ions or excitation temperature) > T_{vib} > T_{rot}. In LIB non-thermal plasma studied here, electron temperature is about 10 eV, ions temperature ~2 eV, vibrational temperature ~1 eV, rotational temperature ~0.2 eV, whereas the gas temperature is close to rotational temperature.

The strong atomic and ionic lines observed in LIB spectra of air indicate the high degree of excitation/ionization and the high rate of the N_2, O_2 dissociation processes achieved in the plasma. As we mentioned in section 2.2, when a high-power laser beam of intensity I_W interacts with a gas, electrons involving the formation of laser-induced plasma can be generated through two main processes: MPI and EII both followed by electron cascade. The ionization rate in MPI varies as I_W^n where n is the number of photons needed to strip off an electron. MPI is relatively improbable for nitrogen and oxygen atoms or molecules in the ground state [N($2s^2 2p^3\ ^4S^0_{3/2}$), O($2s^2 2p^4\ ^3P_2$), $N_2(X^1\Sigma_g^+)$ and $O_2(X^3\Sigma_g^-)$], since their high ionization potentials (14.534, 13.618, 9.567 and 12.070 eV, respectively), means that more than 100 photons are required for these processes. Besides, the probability of simultaneous absorption of photons decreases with the number of photons n necessary to cause ionization. In general, this probability is $W_{MPI} \propto \Phi_W^n \propto F_E^{2n}$. Calculations of MPI probability (Eq. 2.4) for N, O, N_2 and O_2 give $W_{MPI} \cong 0$ s^{-1} for the CO_2 laser at λ=9.621 μm and I_W=4.5 GW×cm^{-2}. For example, for a 193 nm (ArF) at the laser intensity I_W=1 GW×cm^{-2} (n=2), the probability of MPI for O_2 gives W_{MPI}=1058 s^{-1}. EII consists on the absorption of light photon by free or quasifree electrons. These electrons in the focal volume gain sufficient energy, from the laser field through IB collisions with neutrals, to ionize mainly nitrogen and oxygen atoms, molecules or ions by inelastic electron-particle collision resulting in two electrons of lower energy being available to start the process again. EII is the most important process for the longer wavelengths used in this work. On the other hand, we have made experimental

measurements of breakdown threshold laser intensities of N_2, O_2 and ambient air (Section 2.4). The threshold power density is dependent on the kind of laser, laser wavelength, pulse length, beam size of the focal volume, and gas pressure. Breakdown thresholds of solids and liquids are usually lower than for gases. Experimental threshold power densities for air is measured for the TEA-CO_2 laser at λ=10.591 μm. The threshold power densities for air at a given pressure are measured in the two following manners. First the cell was evacuated with the aid of a rotary pump, to a base pressure of 4 Pa that was measured by a mechanical gauge and then it was filled with air up to the desired pressure. The TEA-CO_2 laser was fired and its energy transmitted through the cell was increased until the breakdown was observed in 50% of laser pulses. The threshold was easily determined because it was always associated with the appearance of a blued bright flash of light in the focal region, with a cracking noise, and the abrupt absorption of the laser pulse transmitted through the focal region. Another way to measure the threshold was to induce a previous breakdown at a pressure over the desired value, later the pressure is lowered and the energy adjusted until the breakdown begins with some probability, usually around 50%. This method is similar to induce the breakdown with energy in excess and to attenuate the laser until the spark disappears. In these cases it could be that initial free electrons have been produced by previous breakdowns and they are the seed of the avalanche process. In this last method the obtained threshold value is normally lower. The present experiments have shown that when high laser energy was used, air breakdown occurred easily and it was reproducible. When the laser energy was reduced to its threshold power density value, air breakdown became a sporadic event. Such sporadic behavior might be due to the difficulty of generating the seed electrons at the breakdown threshold values.

Figure 24 shows the measured breakdown threshold intensity for air, N_2 [18] and O_2 [20] as a function of pressure. We have measured the breakdown threshold intensity in air at atmospheric pressure finding 4.5×10^9 W×cm^{-2} (1.3×10^6 V×cm^{-1}) for an air fresh charge and 1.1×10^9 W×cm^{-2} (6.4×10^5 V×cm^{-1}) for an air non-fresh charge. As can be seen from Fig. 24, if a

breakdown has been previously induced in the gas (open symbol), the pressure range to induce the breakdown is bigger and the power density is lower than when no previous breakdown is induced (solid symbol). The number of free electrons is higher in conditions of previous breakdown than in the case of no previous breakdown, lowering the threshold for the plasma initiation. This has been observed by different authors. LIB threshold intensity of air at atmospheric pressure has been measured by Alcock *et al* [$\sim 4\times10^{10}$ W×cm^{-2} (Ruby, 0.3472 μm) and $\sim 10^{11}$ W×cm^{-2} (0.6943 μm)] [64], Haught *et al* ($\sim 4\times10^{14}$ W×cm^{-2}) [65], De Michelis ($\sim 4\times10^{10}$ W× cm^{-2}) [66], Ireland *et al* ($\sim 4\times10^{10}$ W×cm^{-2}) [67], Aaron *et al* ($\sim 4\times10^{14}$ W×cm^{-2}) [68], Phuoc and White ($\sim 2.5\times10^{12}$ W×cm^{-2}) [69], Tomlinson *et al* [$\sim 2\times10^{11}$ W×cm^{-2} (Ruby, 0.69 μm) and $\sim 7\times10^{10}$ W×cm^{-2} (Nd:YAG, 1.06 μm)] [70], Chan *et al* [$\sim 1.5\times10^{9}$ W×cm^{-2} (CO_2, 10.6 μm, Λ(diffusion length)=4.8×10^{-3} cm), $\sim 3\times10^{9}$ W×cm^{-2} (Λ=3.2×10^{-3} cm), and $\sim 7\times10^{9}$ W×cm^{-2} (Λ=1.6×10^{-3} cm)] [30], Kawahara ($\sim 7\times10^{10}$ W×cm^{-2}, Nd:YAG, 1.06 μm)] [71] and Zhuzhukalo *et al* [$\sim 7\times10^{10}$ W×cm^{-2} (focal length = 1.4 m) and $\sim 2\times10^{10}$ W×cm^{-2} (focal length =14 m)] [72]. Alcock *et al* [64] reported a decrease of the breakdown threshold intensity from $\sim 9\times10^{10}$ to $\sim 4\times10^{10}$ W×cm^{-2} at 0.3472 μm and $\sim 2\times10^{11}$ to $\sim 1\times10^{11}$ W×cm^{-2} at 0.6943 μm for air pressures between ~200 Torr and ~800 Torr. Chang *et al* [30] reported for several gases (O_2, N_2, air, He, and Ne) that the threshold power density decreases as the pressure increases and that it decreases as the focal volume increases. For air they reported a slow decrease with a minimum of the breakdown threshold intensity from $\sim 1.5\times10^{9}$ to $\sim 1\times10^{9}$ W×cm^{-2} at Λ=4.8×10^{-3} cm, $\sim 3\times10^{9}$ to $\sim 1.5\times10^{9}$ W×cm^{-2} at Λ=3.2×10^{-3} cm, and $\sim 10\times10^{9}$ to $\sim 5\times10^{9}$ W×cm^{-2} at Λ=1.6×10^{-3} cm for air pressures between ~200 Torr and ~10000 Torr. In this work, they used a CO_2 laser and the focal diameter range from 0.75×10^{-2} to 3×10^{-2} cm. Phuoc and White [69] reported a decrease of the breakdown threshold intensity from $\sim 2\times10^{13}$ to $\sim 2\times10^{12}$ W×cm^{-2} at 0.532 μm and $\sim 8\times10^{12}$ to $\sim 1\times10^{12}$ W×cm^{-2} at 1.064 μm for air pressures between 50 Torr and 3000 Torr. It has to be noted that we have obtained similar threshold power densities for air than those given by Chan [30], but lower values than reported in Refs. [64-72]. This fact can be related in part to the used focal length (24 cm) and beam size in the focal region (7.85×10^{-3} cm^2)

that is one order of magnitude, at least, higher that the values commonly used in the literature, favoring the probability of existence of free electrons to seed the process and decreasing the threshold laser intensity due to the lack of the diffusion losses.

It has been established [3-10] that the threshold photon flux density or equivalently the threshold power density for MPI varies with $p^{-1/n}$, where p is the gas pressure and n is the number of simultaneously absorbed photons (see section 2.4). Therefore, MPI predicts a very weak dependence of the threshold power density on pressure. However, as we can see from fig. 24, the breakdown threshold power density in air versus pressure shows a minimum around 5×10^4 Pa if previous breakdown have existed and 8×10^4 Pa without previous breakdown. Therefore, it can be seen from Fig. 24 that the pressure dependence is not in harmony with MPI which predicts a very weak $p^{-1/n}$ dependence for the threshold power density, while it is in qualitative agreement with electron cascade. A minimum in the variation of the threshold power density versus pressure is predicted by the classical theory [2-3, 23]. In our experiments, a minimum in the threshold power density versus pressure curve (fig. 24) is observed. Therefore, starting from our experimental observations and calculations, we can conclude that although, the first electrons must appear via MPI or natural ionization, electron impact is the main mechanism responsible for the breakdown in air.

5.3.1 Temporal evolution of the LIB plasma

The absorption of light and heating of a gas is of primary significance for important practical problems (the fire ball of an explosion, the heating of artificial satellites during re-entry into the atmosphere, detection of environmental pollutants, ignition systems, laser machining, inertially confined fusion, etc). In this section, time-resolved OES analysis for the plasma produced by high-power tunable IR CO_2 pulsed laser breakdown of air is presented [21]. In these series of experiments, the CO_2 pulsed laser (λ=10.591 μm, 64 ns (FWHM), 47-347 J/cm^2) was focused onto a metal mesh target under air as host gas at atmospheric pressure [21]. It was found that the CO_2 laser is favorable for generating strong, large volume air breakdown plasma, in which

the air plasma was then produced. While the metal mesh target itself was practically never ablated, the air breakdown is mainly due to electronic relaxation of excited N, O, C, H, Ar and ionic fragments N^+, O^+, N^{2+}, O^{2+}, C^+ and molecular band systems of $N_2^+(B^2\Sigma_u^+\text{-}X^2\Sigma_g^+$; $D^2\Pi_g\text{-}A^2\Pi_u)$, $N_2(C^3\Pi_u\text{-}B^3\Pi_g)$ and $OH(A^2\Sigma^+\text{-}X^2\Pi)$.

The difficulties arise on account of the imprecise definition of the extent of the focal region which, in turn lead to inadequate or inaccurate knowledge of the spatial- temporal characteristic of the beam intensity within the focal region for gases. On the other hand, it is well known that a pure gas plasma, due to the gas breakdown process, is produced when a TEA CO_2 laser is focused onto a metal sample at a gas pressure of around 1 atm, in which case practically all the laser irradiance is absorbed in the gas plasma [33, 73]. It is expected that, in some medium range pressures between 0.01 torr and 1 atm, both gas plasma and target plasmas are produced. In such a case, some interaction inevitable takes place between the gas and the target laser induced plasmas. The plasma is a mixture of electrons, atoms, molecules and ions, and mass from both the ablated target and the ambient gas. The interaction between the ejected mass (plume) and the surrounding air slows the expansion of the plasma. If a metal mesh is used as a target, low amount (if any) of ablated material will be formed and the spatial origin of gas breakdown process will be accurately defined independently of the laser fluence. After its formation in the vicinity of the metal mesh surface, the air breakdown plasma propagates towards the laser source at a supersonic speed. The shock wave heats up the surrounding air which is instantaneously transformed in strongly ionized plasma.

Two different types of spectra were recorded: time-integrated and time-resolved. In the acquisition of time-integrated spectra, a good signal to noise ratio has been obtained averaging each spectrum over several successive laser pulses. Typically the signals from 20 laser pulses are averaged and integrated over the entire emission time. In time-resolved measurements, the delay t_d and width t_w times were varied. It was verified that the plasma emission was reproducible over more than 7 ablation events by recording the same spectrum several times. The temporal history of

LIB air plasma is illustrated schematically in Fig. 25. The time for the beginning of the CO_2 laser pulse is considered as the origin of the time scale (t=0). Inserts illustrate some emission spectra recorded at different delay and width times at two observed distances of z=2.5 and 5 mm. The temporal shape of the CO_2 laser pulse is also shown.

The LIB spectra of air were measured at different delay and width times. In a first set of experimental measurements, the spectra have been obtained in the spectral region 2423-2573 Å, at a delay time ranging from 0 to 30 μs at 0.5 μs intervals and at an observed distance z from 1 to 10 mm. The spectral range was chosen in order to detect both single and double ionized oxygen species, several single ionized nitrogen lines and atomic carbon. Figure 26 illustrates the time-resolved evolution from laser-induced (106 J/cm^2) air plasma monitored at 0, 0.1, 0.7, 2, 3, 4, and 5 μs gate delays for a fixed gate width time of 0.5 μs and z=2.5 mm. One can see that after the laser pulse, the plasma emission consists in an intense continuum. This continuum radiation is emitted by the laser-induced plasma as a result of free-free and free-bound transitions. As seen in figure 26 during the initial stages after laser pulse ($t_d \leq 0.5$ μs), continuum emission dominates the spectrum. As time evolves (0.5 μs$\leq t_d \leq$3.5 μs), N^+, O^+ and O^{2+} emissions dominate the spectrum. These ionic lines decrease quickly for higher delay times, being detected up to ~ 4.5 μs. The emission lines become progressively narrower as a consequence of the electron number density distribution. It points out that the electron density and excitation temperature must decrease during the plasma expansion. As the delay is increased (t_d>3.5 μs) C atomic emission line dominates the spectrum. This atomic line decreases for higher delay times, being detected up to ~ 30 μs. The maximum intensity of continuum and spectral lines is reached after a characteristic time, depending on the observation distance z. Figure 27 shows time-resolved emission spectra from LIB (106 J/cm^2) in air collected at different distances (z=1 and 7.5 mm) and recorded at 2, 3, 4, and 5 μs gate delays for a fixed gate width time of 0.5 μs. By analyzing figures 26 and 27 it is possible to see that C atoms are produced both in the ablated target and in the air breakdown. When the spectra were recorded near the target surface (z<2.5 mm), the main contribution of C

atoms is due to the target surface. For z>2.5 mm, practically the spectrum is due to air breakdown. At far away distances from the metal mesh target surface, the plasma front arrives later than for close distances. Figure 28 displays several time-resolved emission spectra from LIB (106 J/cm^2) in air monitored at 1, 2.5, 5, and 7.5 mm observed distances and after the laser pulse (t_d<0.5 μs). In this figure, one can see that at short time after the TEA CO_2 laser pulse, the plasma emission consists in an intense continuum that decreases with distance. Figure 29 shows time-resolved emission spectra from laser-induced air plasma (106 J/cm^2) recorded at t_d=3 μs with t_w=0.5 μs monitored at 1, 2.5, 5, 7.5 and 10 mm. In these recording conditions, the most intense plasma is monitored at 5 mm from the mesh target surface.

Figure 30 displays the temporal evolution of the LIBS air plasma (160 J/cm^2) in the spectral region 3725-3860 Å region monitored at 2.5, 3 and 4 μs gate delays for a fixed gate width time of 0.5 μs (z=1 cm) and time-integrated spectrum (t_d=0 and t_w>>30 μs). The inset plot shows the assignment of some ionic lines of N^+, O^+ and O^{2+} and band heads of different molecular bands of $N_2^+(B^2\Sigma_u^+-X^2\Sigma_g^+$; $\Delta v=0$ sequence) [see Fig. 17(g)]. At early times (t_d<1 μs) (not shown), the plasma emission consists in a weak continuum. When the delay increases, some ionic lines of N^+, O^+ and O^{2+} and band heads of the molecular bands of $N_2^+(B^2\Sigma_u^+-X^2\Sigma_g^+)$ enhanced steeply as a consequence of the expansion and heating of the air plasma. At longer times (t_d>3 μs), the ion lines significantly decrease steeply in intensity as a consequence of the expansion and cooling of the plasma plume and its recombination into ground state ions. At t_d>4 μs, N^+ and O^+ ionic lines and N_2^+ rovibrational lines disappear. Figure 31 shows the temporal evolution of the LIBS air plasma (71 J/cm^2) in the spectral region 3830-3960 Å region monitored at 2, 3 and 4 μs gate delays for a fixed gate width time of 0.5 μs (z=1 cm) and time-integrated spectrum (t_d=0 and t_w>>30 μs). This plot also shows the assignment of some ionic lines of N^+, O^+ and N^{2+} and band heads of different molecular bands of $N_2^+(B^2\Sigma_u^+-X^2\Sigma_g^+$; $\Delta v=0$ sequence). At early times (t_d<1 μs) (not shown), the plasma emission consists in a continuum. When the delay increases, some ionic lines of N^+, O^+ and N^{2+} and band heads of the molecular bands of $N_2^+(B^2\Sigma_u^+-X^2\Sigma_g^+)$ enhanced as a

consequence of the air plasma expansion. At longer times (t_d>3 μs), the ion lines significantly decrease steeply in intensity. At t_d>5 μs, N^+, N^{2+} and O^+ ionic lines and N_2^+ rovibrational lines disappear. Figure 32 displays the temporal progress of the LIBS air plasma in the spectral window 4070-4195 Å observed at 2.5, 3 and 4 μs gate delays for a fixed gate width time of 0.5 μs (z=1 cm) and time-integrated spectrum (t_d=0 and t_w>>30 μs). The assignments of some ionic lines of N^+, O^+ and N^{2+} and band heads of different molecular bands of N_2^+($B^2\Sigma_u^+$-$X^2\Sigma_g^+$; Δv=-1 sequence) are indicated. As before, at early times (t_d<1 μs), the plasma emission consists in a weak continuum. When the delay increases, some ionic lines of N^+, O^+ and N^{2+} and band heads of the molecular bands of N_2^+($B^2\Sigma_u^+$-$X^2\Sigma_g^+$) enhanced. At longer times (t_d>3 μs), the ion lines significantly decrease steeply in intensity. At t_d>4 μs, N^+, N^{2+} and O^+ ionic lines and N_2^+ rovibrational lines disappear.

5.3.2 Time of flight, velocity, kinetic energy and electron density

Space-and-time resolved OES measurements could be used to estimate plasma expansion rate and kinetic energy. The temporal evolution of spectral atomic, ionic and molecular line intensities at a constant distance from the target can be used to construct the time-of-flight (TOF) profile. TOF studies of the emission provide fundamental information regarding the time taken for a particular species to evolve after the laser-induced plasma has been formed. Specifically, this technique gives an indication of the velocity of the emitted species. A coarse estimation of the velocity for the different species in the plume can be inferred from the time resolved spectra by plotting the intensities of selected emission lines versus the delay time, and then calculating the velocity by dividing the distance from the target by the time where the emission peaks. This method for determination of plasma velocity should be used with care due to the superposition of both expansion and forward movements of the plasma plume. We assumed a plasma model consisting in two plasmas [74]: primary plasma that acts as initial explosion energy source and emits an intense continuum emission background for a short time just above the surface of the

auxiliary target; secondary plasma expands with time around the primary plasma. The secondary plasma is formed by the excitation from the shock wave and by the emitting of atomic, ionic and molecular species characterized by a low background signal.

Figure 33(a) displays the TOF profiles for the air breakdown experiments induced by CO_2 laser pulses (106 J/cm^2), of continuum radiation, O^+(2433.53 Å), O^+(2455.53 Å), N^+(2461.27 Å), N^+(2478.56 Å), N^+(2522.23 Å) and C(2478.56 Å) lines as a function of the delay time. We notice the appearance of a strong maximum for continuum background for a delay of 1 μs at z=5 mm. When t_d increases, the continuum drops steeply as a consequence of the reduction of electron density and temperature as the plume expands. For O^+ and N^+ ionic species and C atomic, the maxima appear for a delay of 2.5, 3 and 4.5 μs, respectively. The emission intensity of O^+ and N^+ ionic lines decreases more rapidly than the emission intensity of the C lines. The time duration of ionic species was nearly 5 μs, while the time duration of C atomic emission was nearly 20 μs. The experimental TOF distributions $N(t)$ are essentially number density distributions. They are converted to flux distributions dN/dt by employing a correction factor z/t, where z means the flight distance along the plasma expansion and t is the delay time after the laser pulse incidence. It should be mentioned that the estimation of velocity distributions assumes that the emitting species are generated on the assisting metal mesh target. The velocity distributions that are derived from these TOF distributions are display in figure 33(b). At the laser fluence used in this series of experiments (106 J/cm^2) and z=5 mm, TOF distributions present different characteristics. Thus, the velocity distributions of ionic species O^+(2445.54 Å) and N^+(2522.23 Å) are comparatively wider (~3.7 and ~4 km/s (FWHM), respectively) than the velocity distribution of carbon neutral species [~1.2 km/s (FWHM)]. The velocity distributions of O^+, N^+ and C lines species are centred at about 2, 1.7 and 1.1 km/s, respectively. From TOF spectra, the translational kinetic energy can be deduced [$KE=(1/2)m(z/t)^2$] by measuring the time t required to transverse the distance from the target to the detector z. The kinetic energy obtained for some species are plotted in figure 34. We have observed small atomic and ionic average kinetic energies. As we have stated above, for a

better understanding of the physical mechanisms underlying the plasma emission breakdown in air, LIB spectra were obtained by varying both the distance *z* (up to 10 mm) with respect to the auxiliary metal mesh and the laser energy. It is expected, in fact, that these two parameters would affect strongly the dynamic evolution of the plasma and the shock wave induced by the CO_2 laser. Different lines originating from atomic and ionic species of both nitrogen and oxygen were analyzed. O^+ doublet ($2s^22p^2(^1D)3p\ ^2D^0_{3/2,5/2} \rightarrow 2s^22p^2(^3P)3s\ ^2P_{3/2}$) at ~ 2445 Å and N^+ triplet ($2s^22p(^2P^0)4d\ ^3D^0_{1,2,3} \rightarrow 2s^22p(^2P^0)3p\ ^3P_{0,1,2}$) at ~ 2522 Å were chosen as representative of ionized lines. The energies of the lower levels of both multiplets are high (189068.514 for O^+ and 170572.61, 170607.89 and 170666.23 cm^{-1} for N^+) so that the self-absorption effect can be neglected. Figures 35 and 36 show TOF and velocity distributions of multiplet structures of N^+(~2522 Å) and O^+(~2445 Å) at different distances (1, 2.5, 5, 7.5 and 10 mm) as for a laser fluence of 106 J/cm^2 The temporal emission features are affected by the presence of strong continuum at short distances ($z \leq 3$ mm) and at early delay time. But at distances greater than 3 mm, the continuum radiation is considerably reduced and the interference of continuum on the TOF distributions is negligible. The spike observed in TOF and velocity profiles is the prompt signal that is used as a time maker. By the shift of the TOF peaks for each distance it is possible to calculate approximately the mean velocities of LIB along the propagation axis *Z*. The measured peak velocities of multiplet structures of N^+(~2522 Å) and O^+(~2445 Å) monitored at 1, 2.5, 5, 7.5 and 10 mm (for a laser fluence of 106 J/cm^2) are 0.5, 1, 1.7, 2.1 and 3.6 km/s and 0.5, 1, 2, 2.5 and 5 km/s, respectively. The peak velocities of N^+ and O^+ increase with the distance from the target surface. This is due to the initial acceleration of the ablated partials from zero velocity to a maximum velocity. Also we have studied OES of the air plasma by varying the laser energy. We observed that when the laser fluence is increased, the N^+ and O^+ TOF distributions broaden and move towards lower delay times. On the other hand, plasma temperature was determined from the emission line intensities of several N^+ and O^+ ionized lines observed in the laser-induced plasma of air for a delay time of 3 μs and a distance of z=5 mm. The obtained excitation temperatures, in

the case of N^+ and O^+, were 23400 ± 900 K and 26600 ± 1300 K, respectively. For N^+ and O^+ lines, the Doppler line widths vary between 0.08-0.17 Å at 23400 K and 0.11-0.13 Å at 26600 K, respectively.

The N^+ triplet ($2s^2 2p(^2P^0)4d\ ^3D^0_{1,2,3} \rightarrow 2s^2 2p(^2P^0)3p\ ^3P_{0,1,2}$) at ~2522 Å was identified as candidate for electron-density measurements. By substituting the Stark line widths at different time delays in Eqn. (3.12) and the corresponding value of Stark broadening W (0.372 Å from Griem [41] at plasma temperature of 23400 K), we obtain the electron density. Figure 37 gives the time evolution of electron density and its first derivative with respect to time by setting the gate width of the intensifier at 0.5 μs. These values have been obtained by Stark broadening of the N^+ TOF curves at z = 5 mm and for a laser fluence of 106 J/cm^2. The initial electron density at 0.1 μs is approximately 1.3×10^{16} cm^{-3}. Afterwards, the density increases and reaches a maximum (1.7×10^{17} cm^{-3}) at ~0.8 μs, and then decrease as the time is further increased. At shorter delay times (<0.1 μs), the line to continuum ratio is small and the density measurement is sensitive to errors in setting the true continuum level. For times >0.1 μs, the line to continuum ratio is within the reasonable limits and the values of electron density shown in figure 37 should be reliable. After 6 μs, the electron density is about 2.7×10^{16} cm^{-3}. For a long time >6 μs, subsequent decreased N^+ emission intensities result in poor signal-to-noise ratios, and there exits a limitation in the spectral resolution. The decrease of n_e is mainly due to recombination between electrons and ions in the plasma. These processes correspond to the so-called radiative recombination and three-body recombination processes in which a third body may be either a heavy particle or an electron. The electron number density n_e (cm^{-3}) in the laser induced plasma is governed by the kinetic balance equation 2.10. By considering the discussion reported in section 2.3, the equilibrium condition can be established at 0.8 μs (dynamical equilibrium) and t>2 μs (stationary equilibrium). For $t \leq 0.8$ μs the ionization prevails while for 0.8 μs<t<2 μs the three-body recombination dominates. In the case of TEA-CO_2 laser at a laser fluence of 106 J/cm^2 and z=5 mm, the recombination rate constant estimated is approximately 5×10^{-28} cm^6 s^{-1} (Eq. 2.11). The

recombination time can be determined by the value of the rate constant of the recombination process as $t_{rec}=1/(n_e^2.k_{rec})$ obtaining $t_{rec}\approx$0.4-3 μs.

Optical emission accompanying TEA-CO_2 nanosecond LIB in air is very long lived (~20 μs) relative to the average radiative lifetimes of the excited levels that give rise to the observed emission lines. All of the emission lines of N, N^+, N^{2+}, O, O^+ and O^{2+} expected in the 2000-10000 Å wavelength range are observed, illustrating that the excited species giving rise to the optical emission are produced by non-specific mechanism during the TEA CO_2 LIB process. However, a direct excitation-de-excitation mechanism cannot explain the observed emission spectra. Electron impact ionization would explain the emission intensity variation with the time for N, N^+, N^{2+}, O, O^+ and O^{2+} species. On the other hand, the formation of the excited molecular species would happen in the gas phase by collisions between atomic or ionic species present in the plume at times far away from the plasma ignition. The emission process at this plasma stage is divided into two different process associated, respectively with the shock formation and the plasma cooling. During the former, the atoms, molecules and ions gushing out from the laser focal region are adiabatically compressed against the surrounding gas. During the latter stage the temperature of the plasma and consequently the emission intensities of atomic lines and molecular bands decrease gradually.

6. Conclusion

This article reviews some fundamentals of LIBS and some experimental studies developed in our laboratory on N_2, O_2 and air gases using a high-power IR CO_2 pulsed laser. In this experimental study we used several laser wavelengths (λ=9.621 and 10.591 μm) and laser intensity ranging from 0.87 to 6.31 GW cm^{-2}. The spectra of the generated plasmas are dominated by emission of strong atomic, ionic species and molecular bands. For the assignment of molecular bands a comparison with conventional emission sources was made. Excitation, vibrational and rotational temperatures, ionization degree and electron number density for some species were estimated by using different spectroscopic methods. The characteristics of the spectral emission intensities from

different species have been investigated as functions of the gas pressure and laser irradiance. Optical breakdown threshold intensities in different gases have been measured experimentally. The physical processes leading to laser-induced breakdown of the gases have been analyzed. Plasma characteristics in LIBS of air were examined in detail on the emission lines of N^+, O^+ and C by means of time-resolved OES technique. The results show a faster decay of continuum and ionic spectral species than of neutral atomic and molecular ones. The velocity and kinetic energy distributions for different species were obtained from TOF measurements. Excitation temperature and electron density in the laser-induced plasma were estimated from the analysis of spectral data at various times from the laser pulse incidence. Temporal evolution of electron density has been used for the estimation of the three-body recombination rate constant.

ACKNOWLEDGMENTS

We gratefully acknowledge the support received in part by the DGICYT (Spain) Projects: MEC: CTQ2007-60177/BQU and MEC: CTQ2008-05393/BQU for this research.

TABLE AND TABLE LEGENDS

Table 1.- List of the most intense observed molecular bands in the LIB in nitrogen, corresponding electronic transition and wavelength in Å (air) for the major band heads.

Molecule	Name system	Observed band system	Major band heads (Å) (v', v")
N_2^+	Janin-d'Incan	$D^2\Pi_g - A^2\Pi_u$	2343 (0, 0); 2398 (1, 1); 2456 (2, 2); 2516 (3,3); 2579 (4, 4); 2645 (5, 5); 2714 (6, 6)
N_2^+	First negative	$B^2\Sigma_u^+ - X^2\Sigma_g^+$	2861.7 (11, 6); 3033.0 (11, 7); 3065.1 (15, 10); 3076.4 (4, 1); 3078.2 (3, 0); 3291.6 (5, 3); 3293.4 (4, 2); 3298.7 (3, 1); 3308.0 (2, 0); 3319.9 (8, 6); 3349.6 (18, 13); 3381.5 (10, 8); 3419.6 (14, 11); 3447.3 (23, 16); 3460.8 (17, 13); 3493.4 (12, 10); 3532.3 (5, 3); 3538.3 (4, 3); 3548.9 (3, 2); 3563.9 (2, 1); 3582.1 (1, 0); 3588.6 (16, 13); 3612.4 (10, 9); 3806.8 (5, 5); 3818.1 (4, 4); 3835.4 (3, 3); 3857.9 (2, 2); 3884.3 (1, 1); 3914.4 (0, 0); 4110.9 (6, 7); 4121.3 (5,6); 4140.5 (4, 5); 4199.1 (2, 3); 4236.5 (1, 2); 4278.1 (0, 1); 4459.3 (7, 9); 4466.6 (6, 8); 4490.3 (5, 7); 4515.9 (4, 6); 4554.1 (3, 5); 4599.7 (2, 4); 4651.8 (1, 3); 4709.2 (0, 2); 4864.4 (7, 10); 4881.7 (6, 9); 4913.2 (5, 8); 4957.9 (4, 7); 5012.7 (3, 6); 5076.6 (2, 5); 5148.8 (1, 4); 5228.3 (0,3); 5485.5 (4, 8); 5564.1 (3, 7); 5653.1 (2, 6); 5754.4 (1, 5); 5864.7 (0, 4)
N_2	Second positive	$C^3\Pi_u - B^3\Pi_g$	2953.2 (4, 2); 2962.0 (3, 1); 2976.8 (2, 0); 3116.7 (3, 2); 3136.0 (2, 1); 3159.3 (1, 0); 3268.1 (4, 4); 3285.3 (3, 3); 3311.9 (2, 2); 3338.9 (1, 1); 3371.3 (0, 0); 3500.5 (2, 3); 3536.7 (1, 2); 3576.9 (0, 1); 3641.7 (4, 6); 3671.9 (3, 5); 3710.5 (2, 4); 3755.4 (1, 3); 3804.9 (0, 2); 3857.9 (4, 7); 3894.6 (3, 6); 3943.0 (2, 5); 3998.4 (1, 4); 4059.4 (0, 3); 4094.8 (4, 8); 4141.8 (3, 7); 4200.5 (2, 6); 4269.7 (1, 5); 4343.6 (0, 4); 4355.0 (4, 9); 4416.7 (3, 8); 4490.2 (2, 7); 4574.3 (1, 6); 4667.3 (0, 5); 4723.5 (3, 9); 4814.7 (2, 8); 4916.8 (1, 7); 5031.5 (0, 6); 5066.0 (3, 10); 5179.3 (2, 9); 5309.3 (1, 8)

TABLE 2.- Laser parameters for the TEA CO_2 LIB experiments of oxygen.

Laser λ(μm)	Energy E_W (mJ)	Power P_W (MW)	Intensity I_W (GW cm^{-2})	Fluence Φ_W (J cm^{-2})	Photon Flux, F_{ph} (ph. cm^{-2} s^{-1})	Electric Field F_E (MV cm^{-1})
9.621	2685	42.1	5.36	342	2.60×10^{29}	1.50
9.621	2256	35.4	4.50	287	2.18×10^{29}	1.37
9.621	1732	27.1	3.46	220	1.67×10^{29}	1.20
9.621	1209	19.0	2.41	154	1.17×10^{29}	1.01
9.621	503	7.88	1.00	64.0	4.86×10^{28}	0.65
10.591	3161	49.5	6.31	402	3.36×10^{29}	1.63
10.591	2145	33.6	4.28	273	2.28×10^{29}	1.34
10.591	1481	23.2	2.96	189	1.58×10^{29}	1.11
10.591	968	15.2	1.93	123	1.03×10^{29}	0.90
10.591	624	9.78	1.25	79.5	6.64×10^{28}	0.72
10.591	436	6.83	0.87	55.5	4.64×10^{28}	0.60

REFERENCES

[1] Maker, P. D.; Terhune, R. W.; Savage, C. M. *Proc. 3rd Int. Conf. Quantum Electronics*; (Paris: Dunod) 1963, Vol. **2** p 1559.

[2] Raizer, Y. P. *Breakdown and heating of gases under the influence of a laser beam*; Soviet Physics: Uspekhi. Vol. **8**, Nº 5, 1966.

[3] Raizer, Y. P. *Laser-Induced discharge phenomena*; Consultants Bureau: New York. 1977.

[4] Bebb, H. B.; Gold, A. *Multiphoton Ionization of Hydrogen and Rare Gas Atoms; Physics of Quantum Electronics;* ed P L Kelly *et al* McGraw-Hill: New York. 1966.

[5] De Michelis, C. *IEEE J. Quantum Electron.* 1969, **5,** 188-202.

[6] Morgan, C. G. *Rep. Prog. Phys.* 1975, **38**, 621-665.

[7] Bekefi, G. *Principles of Laser Plasma*; Wiley: New York. 1976.

[8] Lyman, J. L.; Quigley, G. P.; Judd; O. P. *Multiple-Photon Excitation and Dissociation of Polyatomic Molecules*; Ed. Cantrell, C. D. Springer: Berlin. 1980.

[9] Rosen, D. I.; Weyl, G. *J. Phys. D: Appl. Phys.* 1978, **20,** 1264-1276.

[10] Gamal, Y. E. E-D. *J. Phys D: Appl. Phys.* 1988, **21**, 1117-1120.

[11] Smith, D. C. *Laser induced gas breakdown and plasma interaction* 38th Aerospace Sciences Meeting and Exhibit. Reno: Nevada. 2000.

[12] Yueh, F.-Y.; Singh, J. P.; Zhang, H. *Encyclopedia of Analytical Chemistry (Laser-lnduced Breakdown Spectroscopy, Elemental Analysis)*; ed R A Meyers. Wiley: Chichester. 2000.

[13] Cremers, D. A.; Radziemski, L. J. *Handbook of Laser-lnduced Breakdown Spectroscopy*; Wiley: Chichester. 2006.

[14] Miziolek, A. W.; Palleschi, V.; Schechter, I. *Laser-Induced Breakdown Spectroscopy*; Cambridge University Press: Cambridge. 2006.

[15] Singh, J. P.; Thakur, S. N. *Laser-Induced Breakdown Spectroscopy*; Elsevier: New York. 2007.

[16] Yong-Ill, L., *Laser Induced Breakdown Spectrometry*; Nova Science Publishers: New York 2000.

[17] Marpaung, A. M.; Kurniawan, H.; Tjia, M. O.; Kagawa, K. *J. Phys. D: Appl. Phys.* 2001, **34**, 758-771.

[18] Camacho, J. J.; Poyato, J. M. L.; Diaz, L.; Santos, M. *J. Phys. B: At. Mol. Opt. Phys.* 2007, **40**, 4573-4590.

[19] Camacho, J. J.; Poyato, J. M. L.; Diaz, L.; Santos, M. *J. Appl. Phys.* 2007, **102**, 103302-10.

[20] Camacho, J. J.; Santos, M.; Diaz, L.; Poyato, J. M. L. *J. Phys. D: Appl. Phys.* 2008, **41**, 215206-13pp.

[21] Camacho, J. J.; Santos, M.; Diaz, L.; Juan, L. J.; Poyato, J. M. L. 2009 (Submitted for publication)

[22] MacDonald, A. D. *Microwave Breakdown in Gases*; Wiley: New York. 1966.

[23] Raizer, Y. P. *Gas Discharge Physics;* Springer: Berlin, Heidelberg. 1991.

[24] Kopiczynski, T. L.; Bogdan, M.; Kalin, A. W.; Schotwau, H. J.; Kneubuhl, F. H. *Appl. Phys. B: Photophys. Laser Chem.* 1992, **54**, 526-530.

[25] Tozer, B. A. *Phys. Rev.* 1965, **137,** 1665-1667.

[26] Radziemski, L. J.; Cremers, D. A.; *Laser-induced plasma and applications*; New York: Dekker. 1989.

[27] Gurevich, A.; Pitaevskii, L. *Sov. Phys. JETP*, 1962, **19**, 870-871.

[28] Capitelli, M.; Capitelli, F.; Eletskii, A. *Spectrochim. Acta B*, 2000, **55**, 559-574.

[29] Capitelli, M.; Casavola, A.; Colonna, G.; Giacomo, A. D. *Spectrochim. Acta B*, 2004, **59**, 271-289.

[30] Chan, C. H.; Moody, C. D.; McKnight, W. B. *J. Appl. Phys.* 1973, **44**, 1179-1188.

[31] Smith, D. S.; Haught, A. F. *Phys. Rev. Lett.* 1966, **16**, 1085-1088.

[32] Young, M.; Hercher, M. *J. Appl. Phys.* 1967, **38**, 4393-4400.

[33] Barchukov, A. I.; Bunkin, F. V.; Konov, V. I.; Lubin, A. A. *Sov. Phys. JETP*, 1974, **39**, 469-477.

[34] Hermann, J.; Boulmer-Leborgne, C.; Mihailescu, I. N.; Dubreuil, B. *J. Appl. Phys.* 1993, **73**, 1091-1099.

[35] Offenberger, A. A.; Burnett, N. H. *J. Appl. Phys.* 1972, **43**, 4977-4980.

[36] Donaldson, T. P.; Balmer, J. E.; Zimmermann, J. A. *J. Phys. D: Appl. Phys.* 1980, **13**, 1221-1233.

[37] Meyerand, R. G.; Haught, A. F. *Phys. Rev. Lett.* 1964, **13**, 7-9.

[38] Spitzer, L. *Physics of Fully Ionised Gases*; John Wiley: New York. 1962.

[39] Hermann, J.; Boulmer-Leborgne C.;, Dubreuil, B.; Mihailescu, I. N. *J. Appl. Phys.* 1993, **74**, 3071-3079.

[40] Ready, J. F. *Effect of high power laser radiation*; Academic Press: New York. 1971.

[41] Griem, H. R. *Principles of plasma spectroscopy*; University Press: Cambridge. 1997.

[42] Griem, H. R. *Phys. Rev.* 1962, **128**, 515-523.

[43] Huddlestone, R. H.; Leonard, S. L. *Plasma Diagnostic Techniques*; Academic Press: New York. 1965.

[44] Hutchinson, I. H. *Principles of plasma diagnostic*; University Press: Cambridge. 2002.

[45]NIST Atomic Spectra Database online at http://physics.nist.gov/PhysRefData/ASD/index.html

[46] Herzberg, G. *Spectra of diatomic molecules*; Van Nostrand: New York. 1950.

[47] Steinfeld, J. I. *An introduction to modern molecular spectroscopy*; MIT Press: London. 1986.

[48] Bernath, P. F. *Spectra of atoms and molecules*; Oxford University Press: New York. 1995.

[49] Camacho, J. J.; Pardo, A.; Martin, E.; Poyato, J. M. L. *J. Phys. B: At. Mol. Opt. Phys.* 2006, **39**, 2665-2679.

[50] Kovacs, I. *Rotational Structure in the Spectra of Diatomic Molecules*; Hilger: London. 1969.

[51] Drogoff, L. B.; Margotb, J.; Chakera, M.; Sabsabi, M.; Barthelemy, O.; Johnstona, T. W.; Lavillea, S.; Vidala, F.; Kaenela, V. Y. *Spectrochim. Acta Part B*, 2001, **56**, 987-1002.

[52] Lofthus, A.; Krupenie, P. H. *J. Phys. Chem. Ref. Data*; 1977, **6**, 113-307.

[53] Herzberg, G. *Ergeb. Exakten Naturwiss.* 1931, **10**, 207-284.

[54] Pannetier, G.; Marsigny, G. L.; Guenebaut, H. C. *R. Acad. Sci. Paris*, 1961, **252**, 1753-1755.

[55] Tanaka, Y.; Jursa, A. S. *J. Opt. Soc. Amer.* 1961, **51,** 1239-1245.

[56] Meinel, A. B. *Astrophys. J.* 1950, **112,** 562-563.

[57] Ledbetter, J. W. Jr. *J. Mol. Spectrosc.* 1972, **42** 100-111.

[58] Huber, K. P.; Herzberg, G. *Molecular spectra an Molecular structure. IV. Constants of diatomic molecules*; Van Nostrand Reinhold: New York. 1979.

[59] Laher, R. R.; Gilmore, F. R. *J. Phys. Chem. Ref. Data*, 1991, **20,** 685-712.

[60] Gilmore, F. R. *J. Quant. Spectrosc. Radiat. Transfer*, 1965, **5,** 369-389.

[61] Aguilera, J. A.; Aragon, C. *Spectrochim. Acta B*, 2004, **59**, 1861-1876.

[62] Martin, W. C.; Zalubas, R. *J. Phys. Chem. Ref. Data*, 1983, **12,** 323-379.

[63] Sreckovic, A.; Dimitrijevic, M. S.; Djenize, S. *Astron. and Astroph.* 2001, **371,** 354-359.

[64] Alcock, A. J.; Kato, K.; Richardson, M. C. *Opt. Comm.*1968, **6**, 342-343.

[65] Haught, A. F.; Meyerand, R. G.; Smith, D. C. *Physics of Quantum Electronics*; Ed. Kelley, P. L.; Lax, B.; Tannenwald, P. E. MacGraw-Hill: New York. 1966. p. 509.

[66] De Michelis, C. *Opt. Comm.* 1970, **2**, 255-256.

[67] Ireland, C. L. M.; Morgan, C. G. *J. Phys. D: Appl. Phys.*1973, **6**, 720-729.

[68] Aaron, J. M.; Ireland, C. L. M. Morgan, C. G. *J. Phys. D: Appl. Phys.*1974, **7**, 1907-1917.

[69] Phuoc, T. X.; White, C. M. *Opt. Comm.* 2000, **181**, 353-359.

[70] Tomlinson, R. G.; Damon, E. K.; Buscher, H. T. *Physics of Quantum Electronics*; Ed. Kelley, P. L.; Lax, B.; Tannenwald, P. E. MacGraw-Hill: New York. 1966. p. 520.

[71] N. Kawahara, J.L. Beduneau, T. Nakayama, E. Tomita, Y. Ikeda: *Appl. Phys. B* 2007, **86**, 605-614.

[72] Zhuzhukalo, E. V.; Kolomiiskii, A. N.; Nastoyashchii, A. F.; Plyashkevich, L. N. *J. Quantum Electron.* 1981, **11**, 670-671.

[73] Marcus, S.; Lowder, J. E.; Mooney, D. L. *J. Appl. Phys.* 1976, **47**, 2966-2968.

[74] Kagawa, K.; Yokoi, S. *Spectrochim.. Acta B* 1982, **37,** 789-795.

Figures and figure captions

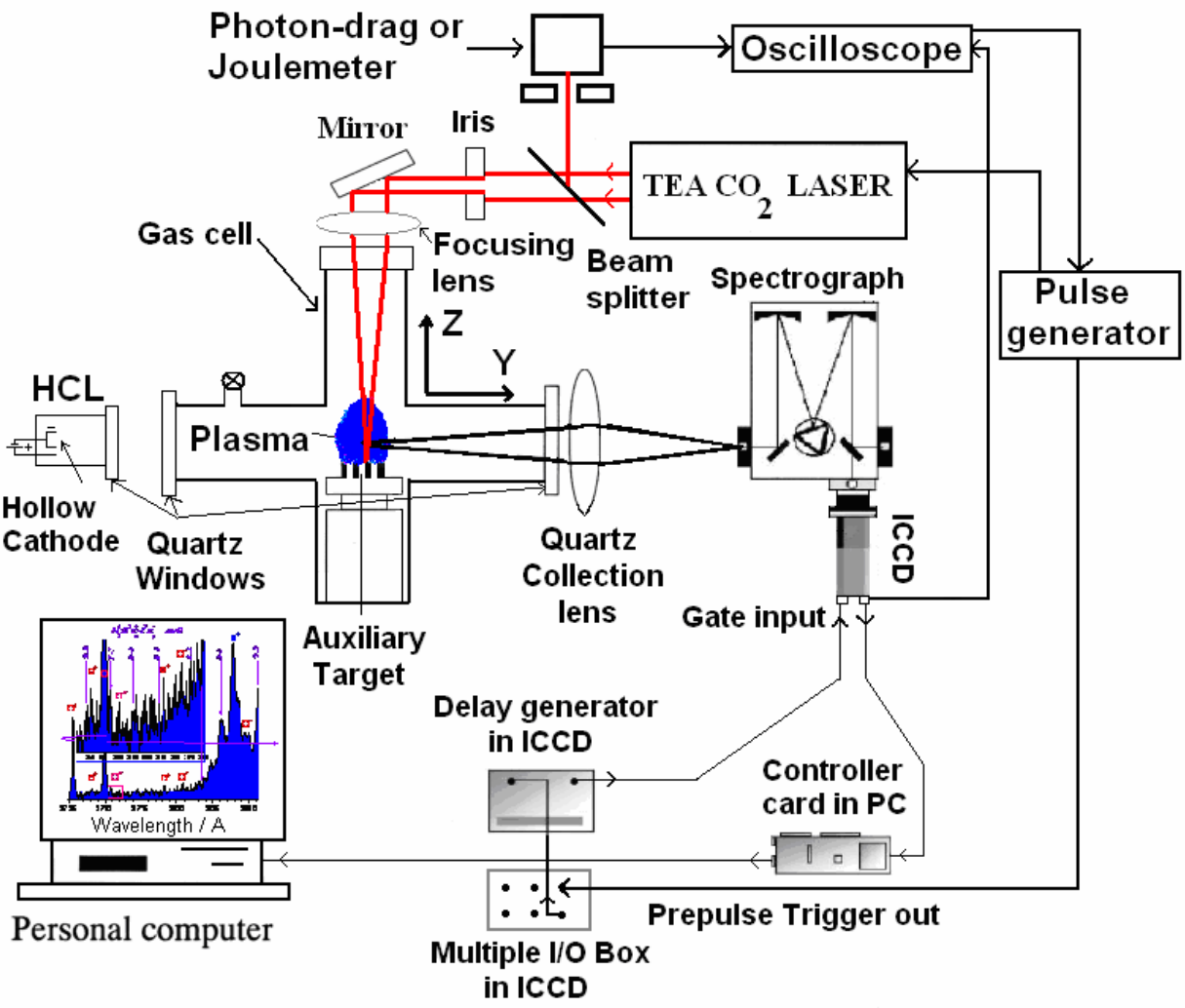

FIG. 1. Schematic diagram of the experimental set-up used for time-resolved TEA-CO_2 pulsed laser gas breakdown diagnostics.

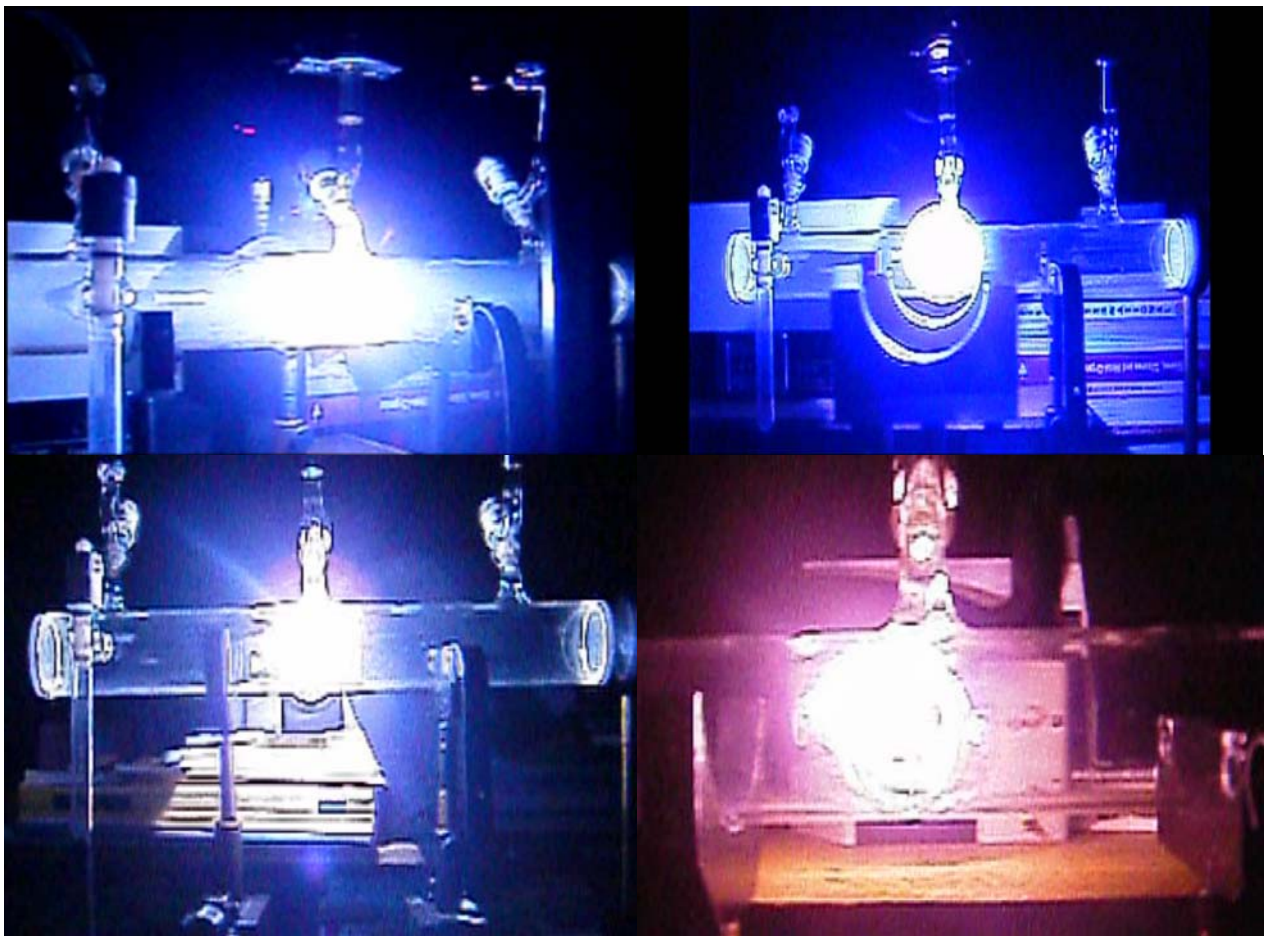

Figure 2. Four images of the LIB of nitrogen at atmospheric pressure (λ=9.621 μm and power density of 4.5 GW×cm^{-2}), oxygen at 49.0 kPa (λ=10.591 μm and power density of 1.93 GW×cm^{-2}), air at atmospheric pressure (λ=9.621 μm and intensity of 5.86 GW×cm^{-2}) and He at atmospheric pressure (λ=10.591 μm and power density of 6.31 GW×cm^{-2}) at different times of the experiment induced by a TEA-CO_2 laser pulse. Laser beam direction is from right to left.

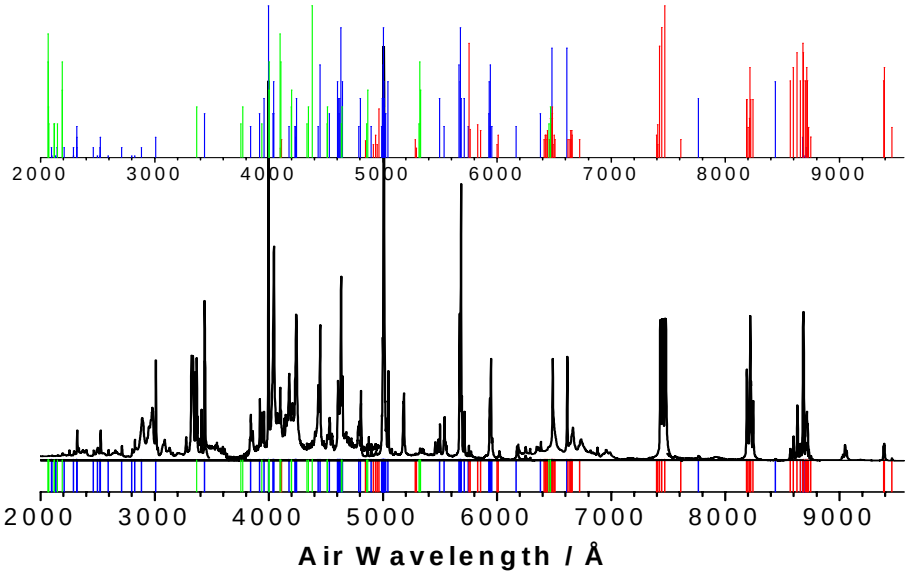

Figure 3. An overview of the LIB emission spectrum of nitrogen at a pressure of 1.2×10^5 Pa, excited by the 9P(28) line at 1039.36 cm^{-1} of the TEA CO_2 laser, compared with atomic lines of N (red), N^+ (blue) and N^{2+}(green).

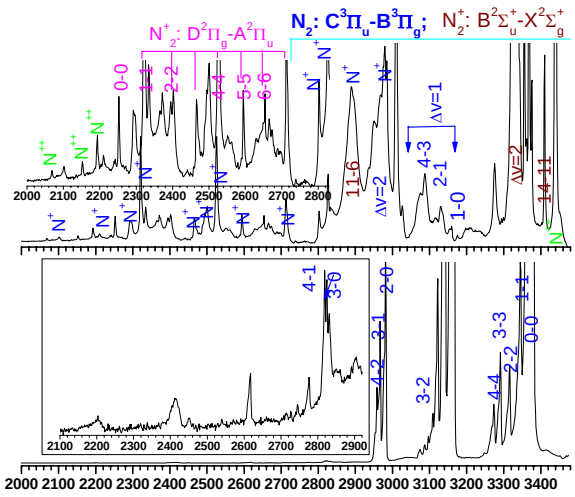
N2+: D2Πg-A2Πu
N2: C3Πu-B3Πg;
N2+: B2Σu+-X2Σg+
Δv=1
Δv=2
2000 2100 2200 2300 2400 2500 2600 2700 2800 2900 3000 3100 3200 3300 3400
Air Wavelength / Å

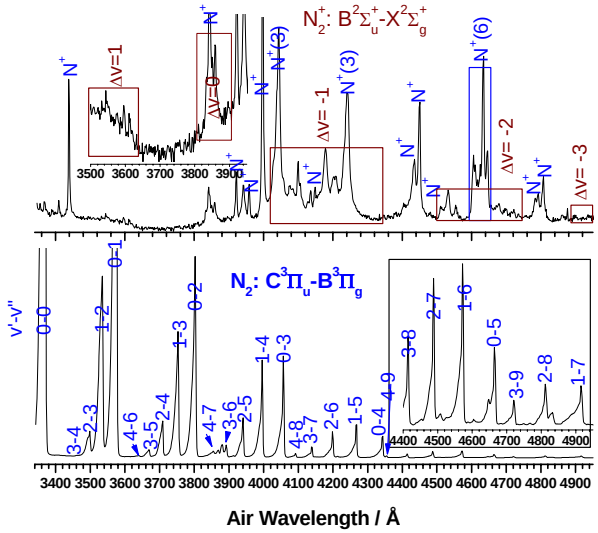
N2+: B2Σu+-X2Σg+
Δv=1
Δv=0
Δv= -1
Δv= -2
Δv= -3
N2: C3Πu-B3Πg
v'-v"
3400 3500 3600 3700 3800 3900 4000 4100 4200 4300 4400 4500 4600 4700 4800 4900
Air Wavelength / Å

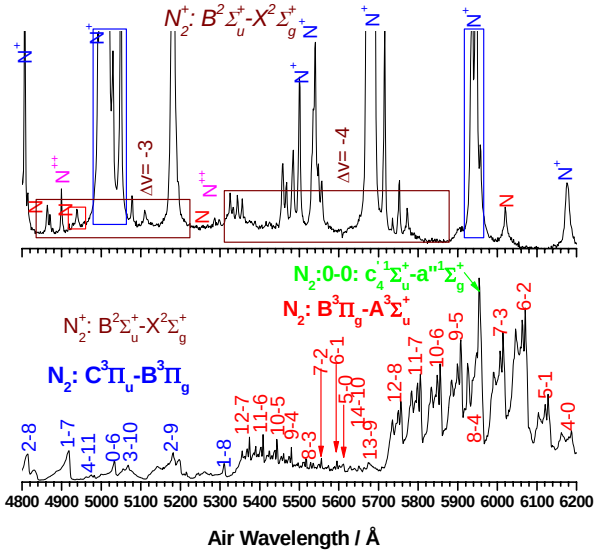
N2+: B2Σu+-X2Σg+
Δv= -3
Δv= -4
N2:0-0: c14Σu+-a"1Σg+
N2: B3Πg-A3Σu+
N2+: B2Σu+-X2Σg+
N2: C3Πu-B3Πg
4800 4900 5000 5100 5200 5300 5400 5500 5600 5700 5800 5900 6000 6100 6200
Air Wavelength / Å

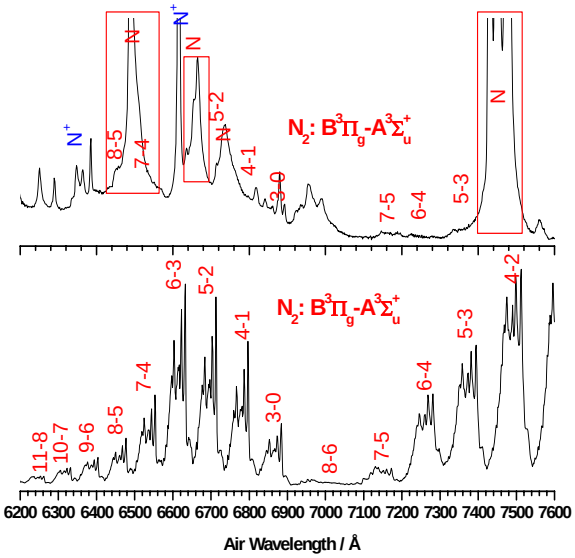
N2: B3Πg-A3Σu+
N2: B3Πg-A3Σu+
6200 6300 6400 6500 6600 6700 6800 6900 7000 7100 7200 7300 7400 7500 7600
Air Wavelength / Å

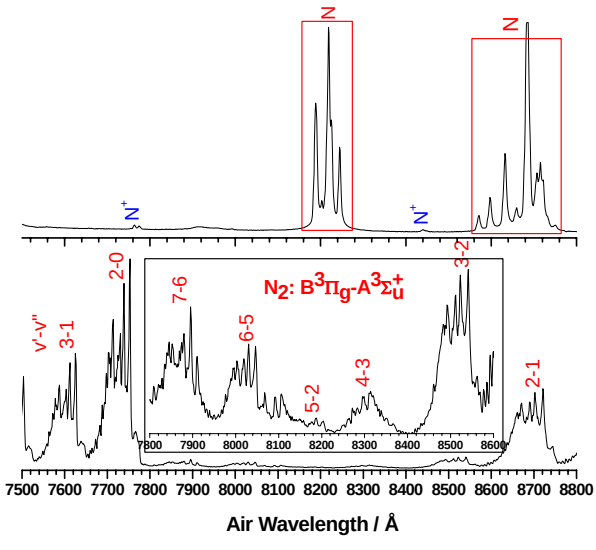
N2: B3Πg-A3Σu+
v'-v"
7500 7600 7700 7800 7900 8000 8100 8200 8300 8400 8500 8600 8700 8800
Air Wavelength / Å

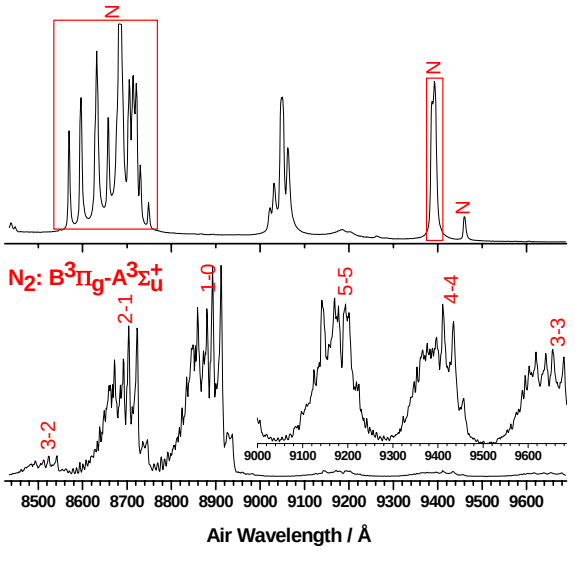
N2: B3Πg-A3Σu+
8500 8600 8700 8800 8900 9000 9100 9200 9300 9400 9500 9600
Air Wavelength / Å

Figure 4. An overview of the low-resolution emission spectra observed in the 2000-9690 Å region. Upper panel: LIDB in nitrogen at a pressure of 1.2×10^5 Pa, excited by the 9P(28) line at 1039.36 cm^{-1} of the CO_2 laser; Lower panel: dc electric glow discharge spectrum of nitrogen at low pressure.

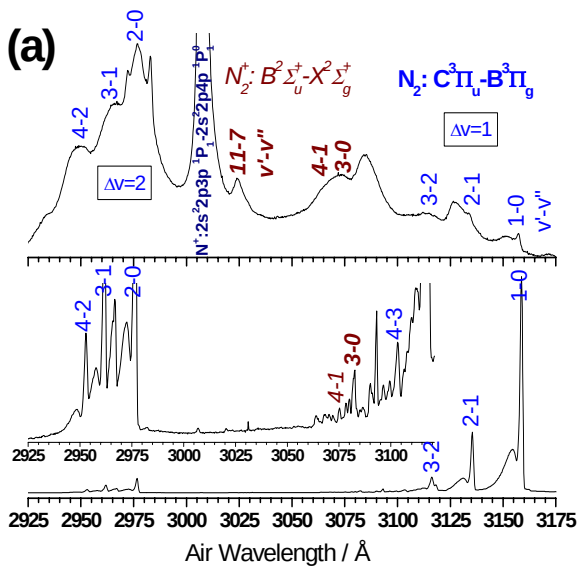
(a)
N_2^+: $B^2\Sigma_u^+$-$X^2\Sigma_g^+$
N_2: $C^3\Pi_u$-$B^3\Pi_g$
Δv=2
Δv=1
Air Wavelength / Å

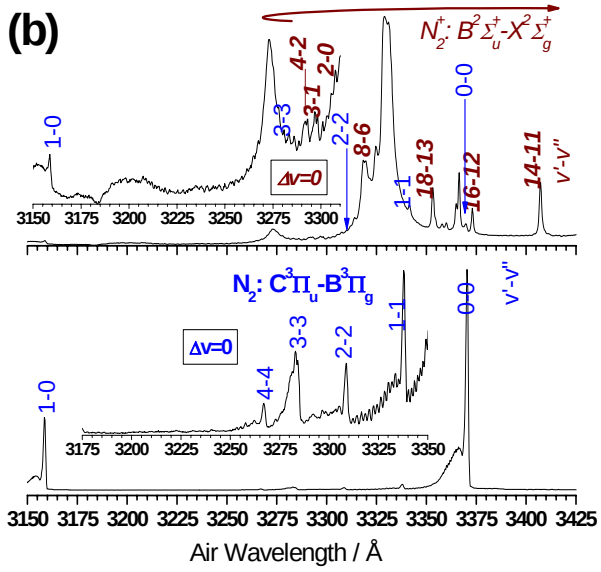
(b)
N_2^+: $B^2\Sigma_u^+$-$X^2\Sigma_g^+$
N_2: $C^3\Pi_u$-$B^3\Pi_g$
Δv=0
Air Wavelength / Å

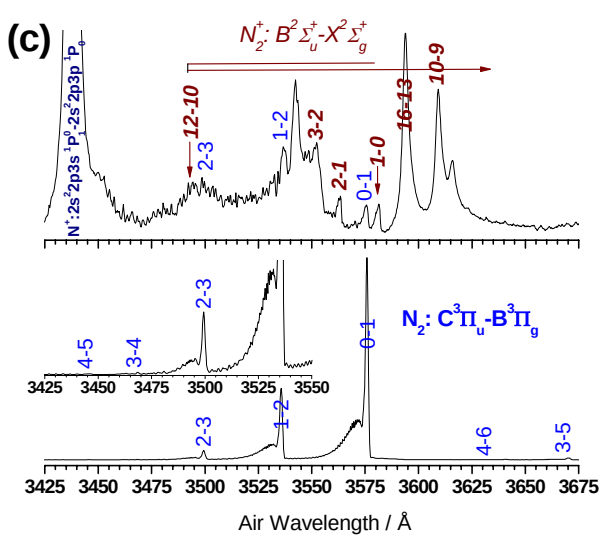
(c)
N_2^+: $B^2\Sigma_u^+$-$X^2\Sigma_g^+$
N_2: $C^3\Pi_u$-$B^3\Pi_g$
Air Wavelength / Å

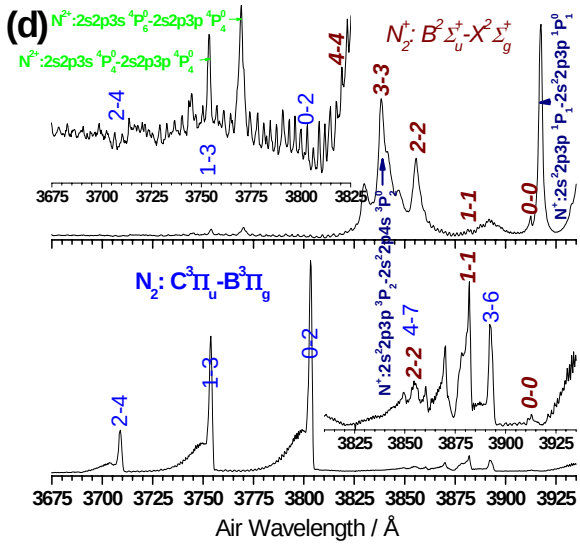
(d)
N_2^+: $B^2\Sigma_u^+$-$X^2\Sigma_g^+$
N_2: $C^3\Pi_u$-$B^3\Pi_g$
Air Wavelength / Å

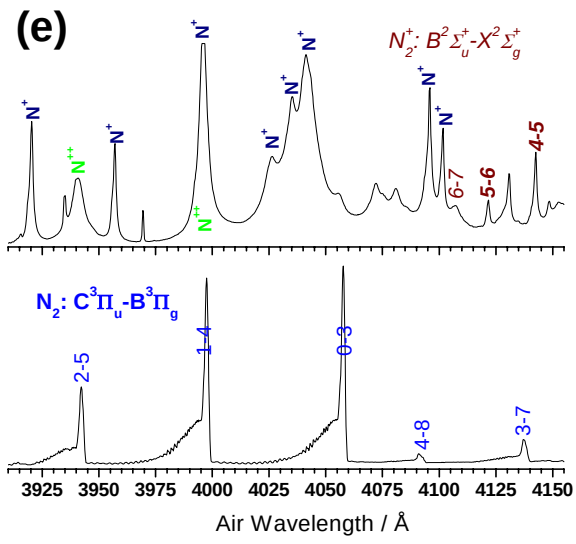
(e)
N_2^+: $B^2\Sigma_u^+$-$X^2\Sigma_g^+$
N_2: $C^3\Pi_u$-$B^3\Pi_g$
Air Wavelength / Å

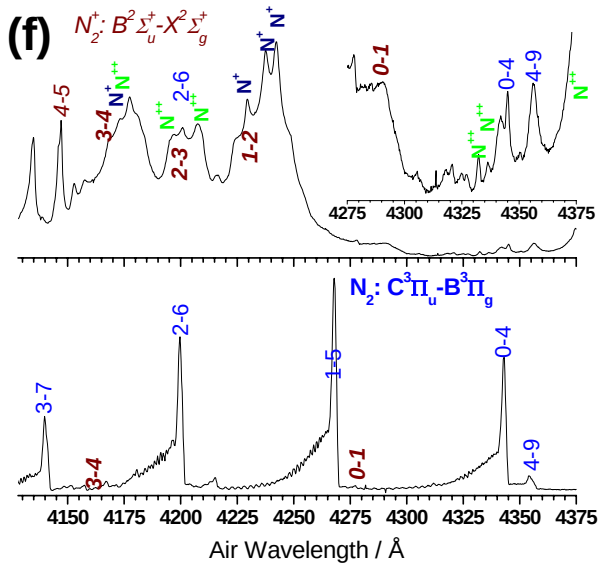
(f)
N_2^+: $B^2\Sigma_u^+$-$X^2\Sigma_g^+$
N_2: $C^3\Pi_u$-$B^3\Pi_g$
Air Wavelength / Å

Figure 5 (a)-(f). Comparison between high-voltage dc electric discharge (lower panels) and LIDB (upper panels) emission spectra for nitrogen in several spectral regions.

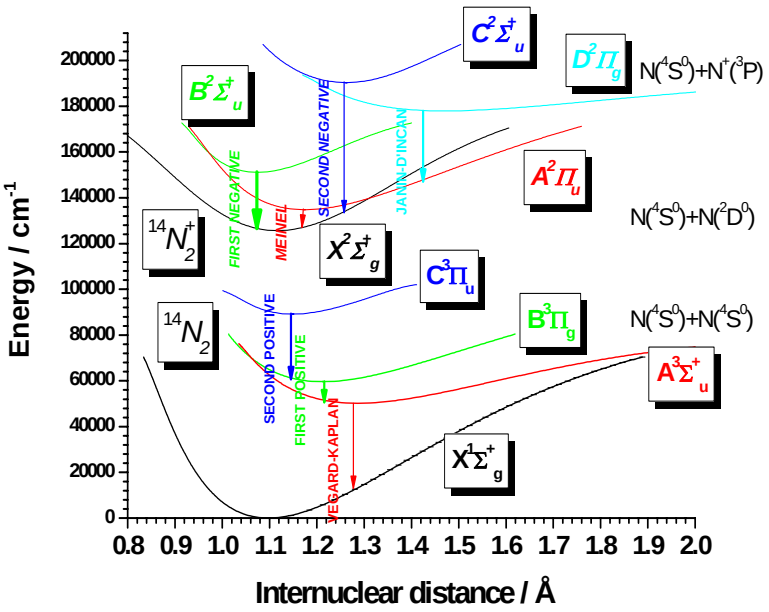

Figure 6. RKR potential energy curves for some bound electronic states of N_2 and N_2^+.

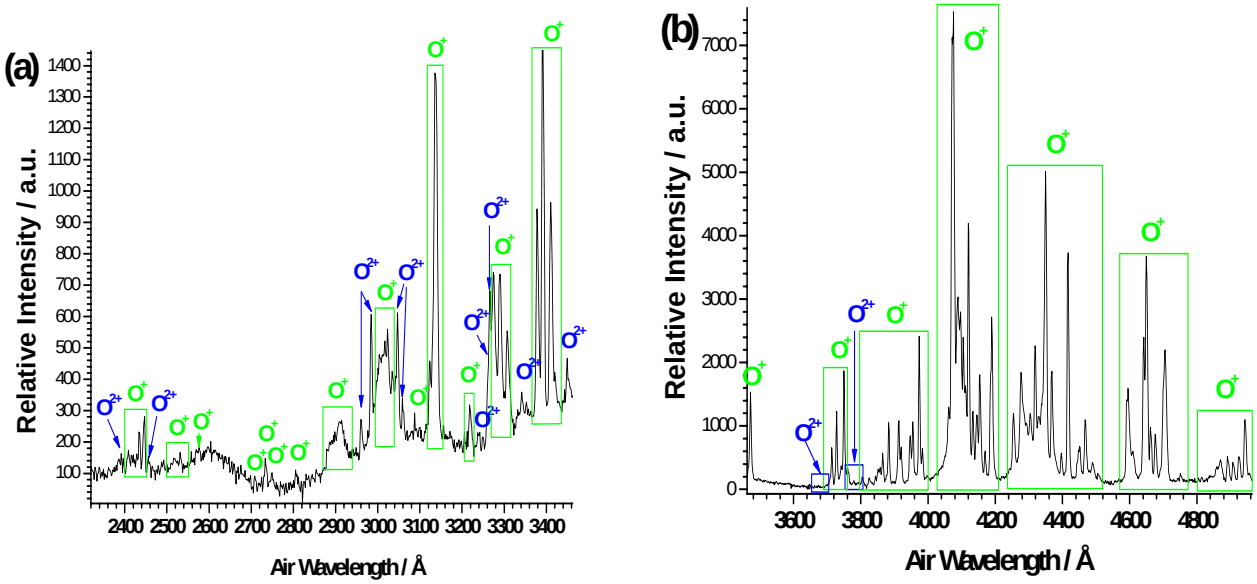

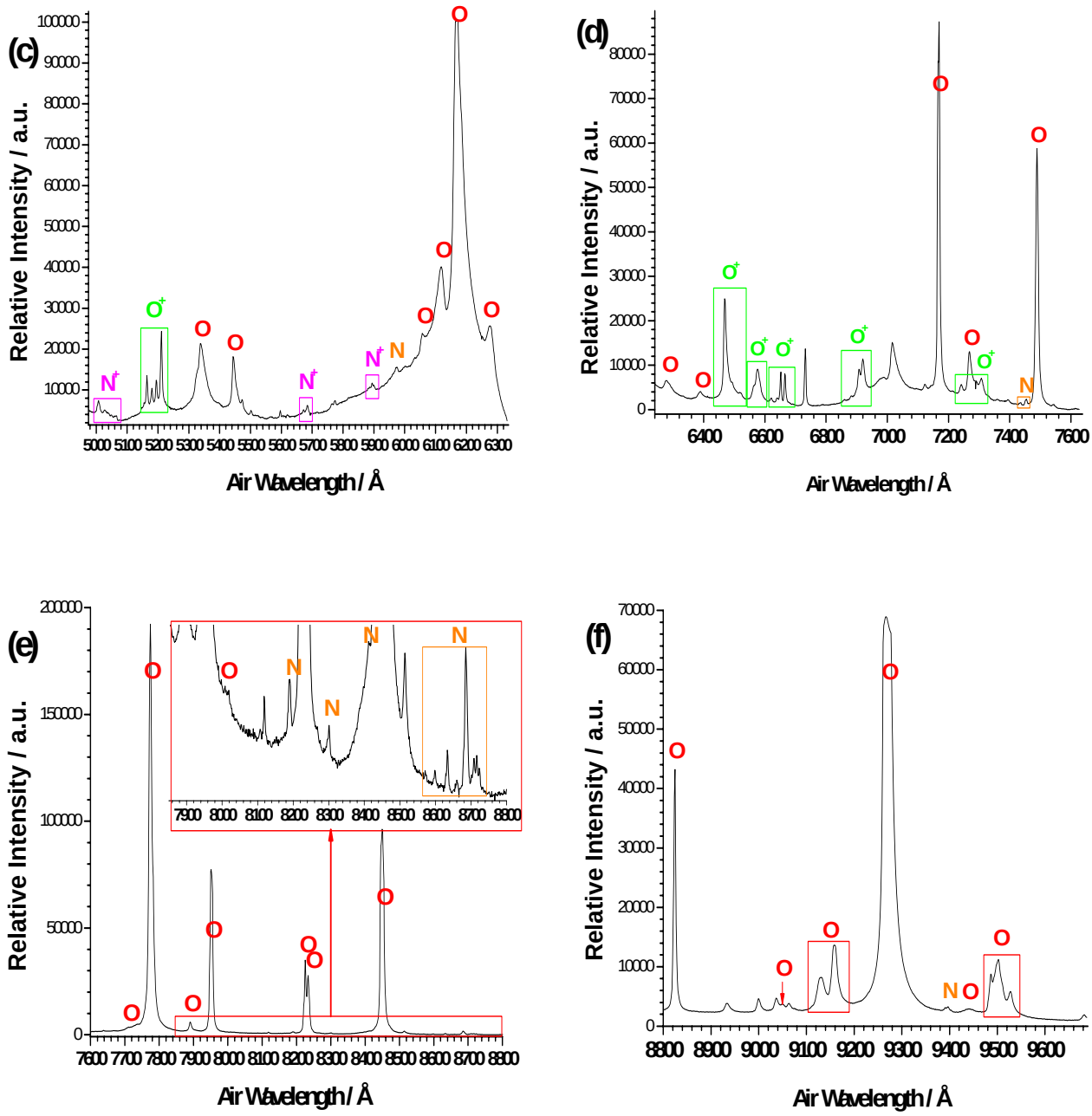

Fig. 7(a-f). Low-resolution LIB emission spectrum observed in the 2320-9690 Å region in oxygen at a pressure of 53.2 kPa, excited by the 10P(20) line of the TEA-CO_2 laser at 10.591 μm and a power density of 0.87 GW×cm^{-2}, and assignment of the atomic lines of O, O^+, O^{2+}, N and N^+.

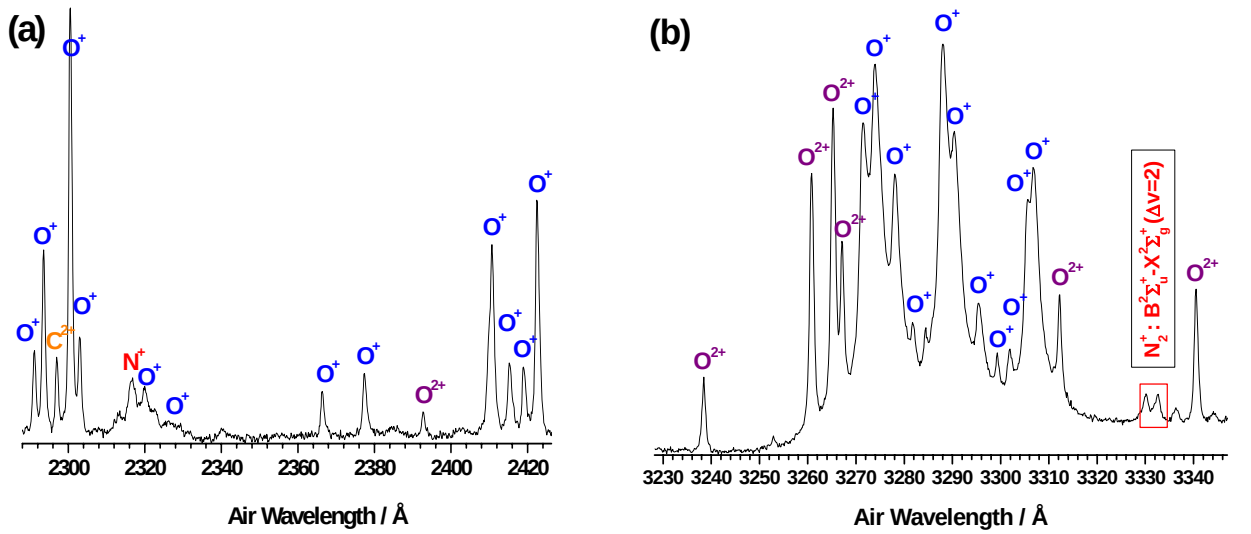
(a)
(b)
(c)
(d)
(e)
(f)
Air Wavelength / Å
Air Wavelength / Å
Air Wavelength / Å
Air Wavelength / Å
Air Wavelength / Å
Air Wavelength / Å
N_2^+: $B^2\Sigma_u^+$-$X^2\Sigma_g^+$ (Δv=2)

Figure 8 (a-f). High-resolution LIB emission spectrum observed in several spectral regions in oxygen at a pressure of 48.8 kPa, excited by the CO_2 laser at 10P(20) line (10.591 μm) with a power density of 4.28 GW×cm^{-2}, and assignment of some atomic lines of O^+, O^{2+}, and N^+.

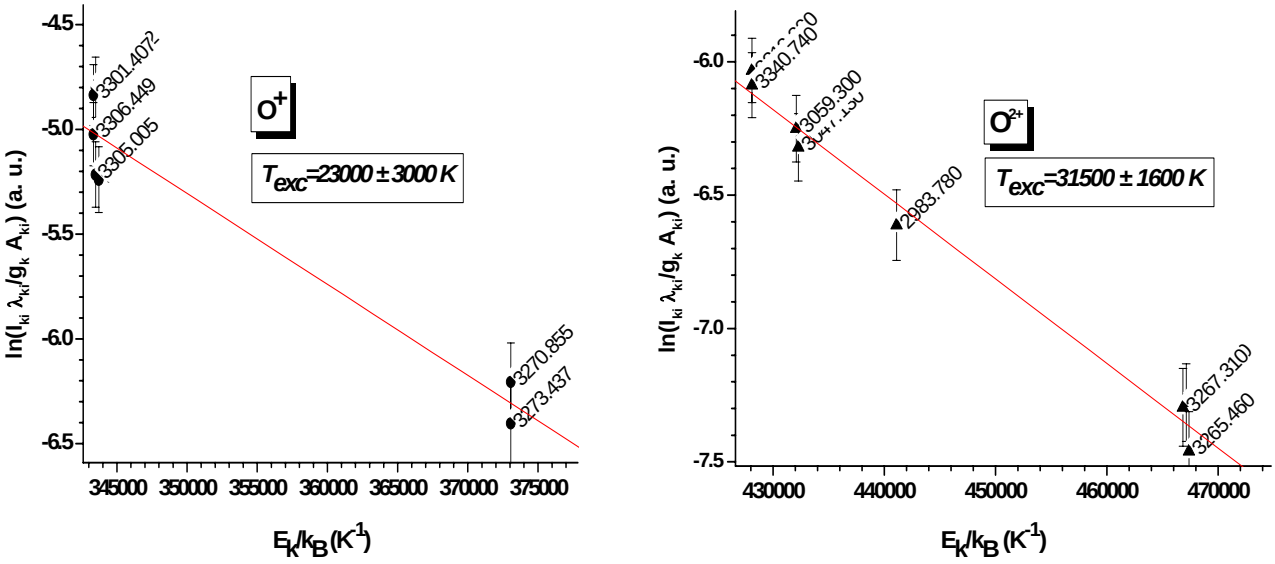

Figure 9. Linear Boltzmann plots for several O^+ and O^{2+} transition lines used to calculate plasma temperature, T_{exc}. Plots also show linear fit to the data.

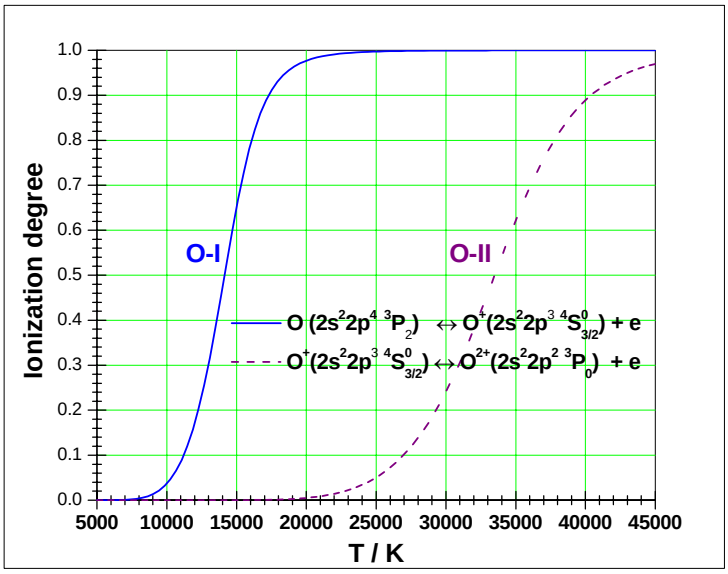

Figure 10. Temperature dependence of the ionization degree $N_i/(N_0+N_i)$ of atomic oxygen O and oxygen singly ionized O^+ at a constant pressure of 53.2 kPa.

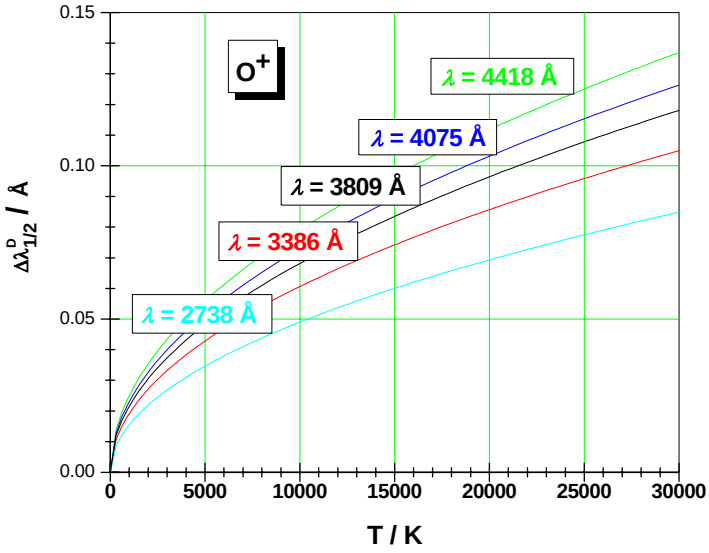

Figure 11. Doppler line widhs for some lines of O^+.

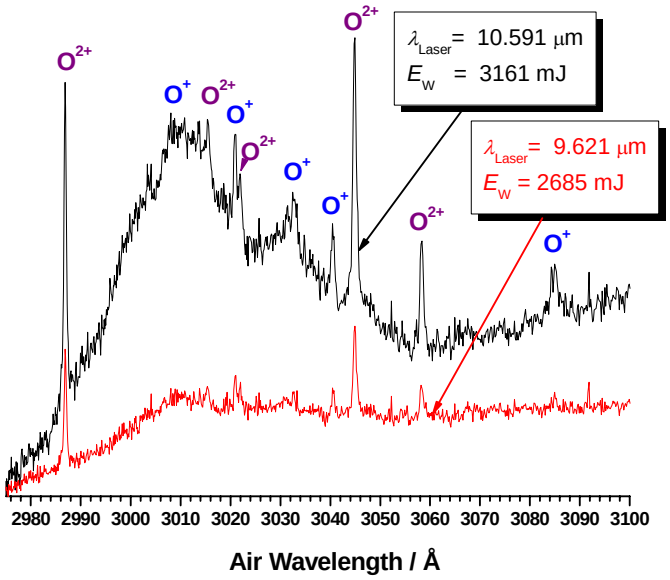

Figure 12. High-resolution LIB emission spectra in oxygen at a pressure of 48.8 kPa, excited by two TEA-CO_2 laser wavelengths at 10.591 μm (E_W=3161 mJ) and 9.621 μm (E_W=2685 mJ).

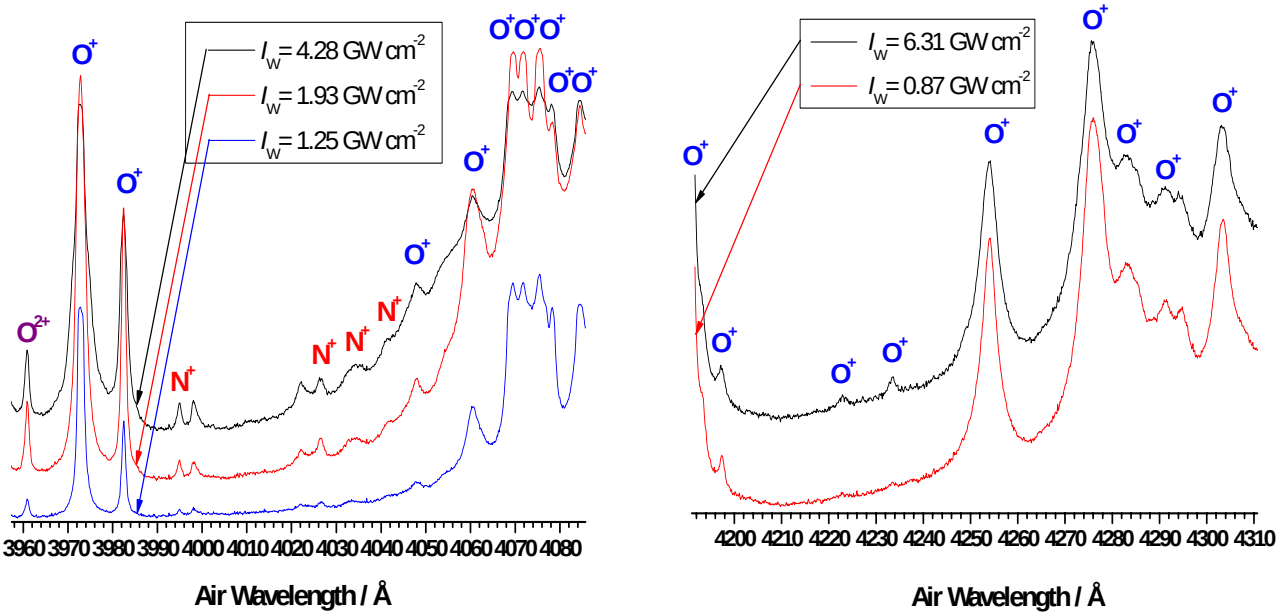

Figure 13 (a-b). High-resolution LIB in oxygen (at a pressure of 48.8 kPa) emission spectra observed in the (a) 3957-4085 Å and (b) 4195-4310 Å regions, excited by two TEA-CO_2 laser wavelengths at 10.591 µm as a function of the laser power density.

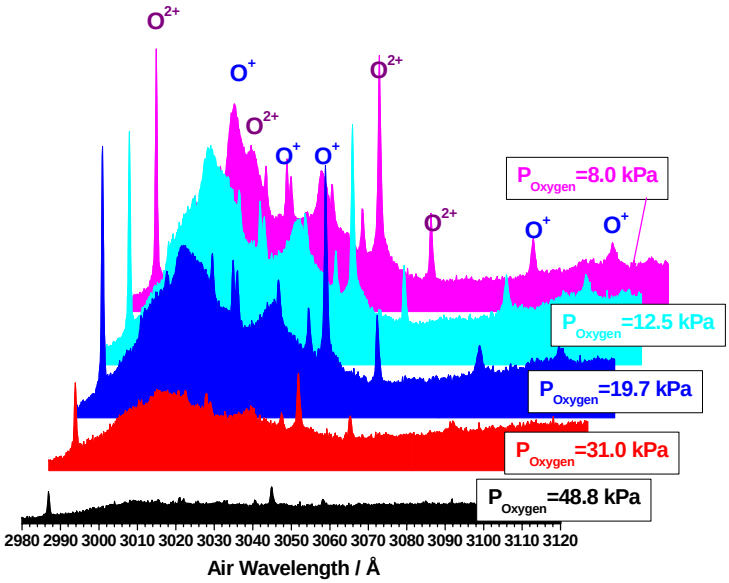

Figure 14. High-resolution LIB emission spectra at various oxygen pressures, excited by the TEA-CO_2 laser (10.591 µm) at a power density of 6.31 GW cm^{-2}.

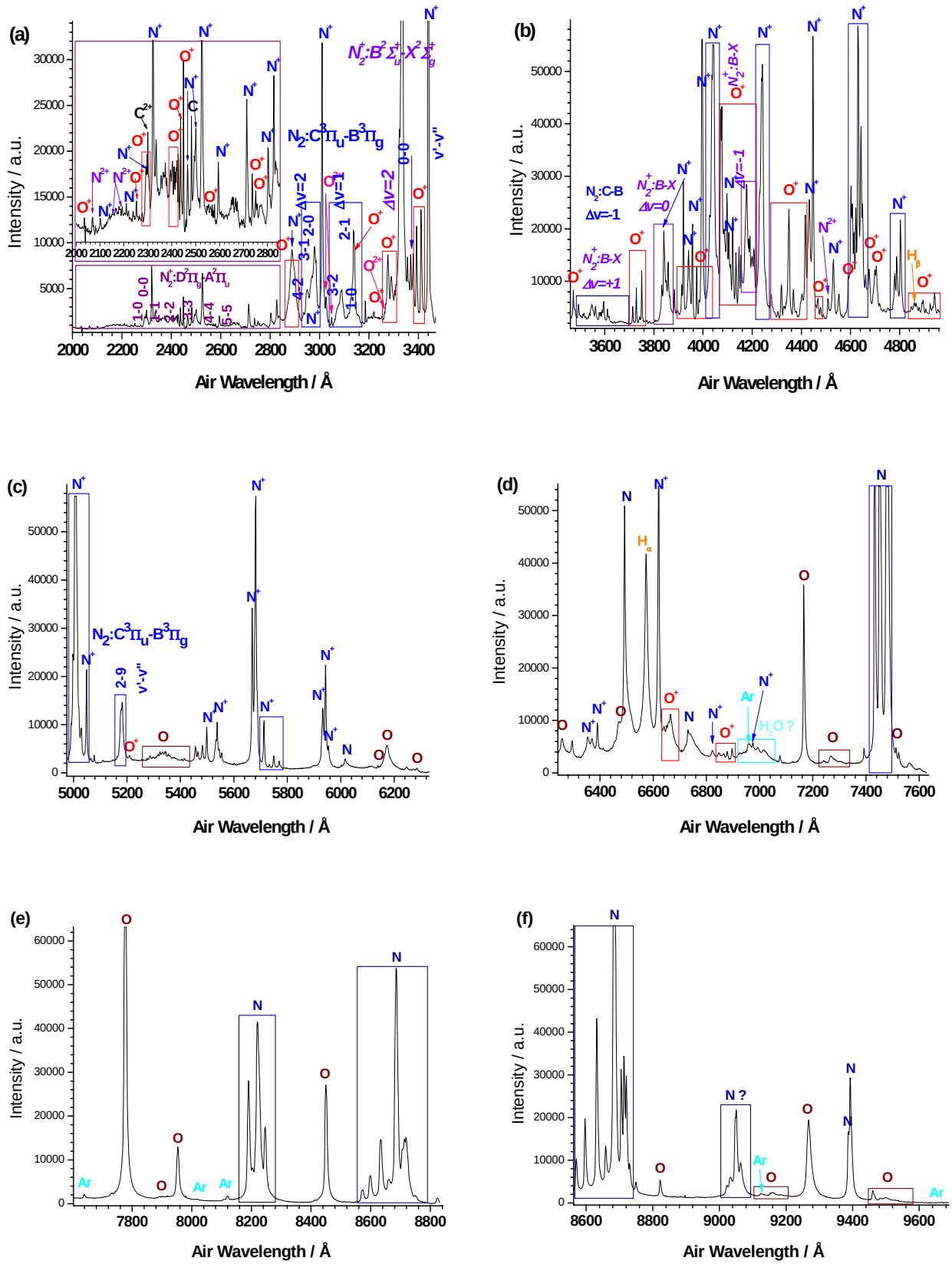

Fig. 15 (a-f) Low-resolution LIB emission spectrum observed in the 2000-9690 Å region in ambient air at atmospheric pressure, excited by the TEA-CO_2 laser at 10.591 μm and a power density of 2.2 GW×cm^{-2}, and assignment of the atomic lines of N, O, C, C^+, H, Ar, N^+, O^+, N^{2+}, O^{2+}, C^{2+} and molecular bands of $N_2^+(B^2\Sigma_u^+-X^2\Sigma_g^+)$ and $N_2(C^3\Pi_u-B^3\Pi_g)$.

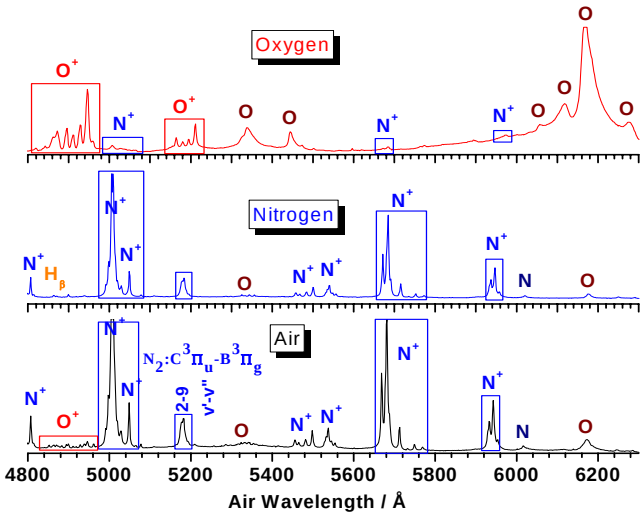

Fig. 16 Low-resolution LIB emission spectra in air, nitrogen and oxygen, excited by the TEA-CO_2 laser at 10.591 μm and a power density of ~1 GW×cm^{-2}, and assignment of the atomic lines of N, O, H, N^+, O^+ and 2-9 molecular band of $N_2(C^3\Pi_u$-$B^3\Pi_g)$.

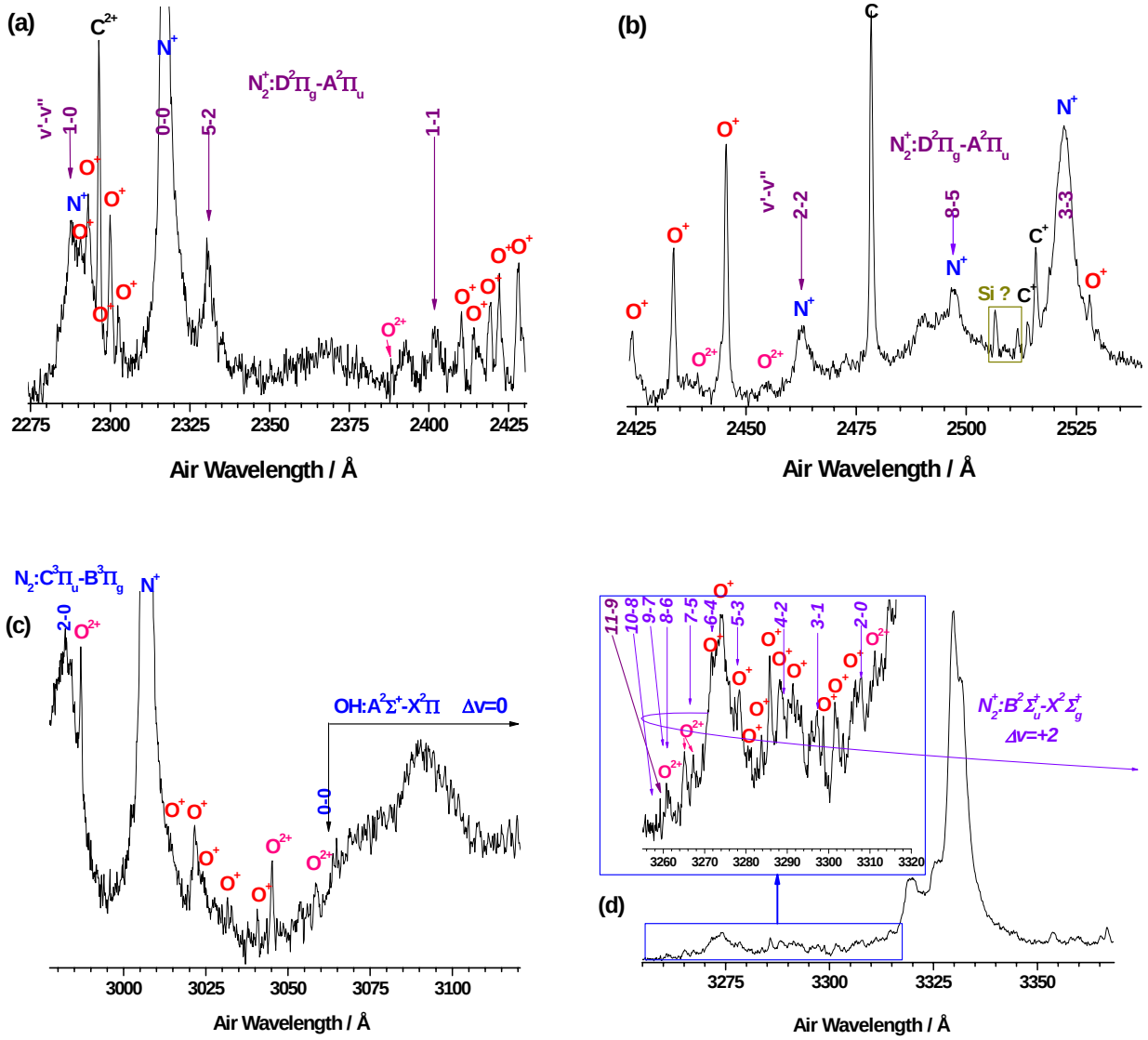

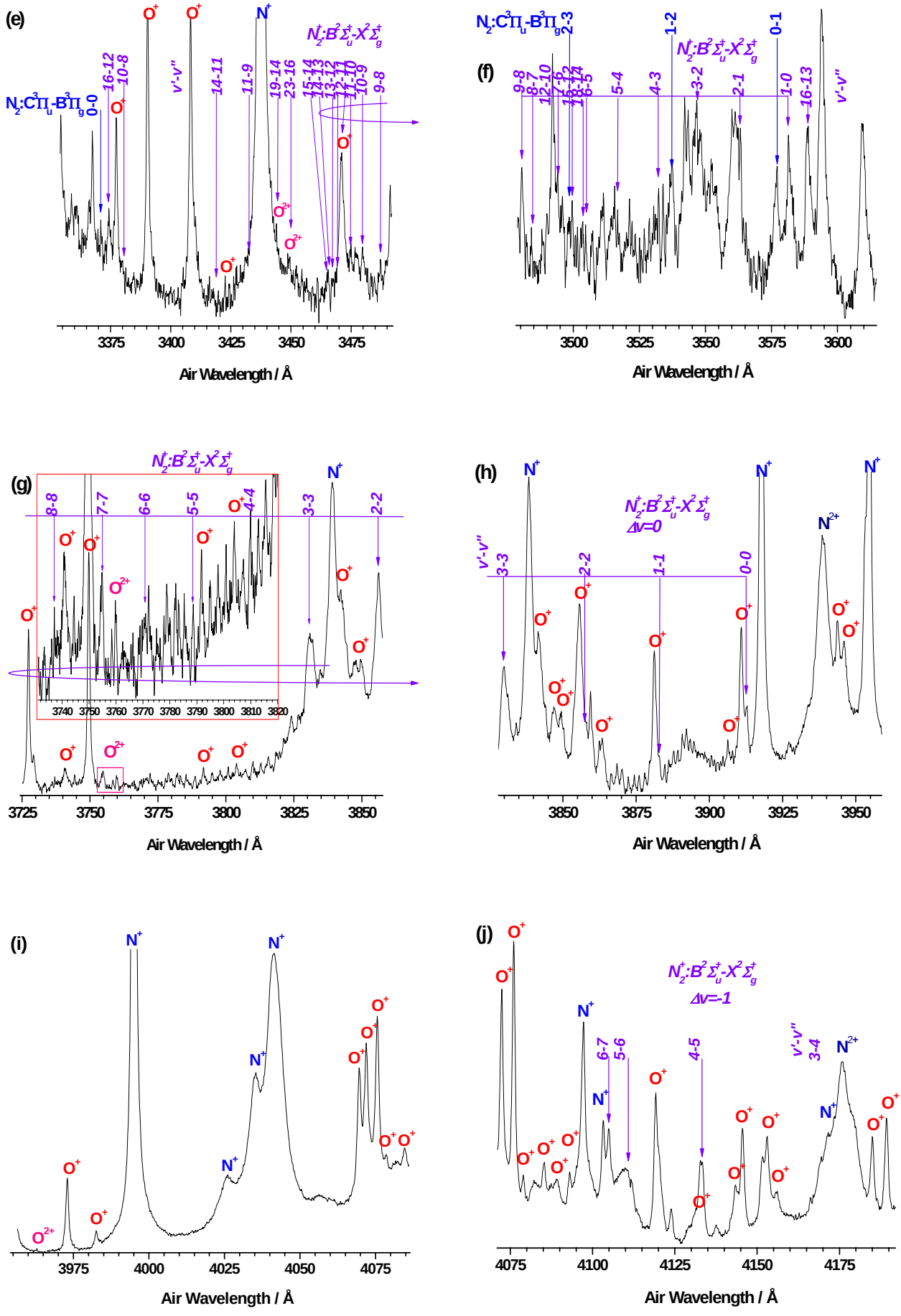
(e)
$N_2^+:B^2\Sigma_u^+-X^2\Sigma_g^+$
$N_2:C^3\Pi_u-B^3\Pi_g$ 0-0
v'-v''
16-12
10-8
14-11
11-9
19-14
23-16
15-14
14-13
13-12
12-11
11-10
10-9
9-8
3375 3400 3425 3450 3475
Air Wavelength / Å
(f)
$N_2:C^3\Pi_u-B^3\Pi_g$ 2-3
1-2
0-1
$N_2^+:B^2\Sigma_u^+-X^2\Sigma_g^+$
9-8
8-7
12-10
11-9
10-8
6-5
5-4
4-3
3-2
2-1
1-0
16-13
v'-v''
3500 3525 3550 3575 3600
Air Wavelength / Å
(g)
$N_2^+:B^2\Sigma_u^+-X^2\Sigma_g^+$
8-8
7-7
6-6
5-5
4-4
3-3
2-2
3740 3750 3760 3770 3780 3790 3800 3810 3820
3725 3750 3775 3800 3825 3850
Air Wavelength / Å
(h)
$N_2^+:B^2\Sigma_u^+-X^2\Sigma_g^+$
$\Delta v=0$
v'-v''
3-3
2-2
1-1
0-0
3850 3875 3900 3925 3950
Air Wavelength / Å
(i)
3975 4000 4025 4050 4075
Air Wavelength / Å
(j)
$N_2^+:B^2\Sigma_u^+-X^2\Sigma_g^+$
$\Delta v=-1$
6-7
5-6
4-5
v'-v''
3-4
4075 4100 4125 4150 4175
Air Wavelength / Å

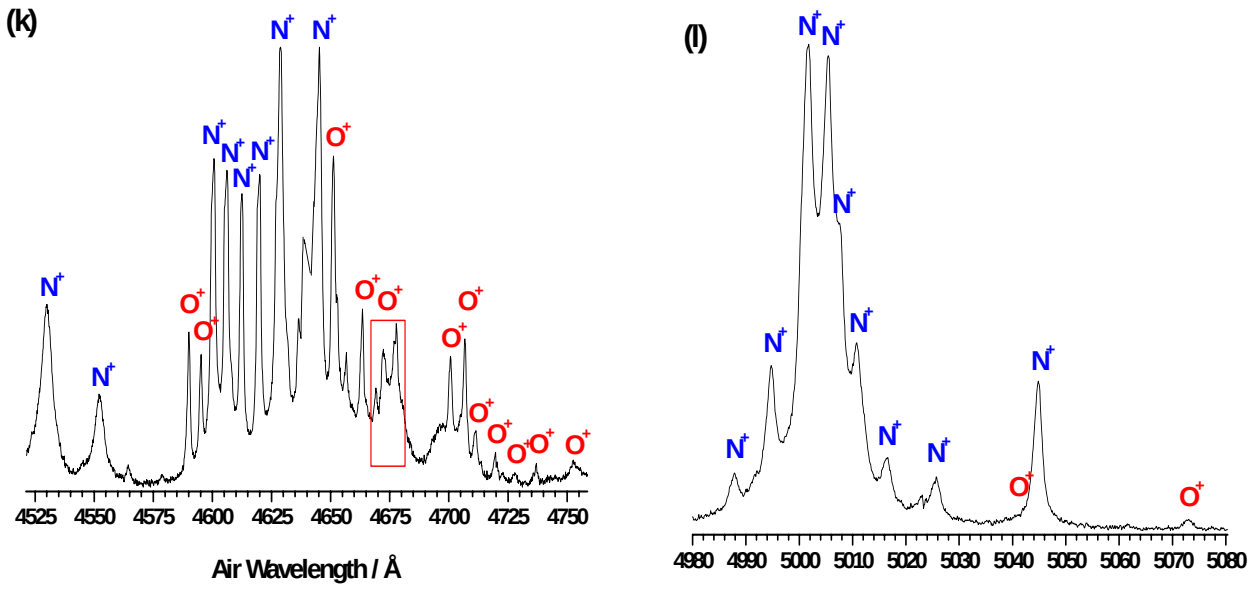

Fig. 16 (a-l) High-resolution LIB emission spectrum observed in several spectral regions in ambient air at atmospheric pressure, excited by the CO_2 laser at 9.621 μm with a power density of 5.36 GW×cm^{-2}, and assignment of some atomic lines of N^+, O^+, N^{2+}, O^{2+}, and band heads of the molecular bands of $N_2^+(B^2\Sigma_u^+\text{-}X^2\Sigma_g^+)$, $N_2(C^3\Pi_u\text{-}B^3\Pi_g)$, $N_2^+(D^2\Pi_g\text{-}A^2\Pi_u)$ and $OH(A^2\Sigma^+\text{-}X^2\Pi)$.

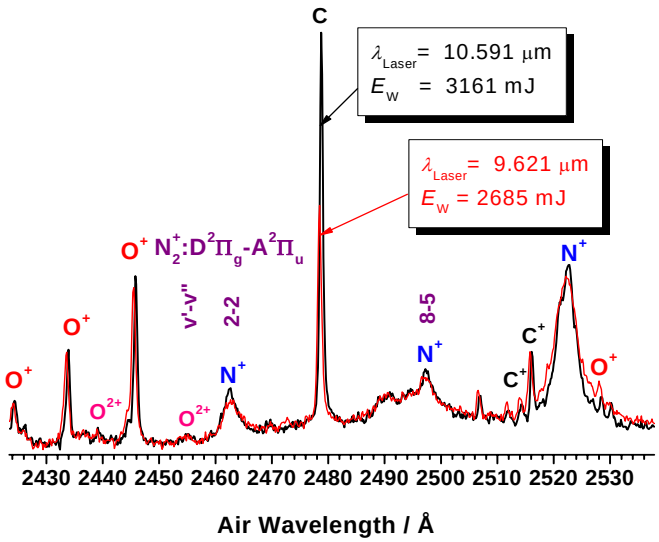

Fig. 17 High-resolution LIB emission spectra in air at atmospheric pressure, excited by two TEA-CO_2 laser wavelengths at 10.591 μm (I_W=6.31 GW/cm^2) and 9.621 μm (I_W=5.36 GW/cm^2).

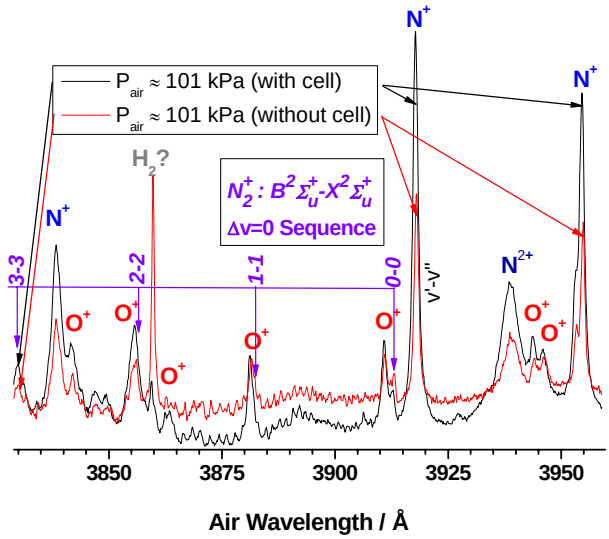

Fig. 18 High-resolution LIB emission spectra in air at atmospheric pressure, excited by the TEA-CO_2 laser line at 9.621 μm (I_W=5.36 GW/cm^2) recorded with cell and without cell.

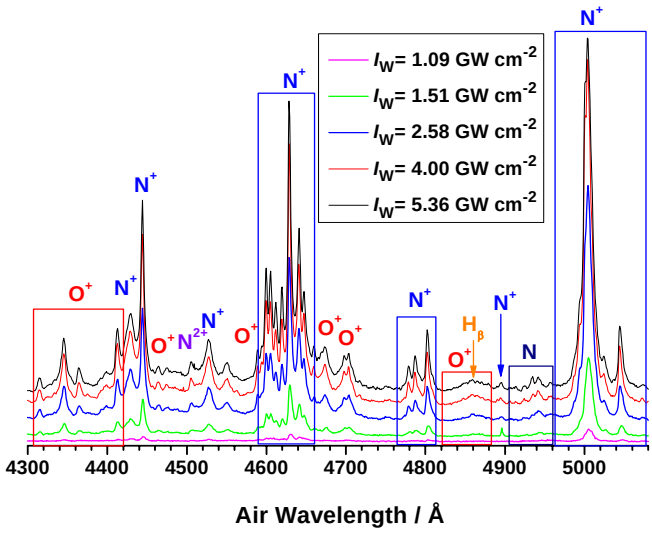

Fig. 19 Low-resolution LIB emission spectra in air at atmospheric pressure observed in the 4300-5080 Å region, excited by the TEA-CO_2 laser wavelength at 9.621 μm, as a function of the laser power density.

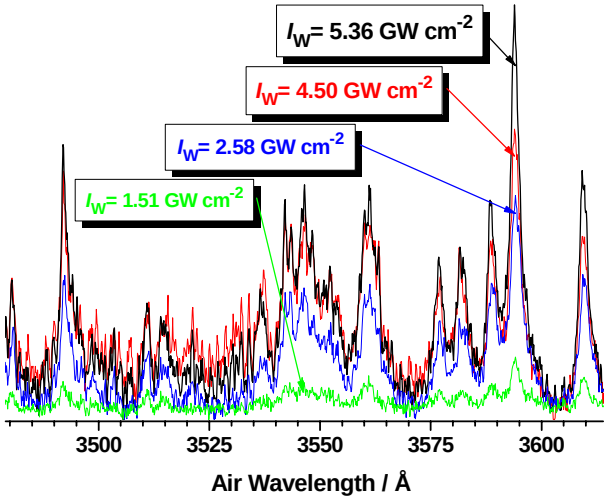

Fig. 20 High-resolution LIB emission spectra in air at atmospheric pressure, excited by the TEA-CO_2 laser wavelength at 9.621 μm, as a function of the laser intensity.

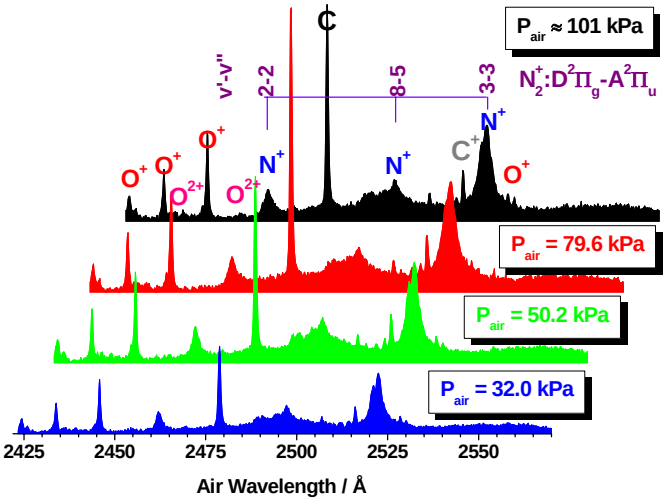

Fig. 21 High-resolution LIB emission spectra at various air pressures, excited by the TEA-CO_2 laser (10.591 μm) at a power density of 6.31 GW×cm^{-2}.

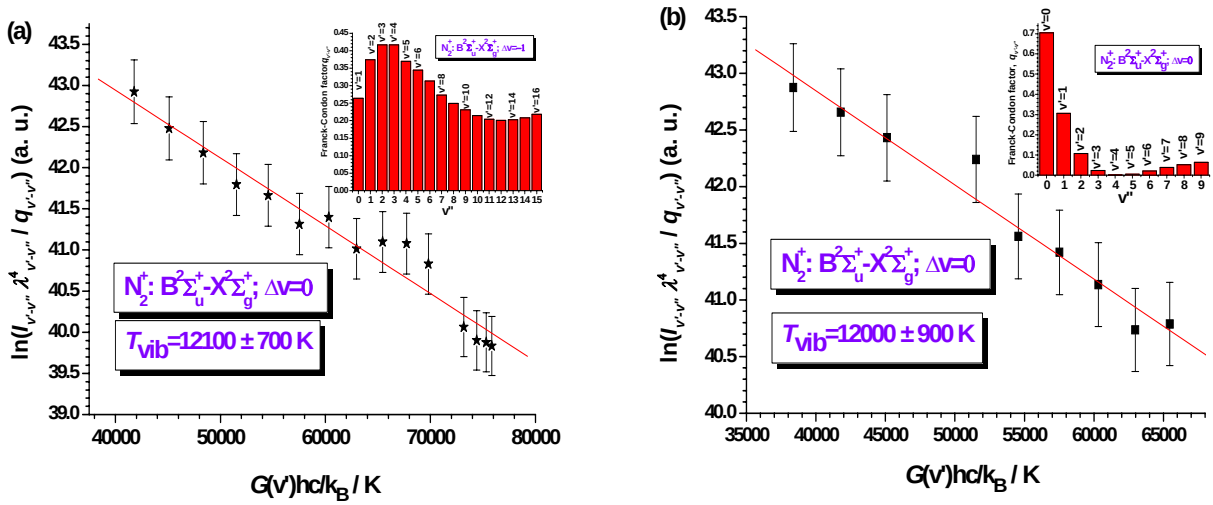

Fig. 22 Left **(a)** panel: Linear Boltzmann plot of the N_2^+ (B-X) Δv=-1 band sequence intensity versus the normalized energy of the upper vibrational level; Right **(b)** panel: Linear Boltzmann plot of the N_2^+ (B-X) Δv=0 band sequence intensity versus the normalized energy of the upper vibrational level; Experimental conditions: laser power density of 5.36 GW cm^{-2} and atmospheric pressure. Plots also show linear fit to the data and the corresponding Franck-Condon factors.

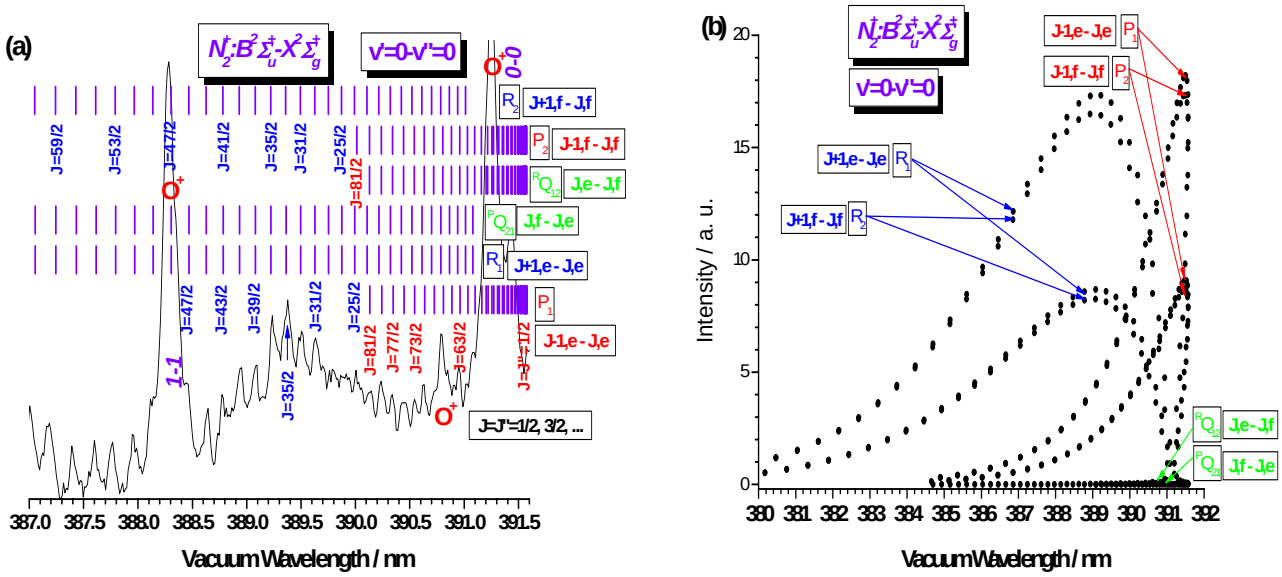

Fig. 23 (a) Detailed LIB spectrum of air and partial rotational assignments of the 0-0 $B^2\Sigma_u^+$-$X^2\Sigma_g^+$ band of N_2^+. **(b)** Calculated fortrat diagram for P_1, P_2, R_1, R_2, $^RQ_{12}$ and $^PQ_{21}$ branches in the 0-0 band (B-X) of N_2^+ at T_{rot}=1950 K.

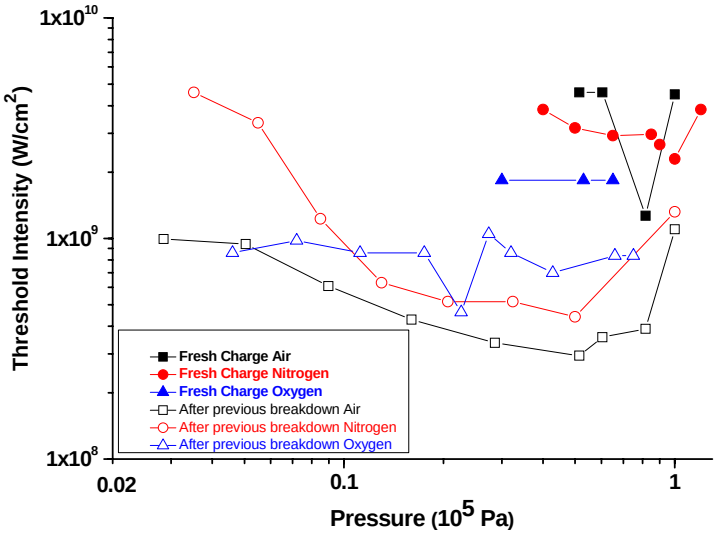

Fig. 24 Experimental laser-induced breakdown thresholds excited by the TEA-CO_2 laser (10.591 μm) in air (square), nitrogen [18] (circle) and oxygen [20] (triangle) for different pressures. Solid: fresh charge (without previous breakdown); Open: after previous breakdown.

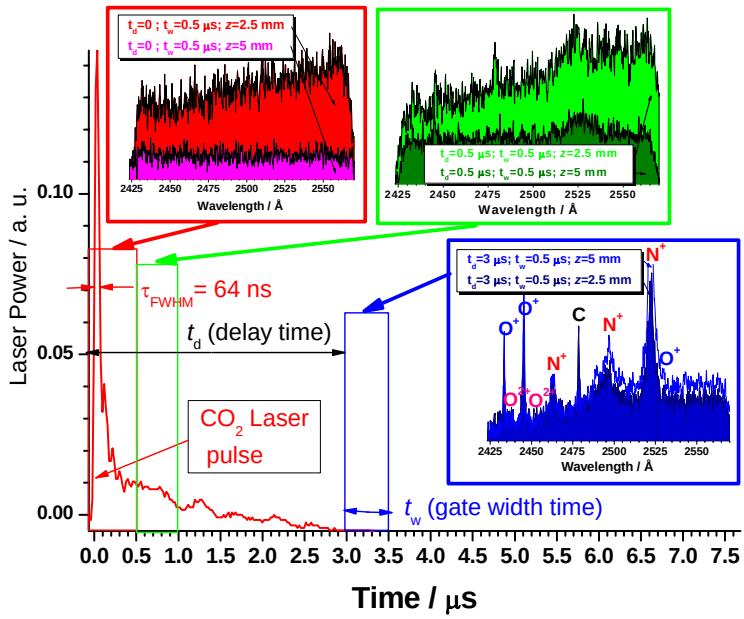

Figure 25. A schematic overview of the temporal history of LIB air plasma. Here t_d is the delay time and t_w is the gate width time during which the plasma emission is monitored. Insets plots illustrate some spectra observed at different delay times (0, 0.5 and 3 μs) for a fixed gate width time of 0.5 μs and z=2.5 and 5 mm. The temporal shape of the CO_2 laser pulse is also shown.

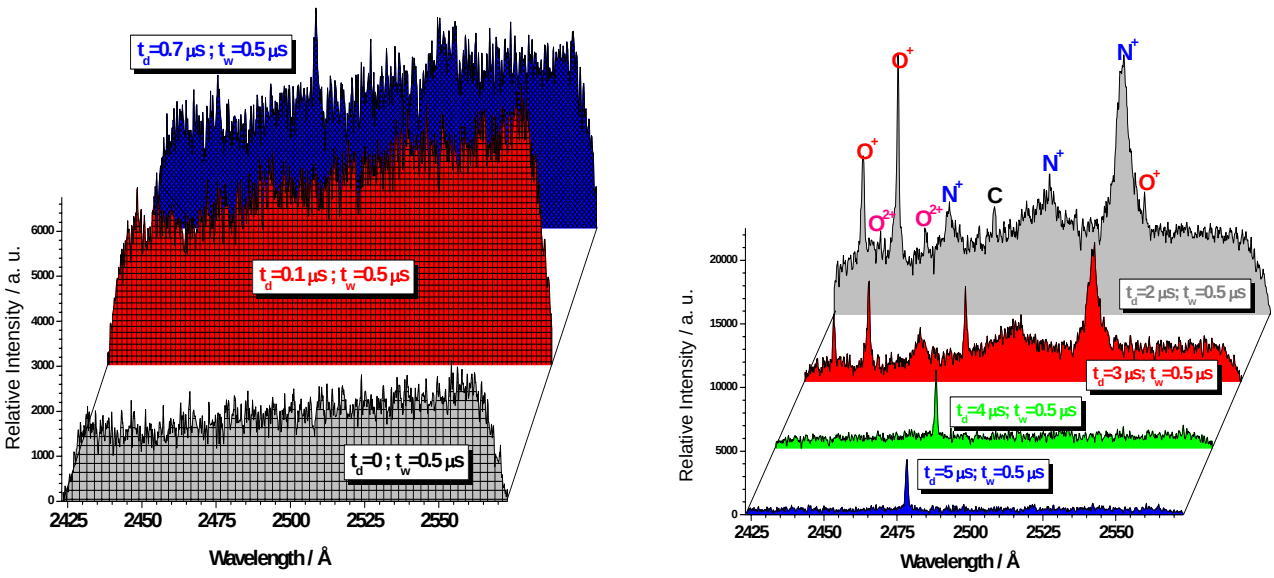

Figure 26. Time-resolved emission spectra from laser-induced (106 J/cm^2) air plasma observed in the region 2423-2573 Å monitored at 0, 0.1, 0.7, 2, 3, 4, and 5 μs gate delays for a fixed gate width time of 0.5 μs and z=2.5 mm.

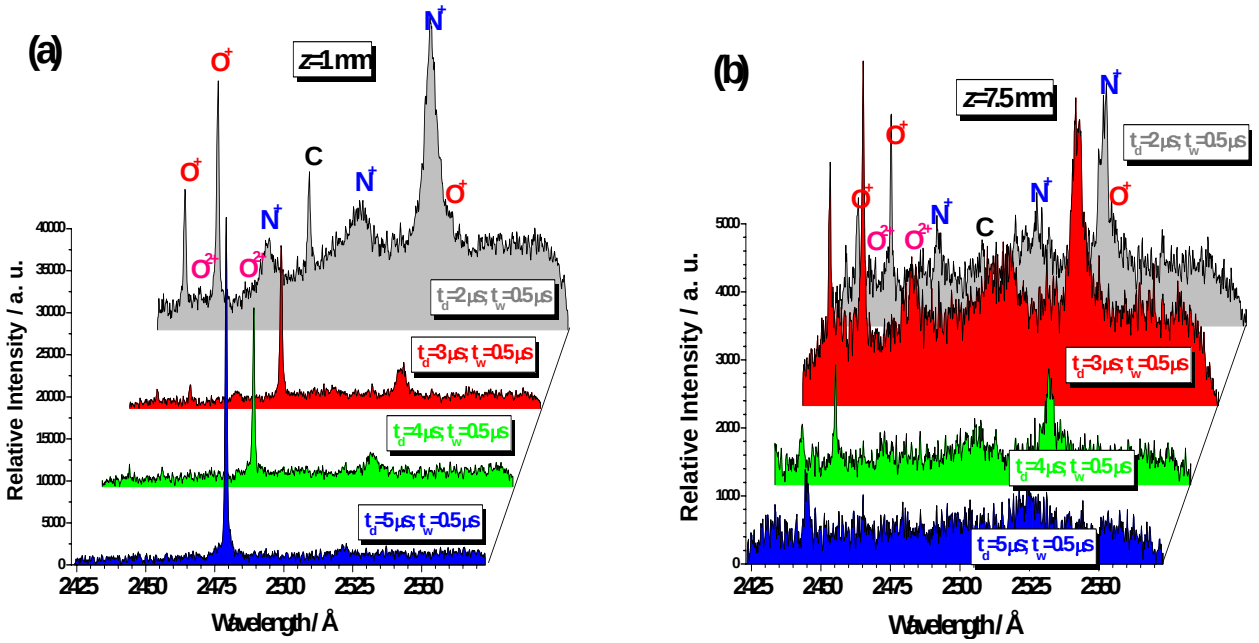

Figure 27. Time-resolved emission spectra from laser-induced (106 J/cm^2) air plasma observed in the region 2423-2573 Å monitored at 2, 3, 4, and 5 μs gate delays for a fixed gate width time of 0.5 μs and **(a)** *z*=1 mm; **(b)** *z*=7.5 mm

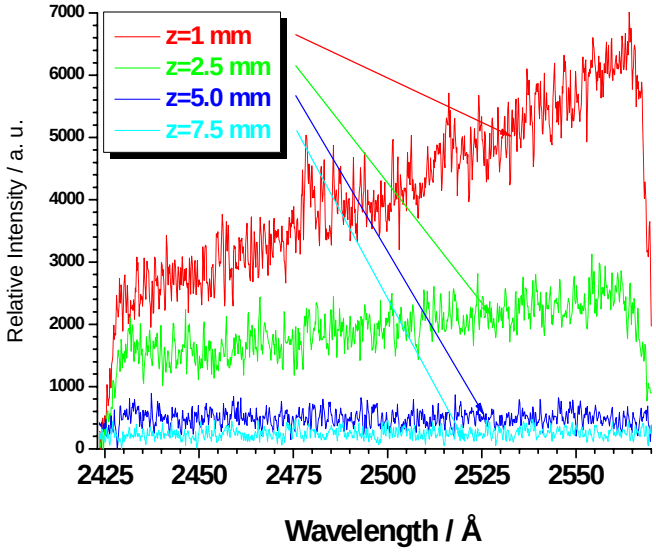

Figure 28. Time-resolved emission spectra from LIB (106 J/cm^2) in air at 1, 2.5, 5, and 7.5 mm along the plasma expansion direction (*Z*-axis) and recorded at t_d=0 and t_w=0.5 μs.

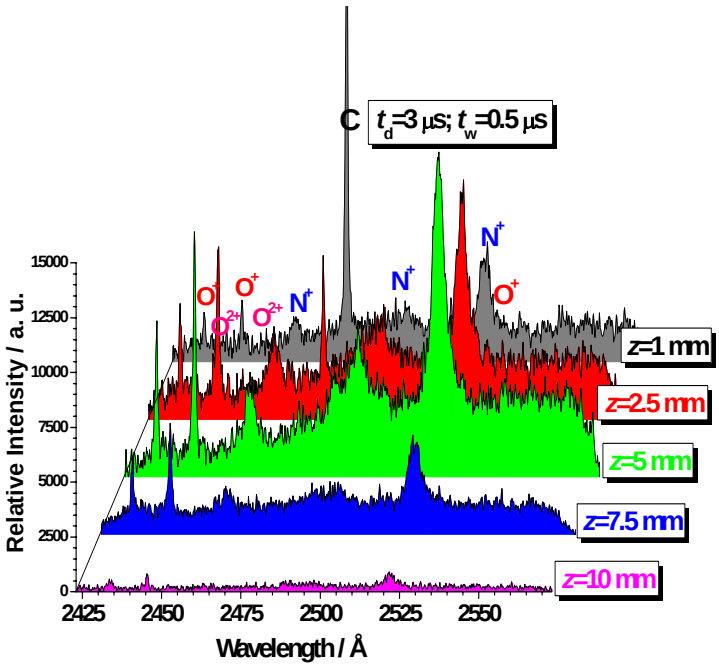

Figure 29. Time-resolved emission spectra from laser-induced air plasma (106 J/cm^2) observed in the region 2423-2573 Å at t_d=3 μs for t_w=0.5 μs monitored at 1, 2.5, 5, 7.5 and 10 mm along the plasma expansion direction.

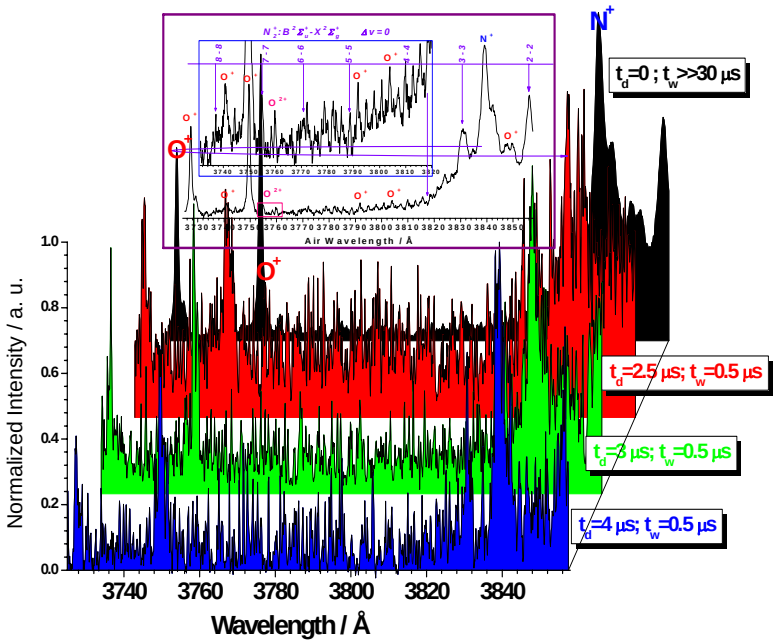

Figure 30. Time-resolved emission spectra from laser-induced (160 J/cm^2) air plasma observed in the region 3725-3860 Å region monitored at 2.5, 3 and 4 μs gate delays for a fixed gate width time of 0.5 μs (z=1 cm) and time-integrated spectrum (t_d=0 and t_w>>30 μs). The inset plot shows the assignment of some ionic lines of N^+, O^+ and O^{2+} and band heads of the molecular bands of $N_2^+(B^2\Sigma_u^+\text{-}X^2\Sigma_g^+)$.

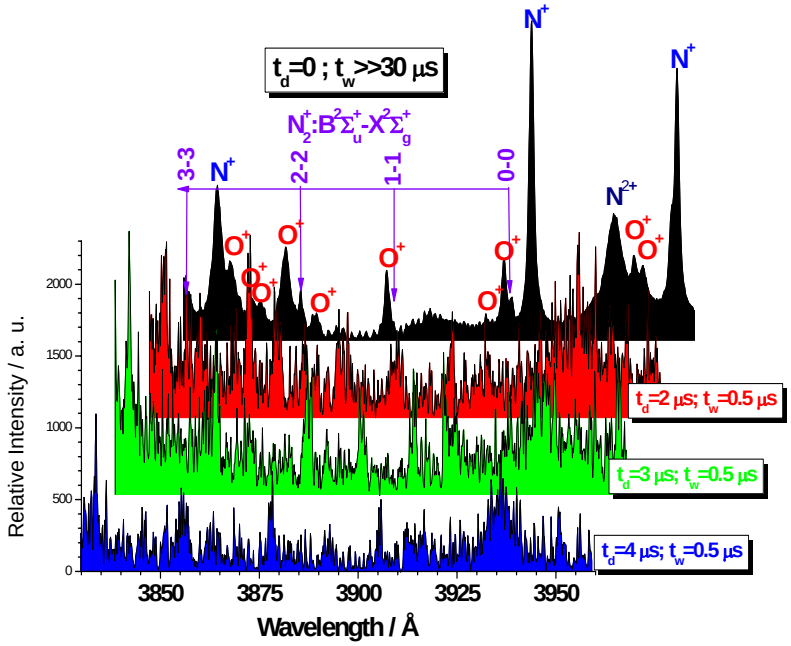

Figure 31. Time-resolved emission spectra from laser-induced air plasma (71 J/cm^2) observed in the region 3830-3960 Å monitored at 2, 3 and 4 µs gate delays for a fixed gate width time of 0.5 µs (z=1 cm) and time-integrated spectrum (t_d=0 and t_w>>30 µs). The assignments of some ionic lines of N^+, O^+ and N^{2+} and band heads of the molecular bands of $N_2^+(B^2\Sigma_u^+-X^2\Sigma_g^+)$ are indicated.

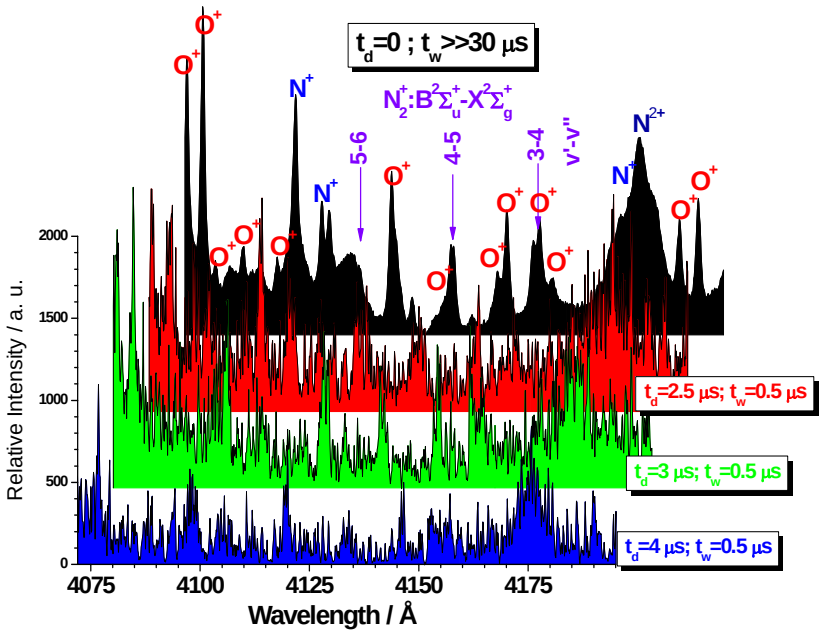

Figure 32. Time-resolved emission spectra from laser-induced air plasma (71 J/cm^2) observed in the region 4070-4195 Å monitored at 2.5, 3 and 4 µs gate delays for a fixed gate width time of 0.5 µs (z=1 cm) and time-integrated spectrum (t_d=0 and t_w>>30 µs). The assignments of some ionic lines of N^+, O^+ and N^{2+} and band heads of the molecular bands of $N_2^+(B^2\Sigma_u^+-X^2\Sigma_g^+)$ are indicated.

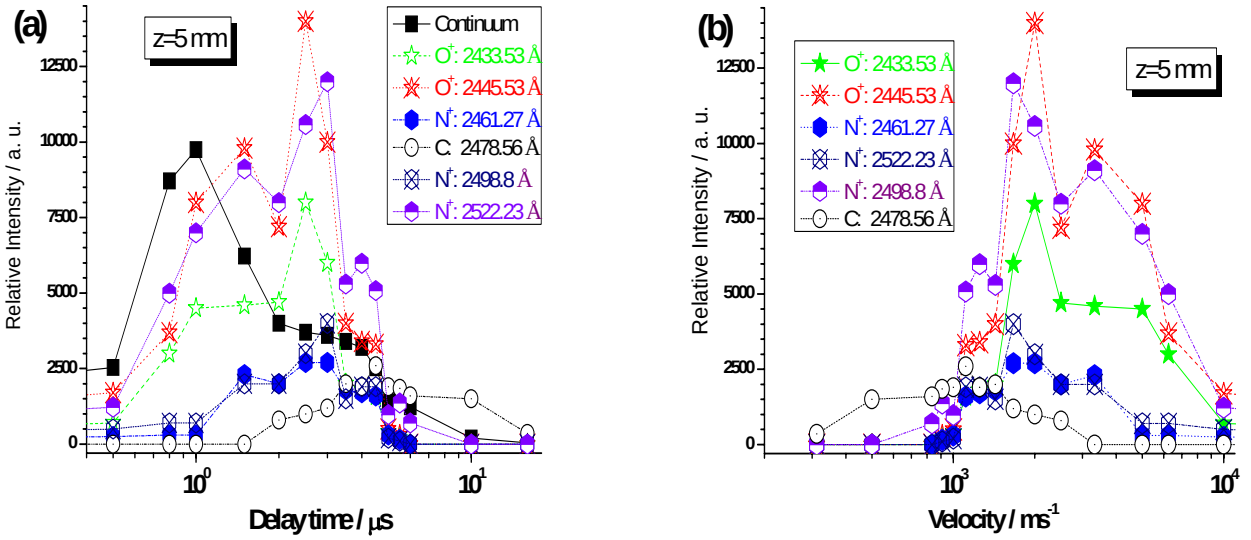

Figure 33. (a) Number density TOF distributions of continuum radiation, O^+(2433.53; 2445.54 Å), N^+(2461.27; 2478.56; 2522.23 Å) and C(2478.56 Å) lines as a function of delay time (fixed gate width time of 0.5 μs) for a laser fluence of 106 J/cm^2 and *z*=5 mm. (b) Velocity distributions derived from the experimental TOF profiles for the indicated species.

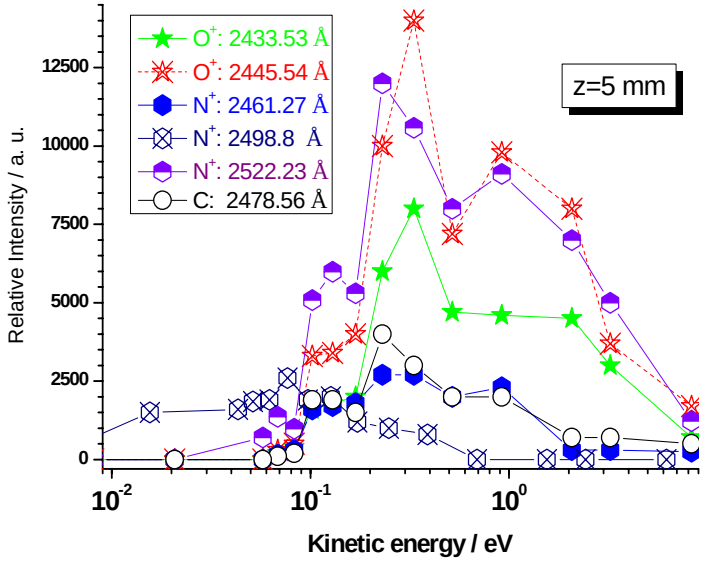

Figure 34. Kinetic energy distributions of O^+(2433.53 Å), O^+(2445.54 Å), N^+(2461.27 Å), N^+(2478.56 Å), N^+(2522.23 Å) and C(2478.56 Å) lines derived from the TOF spectra at z=5 mm.

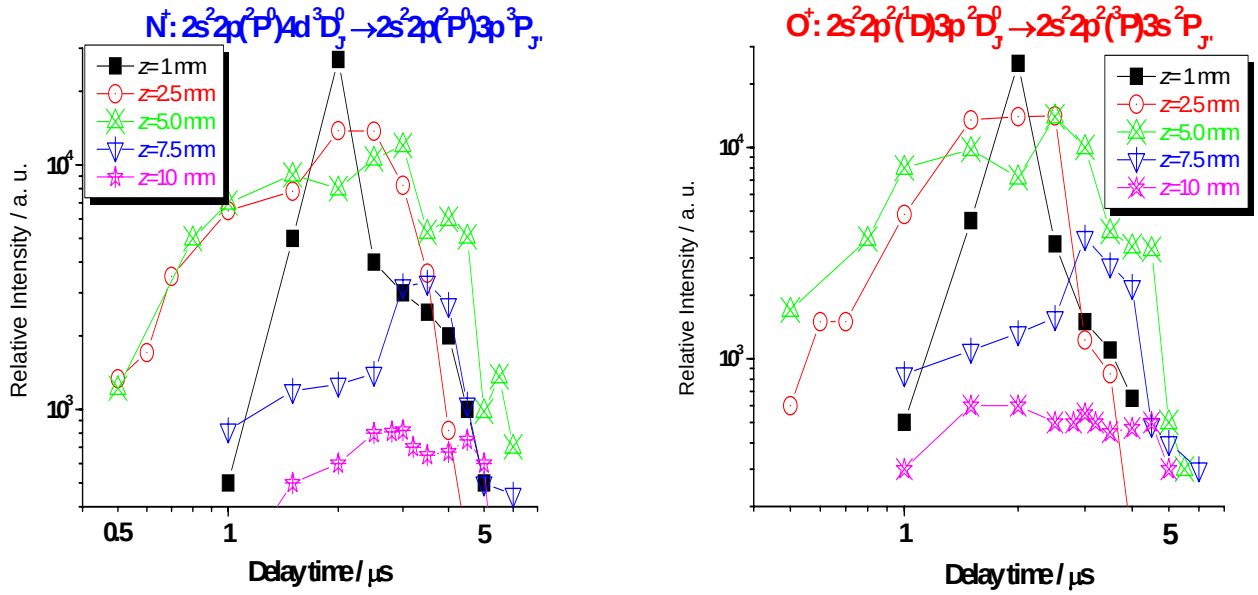

Figure 35. Number density TOF profiles of multiplet structures of N^+(~2522 Å) and O^+(~2445 Å) at 1, 2.5, 5, 7.5 and 10 mm as a function of delay time for a laser fluence of 106 J/cm^2.

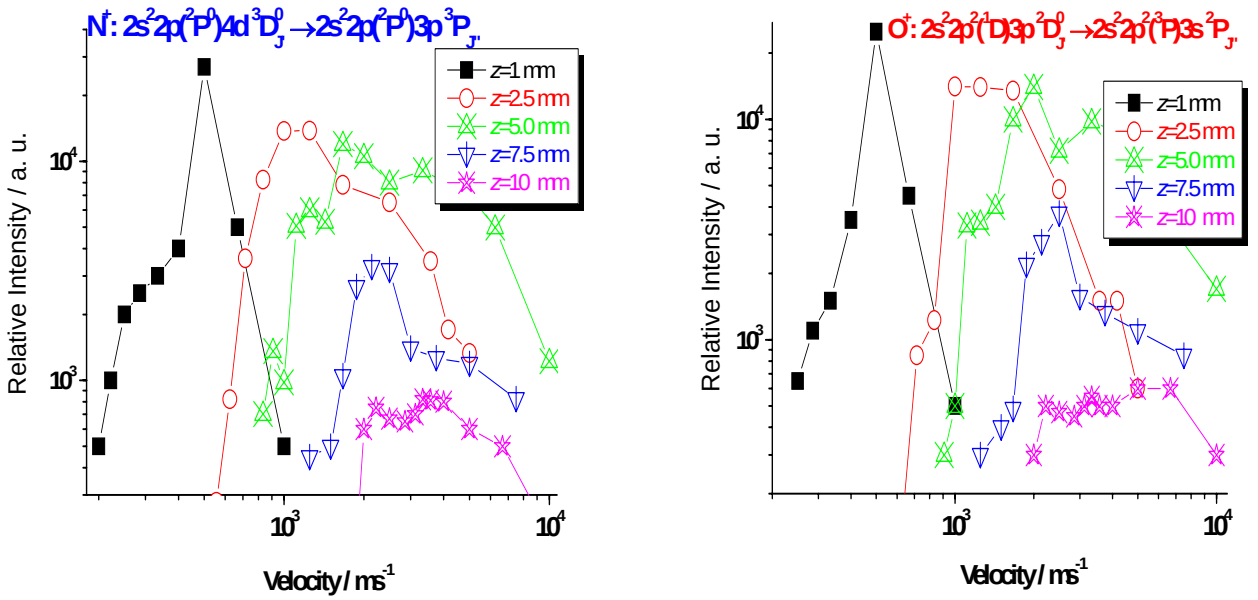

Figure 36. Velocity profiles of multiplet structures of N^+(~2522 Å) and O^+(~2445 Å) at 1, 2.5, 5, 7.5 and 10 mm as a function of delay time for a laser fluence of 106 J/cm^2.

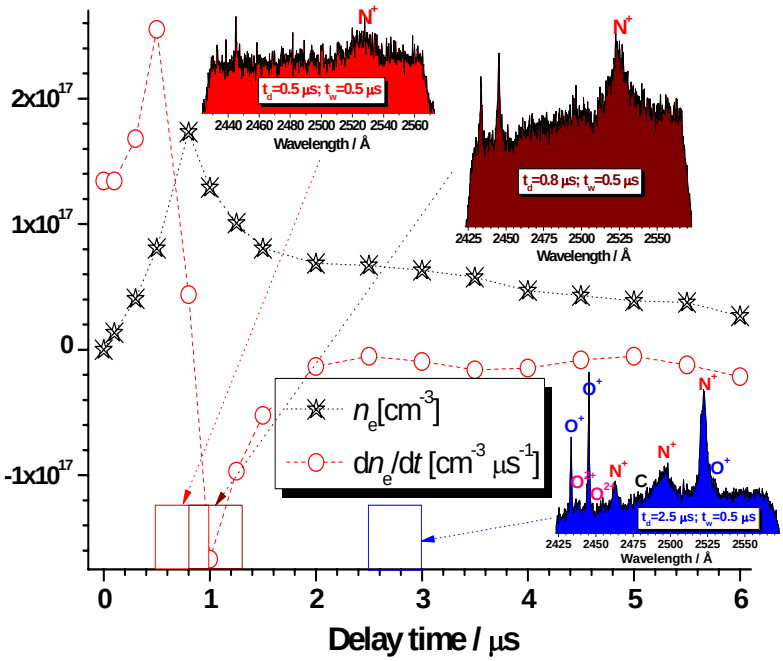

Figure 37. The temporal evolution of electron density n_e and dn_e/dt for different delay times from plasma ignition and z=5 mm. Inset plots illustrate some spectra observed at different delay times.